NTNU
Norwegian University
of Science and Technology

Department of Energy
and Process Engineering

EPT-M-2016-59
EPT-M-2016-99

MASTER THESIS

for

Students
Øyvind Huuse and Erik Rasmussen Prytz

Spring 2016

Numerical Simulation of Flow around the NREL S826 Airfoil at Moderate Reynolds Numbers Using Detached Eddy Simulation (DES)

Numerisk simulering av strømning rundt vingeprofil NREL S826 ved moderate Reynoldstall ved hjelp av løsnet vivel simulering (DES)

Background and objective

For the design of wind turbines, the fast and reliable computation of flow around airfoils at moderate Reynolds numbers is essential. Here, flow over the NREL S826 airfoil at Reynolds numbers between about 10^5 and 10^6 will be considered.

The objective is to check detached eddy simulation (DES) for flow around the NREL S826 airfoil at moderate Reynolds numbers, to check the model parameters which best match experimental data, and to analyze the computational cost.

The project will give the candidate a good introduction into modern turbulence modeling of transitional and turbulent flow in aerodynamics as well as first-hand experience of computational fluid dynamics (CFD) tools involving grid generation, numerical methods, validation, flow visualization, and flow analysis.

The following tasks are to be considered:

1. Study the literature to get an overview over hybrid RANS-LES models, in particular DES.
2. Generate suitable grids for DES of flow around the NREL S826 airfoil at Reynolds numbers between about 10^5 and 10^6.
3. Perform DES of that flow with a CFD tool and compare results with experimental data.
4. Check the sensitivity of the results with respect to grid, boundary conditions and DES model parameters. Which model parameters match the experimental data best?
5. Analyze the computational cost with respect to key model parameters.

-- " --

Within 14 days of receiving the written text on the master thesis, the candidate shall submit a research plan for his project to the department.

When the thesis is evaluated, emphasis is put on processing of the results, and that they are presented in tabular and/or graphic form in a clear manner, and that they are analyzed carefully.

The thesis should be formulated as a research report with summary both in English and Norwegian, conclusion, literature references, table of contents etc. During the preparation of the text, the candidate should make an effort to produce a well-structured and easily readable report. In order to ease the evaluation of the thesis, it is important that the cross-references are correct. In the making of the report, strong emphasis should be placed on both a thorough discussion of the results and an orderly presentation.

The candidate is requested to initiate and keep close contact with his/her academic supervisor(s) throughout the working period. The candidate must follow the rules and regulations of NTNU as well as passive directions given by the Department of Energy and Process Engineering.

Risk assessment of the candidate's work shall be carried out according to the department's procedures. The risk assessment must be documented and included as part of the final report. Events related to the candidate's work adversely affecting the health, safety or security, must be documented and included as part of the final report. If the documentation on risk assessment represents a large number of pages, the full version is to be submitted electronically to the supervisor and an excerpt is included in the report.

Pursuant to "Regulations concerning the supplementary provisions to the technology study program/Master of Science" at NTNU §20, the Department reserves the permission to utilize all the results and data for teaching and research purposes as well as in future publications.

The final report is to be submitted digitally in DAIM. An executive summary of the thesis including title, student's name, supervisor's name, year, department name, and NTNU's logo and name, shall be submitted to the department as a separate pdf file. Based on an agreement with the supervisor, the final report and other material and documents may be given to the supervisor in digital format.

☐ Work to be done in lab (Water power lab, Fluids engineering lab, Thermal engineering lab)
☐ Field work

Department of Energy and Process Engineering, 13. January 2016

Olav Bolland
Department Head

Bernhard Müller
Academic Supervisor

Abstract

In this study computational fluid dynamics (CFD) was used to simulate the flow around the asymmetric NREL S826 airfoil. ANSYS Fluent v.16.2 was used as the CFD solver, while ANSYS Meshing was used for creating the grids.

The 3D domain was built as a replica of the low speed wind tunnel at the Norwegian University of Science and Technology (NTNU), with the walls of the windtunnel approximated as slip walls. This is done so that grid refinements not are needed towards the walls. The flow was simulated at medium to low Reynolds numbers in the range $5 \cdot 10^4 - 10^6$. The goal was to see if any improvement could be made by using detached eddy simulation (DES), a hybrid Reynolds-averaged Navier Stokes (RANS) - large eddy simulation (LES) turbulence model, compared to the 2D RANS simulations. Thereby, the quality of DES simulation results was to be assessed to check whether DES constitutes a viable alternative to the computationally more costly LES.

Reviewing the DES literature, it was found that the Delayed DES (DDES) is now the new standard hybrid scheme and was therefore used in almost all simulations.

A time step study was performed to determine a criterion for the time step size leading to efficient and accurate simulations. Then a grid dependence study was run, while refining the grid in one direction at a time to better be able to determine what refinements actually affect the solution. The grid is very important, as in DDES the grid size is also involved in deciding where to use the different models. It was shown that the solution was not grid independent and that refinements in the spanwise direction gave more 3D effects. To be able to run the whole analysis a grid leading to good accuracy and not too high computational costs was chosen.

After testing numerous numerical settings, a choice was made to continue with the realizable $k-\epsilon$ model as RANS model in DDES. This choice was made based on both computational time and accuracy of the simulation results compared with measurements in the NTNU low wind speed windtunnel. A Reynolds number study was con-

ducted where the DDES was compared with experimental values and the LES study from the Technical University of Denmark (DTU).

DDES was found to perform better than 2D RANS results and even as well as an LES study at a fraction of the computational costs. While being able to remove many cells due to the lower resolution criteria in DDES compared to LES, one can use that saved computational power to build a much more accurate geometry that might even produce more accurate results than the LES. Stall cells over the suction side of the airfoil were also observed in the stall region. The observed Reynolds dependency around the stall angles should be examined more thoroughly in future studies.

Preface

This thesis is the conclusion of five years studying at the Norwegian University of Science and Technology (NTNU) for both of the authors. It was a collaborative effort and a continuation of the previous 2D study conducted by one of the authors. Since it is a continuation, much of the basic theory regardeing the physics and numerics is taken from that study. This extraction of information is indicated in the present master's thesis and done with the author's full knowledge and accept. We are truly grateful for the opportunities this school has given us and also a one year stay at the University of Cape Town (UCT) and Prof. Arnaud Malan, UCT, who introduced us to CFD.

We also want to thank our very helpful supervisor Prof. Bernhard Muller who has been a lighthouse in the confusing darkness a master's thesis sometimes can be. Last, but not least, we want to thank our girlfriends, Julie and Nora, for their unconditional support.

Contents

List of Tables

List of Figures

Abbreviations

2D	=	2-Dimensional
3D	=	3-Dimensional
AIAA	=	The American Institute of Aeronautics and Astronautics
ANSYS	=	Analysis System
BC	=	Boundary Conditions
BCD	=	Bounded Central Differencing
CFD	=	Computational Fluid Dynamics
CPU	=	Central Processing Unit
CV	=	Control Volume
D	=	Depth edge
DDES	=	Delayed Detached Eddy Simulation
DES	=	Detached Eddy Simulation
DNS	=	Direct Numerical Simulation
DTC	=	Digital Temperature Compensation
DTU	=	Technical University of Denmark
E	=	East edge
FSM	=	Fractional Step Method
HAWT	=	Horizontal-Axis Wind Turbines
IDDES	=	Improved Delayed Detached Eddy Simulation
LES	=	Large Eddy Simulation
MUSCL	=	Monotonic Upstream-Centered Scheme for Conservation Laws
N	=	North Edge

NITA	=	Non Iterative Time-Advancement
NREL	=	National Renewable Energy Laboratory
NTNU	=	Norwegian University of Science and Technology
NTU	=	Non-dimensional Time Unit
NW	=	Nort-West edge
PISO	=	Pressure-Implicit with Splitting of Operators
PRESTO!	=	PREssure STaggering Options
RANS	=	Reynolds-Averaged Navier–Stokes
SA	=	Spalart-Allmaras
SGS	=	Sub-Grid Scale
SIMPLE	=	Semi Implicit Method for Pressure Linked Equations
SIMPLEC	=	Semi Implicit Method for Pressure Linked Equations Correction
SST	=	Shear Stress Transport
SC	=	Stall Cells
TI	=	Turbulent Intensity
TSS	=	Time step size
W	=	West edge
WALE	=	Wall-adapting Local Eddy-viscosity

Symbols

C_{DES}	=	DES Constant
C_p	=	Pressure coefficient
$P_{extracted}$	=	Power extracted
$P_{available}$	=	Power available
ω_r	=	Rotations per second
ρ	=	Density
U_∞	=	Free Flow velocity
A	=	Area
Re	=	Reynolds number
c	=	Chord length
ν	=	Kinematic viscosity
τ_w	=	Wall shear stress
μ	=	Dynamic viscosity
U	=	Velocity
Re_{crit}	=	Critical Reynolds number at the laminar instability point
ρ_∞	=	Free flow density
C_f	=	Skin friction coefficient
y^+	=	Non-dimensional distance to the wall
y	=	Distance to the wall
μ_τ	=	Turbulent viscosity
C_d	=	Drag coefficient
D	=	Drag force

C_l	=	Lift coefficient
L	=	Lift force
P	=	Pressure
P_∞	=	Free flow pressure
C_m	=	Moment coefficient
M	=	Moment force
V	=	Volume
τ	=	Shear stress
ϕ	=	Variable
$\overline{\phi}$	=	Mean part of variable
ϕ'	=	Fluctuating part of variable
u'	=	Fluctuating part of velocity
k	=	Turbulent kinetic energy
ϵ	=	Turbulent dissipation rate
ω	=	Dissipation rate per turbulent kinetic energy
ν_t	=	Kinematic eddy viscosity
$G_{\overline{\nu}}$	=	Turbulent viscosity production
Y_ν	=	Destruction of turbulent viscosity
$S_{\overline{\nu}}$	=	Spalart Allmaras source term
$\sigma_{\overline{\nu}}$	=	Spalart Allmaras constant
C_{b2}	=	Spalart Allmaras Constant
G_b	=	Turbulent kinetic energy generation
Y_m	=	Contribution of the fluctuating dilatation in compressible turbulence
σ_k	=	Turbulent Prandtl number for k
σ_ϵ	=	Turbulent Prandtl number for ϵ
$C_{1\epsilon}, C_{2\epsilon}, C_{3\epsilon}$	=	$k-\epsilon$ constants
G_k	=	Turbulent kinetic energy generation from mean velocity gradients
G_ω	=	Generation of ω
Γ_k	=	Effective diffusivity of k

Γ_ω	=	Effective diffusivity of ω
Y_k	=	Dissipation of k
Y_ω	=	Dissipation of ω
S_k, S_ω	=	$k-\omega$ source terms
F_1	=	SST $k-\omega$ blending function
S_{ij}	=	Rate-of-strain for the resolved scale
C_ω	=	WALE constant
κ	=	Von Karman constant
d	=	Distance to the wall
V	=	Volume
Δ_{max}	=	Maximum grid spacing of the grid cell considered
$\mathbf{u}$	=	Velocity vector
Γ	=	Diffusion coefficient
S_ϕ	=	Finite volume method source term
f	=	Quadrilateral control volume
V_p	=	Quadrilateral control volume area
F	=	Force
I	=	Turbulent intensity
u_{avg}	=	Average velocity
Γ_ϕ	=	Diffusion coefficient for ϕ
n	=	Time step
β_n	=	Bounding factor for the given time step
C	=	Courant number
s	=	Seconds
m	=	Meter
kg	=	Kilograms
Δt	=	Difference in t
α	=	Angle of attack
$\sigma_{\omega,2}$	=	SST $k-\omega$ constant

Chapter 1

Introduction

1.1 Background and motivation

The need for clean carbon free energy production is as high as ever, both to satisfy the rising global energy need while at the same time trying to contain the climate change we are already starting to experience. There is now broad agreement that there is an *"an urgent need for a veritable energy revolution, involving a wholesale global shift to low-carbon technologies"* [31].

One of the most popular and promising options is to exploit wind energy through wind turbines. Converting the kinetic energy of the turbines into electric energy has a high efficiency, so to bring down the cost of wind energy the aerodynamic properties of the wings, designed to capture as much as possible of the wind's kinetic energy, are the principal component [21]. It is important to be able to simulate these properties correctly, as experiments can be both hard to conduct correctly and expensive.

1.1.1 Outline

This study has five connected tasks given in the project description above. The outline of this master's thesis is as follows:

- The literature on hybrid RANS-LES models will be reviewed in section 1.2.

- Chapters 2 and 3 consider numerical and theoretical aspects. In addition, details of DES as a hybrid RANS-LES model will be presented.
- Grid generation and time stepping are detailed in chapter 4. They yield accurate and efficient solutions for Reynolds numbers between $5 \cdot 10^4$ and 10^6.
- The verification and validation of the different settings in ANSYS Fluent creating different results and accuracy are discussed in chapter 5
- A Reynolds number study is presented in chapter 6 ranging from angles of attack $-12°$ to $14°$, for the above mentioned Reynolds numbers.

This study is also a continuation of the project thesis by one of the authors [16]. It was an 2D study of the same airfoil and will be of some inspiration when considering the grid and verification.

1.2 Literature Review

In 1997 Spalart et al. [30] published comments on the feasibility of LES and hybrid RANS/LES simulation of flow over wings. Although the accuracy of a LES simulation has the potential to become a Direct Numerical Simulation (DNS) solution for a fine enough grid resolution, this is not, or at least was not, practically possible at the time of the study. LES especially struggles with keeping the computational costs down when wall bounded flow is simulated. For example, to properly calculate the flow over an airplane wing the grid resolution needs to be in the order of 10^{11} grid points and $5 * 10^6$ time steps [30]. This is due to the small dimensions of the energy carrying eddies in the boundary area. Additionally, for higher Reynolds numbers the grid resolution would have to increase. At the same time, if turbulent flow away from walls is simulated, the grid resolution can be greatly reduced and still gives satisfactory accuracy compared to wall bounded flow, because the eddies are considerably larger here. A promising method to avoid this expensive increase in grid resolution when using LES is to use hybrid RANS/LES models. The general idea for a hybrid RANS/LES model is that a switch activates a RANS model when calculating boundary layer flow and switch to LES when

turbulent flow away from walls is calculated. That way, the small eddies will be modelled by RANS and the large eddies will be modelled by LES. This reduces the resolution requirement for the grid and increases the time step size, ultimately reducing the computational cost of the simulation.

In 1999 Shur et al. [22] conducted the first three-dimensional (3D) DES experiment based on the findings from [30], using the Spalart Almaras (SA) turbulence model. The simulation was conducted on an airfoil at high angle of attack in order to study how well the method would tackle flow with large separation. The results showed that the error of the simulation was less then 10% compared to the experimental results for both moderate and high Reynolds numbers. Only $\sim 2 * 10^5$ grid points where required for the DES, a great reduction compared to LES.

Although DES has shown promising results compared to both RANS and LES, it still has some weaknesses. The switch between RANS and LES in DES is controlled by whether the distance to the closest wall or the largest grid spacing is the smallest at the given point. RANS is activated when the wall distance is smaller than the largest grid spacing multiplied by a "DES" constant (C_{DES}). Otherwise, LES is activated. This means that if the grid spacings all get small close to the wall, LES will be activated instead of RANS. If the grid still is stretched in one direction, as can be seen in Figure 1.1, this leads to a problem called modelled-stress depletion (MSD) [27] since LES will be activated. But the grid is not small enough to offer accurate LES solutions the modelled stress gets too small which can lead to grid-induced separation [29].

This means that separation can appear earlier than experimental solutions show and that separation can occur even when there is no proof of it in experimental solutions. In 2006 Spalart et al. [29] came up with a way to keep RANS activated throughout the boundary layer by introducing a new factor to the DES switch between RANS and LES. This modification is dependent on the eddy viscosity of the flow and therefore includes the solution when choosing between using RANS or LES to obtain a solution [29]. This method is called Delayed DES (DDES) and is often considered the new standard for DES [27].

DES and DDES can both suffer from log-layer mismatch. The phenomenon is caused

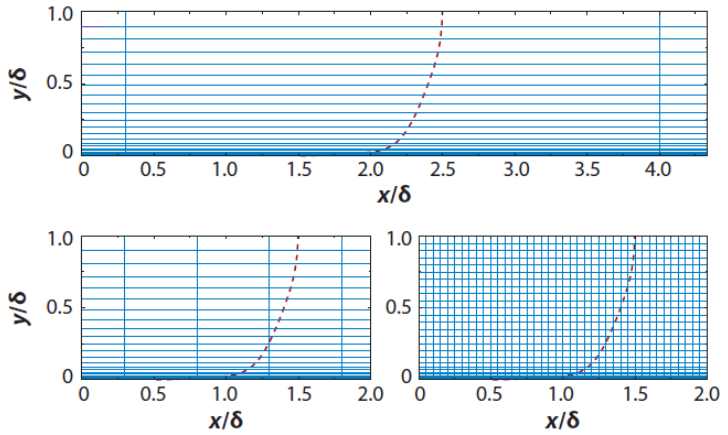

Figure 1.1: Showing different stretching of the grid in the x-direction. The LES model will start similarly close to the wall in all cases, but the cell size might be too large for solving LES with sufficient accuracy in the most stretched cases [27].

by velocity fields from the RANS range, close to walls, effecting the velocity field of the adjacent LES range [9]. This leads to over prediction of the mean velocity gradient, subsequently creating an unnatural buffer layer [9]. An attempt to resolve this log-layer mismatch problem is called improved DDES (IDDES) [23]. The log-layer mismatch problem is resolved by combining DDES with an improved RANS-LES hybrid model designed for wall modelling in LES (WMLES). IDDES will use WMLES when the inflow has sufficient turbulent content and everything will be resolved except close to the wall, where the flow will be modelled. If the inflow has less turbulent content than for WMLES, IDDES will use DDES. The use of WMLES will increase the amount of resolved turbulent activity and thereby remove the log-layer mismatch problem. There have also been proposals of zonal DES where different regions are strictly marked as either RANS or LES territory [5]. This obviously requires deep knowledge of the physics beforehand to be able to label the different zones correctly.

It is clear that there is a place for a model that resolves boundary layers with RANS and LES in the outer regions, and therefore DDES has become the new standard for hybrid RANS-LES modelling. Therefore, DDES will be in focus throughout this study.

1.3 The NREL S826 Airfoil

This section is mostly taken from the project thesis [16].

The majority of the airfoils in use today were originally developed for air crafts. But the design requirements for these airfoils (primarily NACA airfoils), are significantly different from wind turbine airfoils. In 1984, the development of special-purpose airfoils for horizontal-axis wind turbines (HAWTs) began, as a joint effort between National Renewable Energy Laboratory (NREL) and Airfoils Incorporated. NREL has since then developed several airfoil families with a general performance requirement that the airfoils exhibit a maximum lift coefficient, which is relatively insensitive to roughness effects [11].

In this report, an airfoil from the S-Series airfoils will be considered. The S826 airfoil is a tip airfoil designed for horizontal-axis wind turbines with 20-40 meter wings, and operation at variable-speed and pitch. The S826 airfoil profile meets the NREL requirements and produces high maximum lift, an insignificant sensitivity to roughness as well as low profile drag at multiple wind conditions [25]. The lift is increased by the high pressure field created by the curvature at the lower back side of the airfoil. An illustration of the airfoil geometry is depicted in Figure 1.2

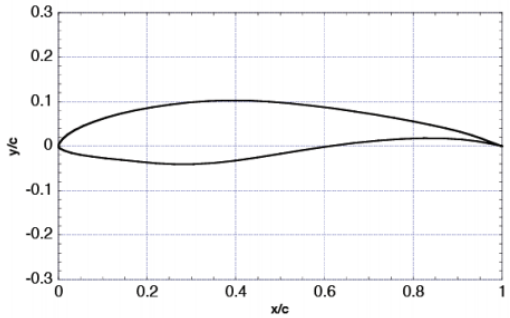

Figure 1.2: The S826 airfoil geometry

The NREL826 airfoil has been investigated in wind tunnels both at the Norwegian University of Science and Technology (NTNU) [1] and at the Technical University of Denmark (DTU) [18]. The main focus of the studies has been to determine the pressure

distribution over the airfoil profile, and its lift properties. However, the two experiments have been carried out with slightly different conditions, which need to be considered when using the experiments as a source of validation. There are different turbulent intensities and the conditions used when comparing the three different turbulent models are slightly different as well.

After this first chapter, the theory behind this study will be presented. Then a chapter on the numerical methods will follow, before presenting the grid generation. An important chapter on verification and validation will be followed by the full Reynolds number study. Towards the end a discussions will come before a brief conclusions. In the appendix, all the plots and visualization of the flow are presented.

Chapter 2

Theory

Some of the sections in this chapter are partly taken from [16].

2.1 Physics

Modelling fluid passing over and airfoil is a complex task and this section will give an introduction on wind turbines in general, before tackling the most important physical aspects to keep in mind when simulating such a flow.

2.1.1 Wind Turbine

The goal of a wind turbine is to harness the kinetic energy stored in wind. There are numerous ways to achieve this, but the most common ones, also the type of turbine the airfoil in this study is designed for, are the Horizontal Axis Wind Turbines (HAWTs). In this design, the blades are mounted perpendicular to a horizontal axis. When they are exposed to wind, they will rotate and create torque, which in turn is converted into electricity by a generator.

The theoretical amount of available energy is dependent on the cross section of the blades, and the density and the speed of the air. Since the air needs some velocity left to be transported away from the blades, this theoretical amount of energy is unobtainable.

It has been calculated through momentum theory that the maximum efficiency of a wind turbine is 59.3%, which is called the Betz limit. The efficiency of a wind turbine is defined by:

$$C_p = \frac{P_{extracted}}{P_{available}} = \frac{\omega_r M}{\frac{1}{2}\rho U_\infty^3 A} \tag{2.1}$$

where $P_{extracted}$ and $P_{available}$ is power extracted from the wind and available kinetic energy in the wind respectively, ω_r is rotations per second, M is the moment, ρ is the density, U_∞ is the free flow velocity and A is the area. The aerodynamical design is crucial in converting as much as possible of the kinetic energy into a force lifting the wing and creating torque in the turbine. However there will also be created a force dragging the wing backwards, which the whole wind structure needs to withstand.

2.1.2 Reynolds number

The Reynolds number is defined as a ratio between inertial and viscous forces. For an airfoil it is defined as the ratio between the free flow velocity, U_∞ and the cord length, c, to the kinematic viscosity, ν, of the fluid:

$$Re = \frac{U_\infty c}{\nu} \tag{2.2}$$

Higher Reynolds numbers lead to thinner boundary layers and to increased viscous forces. The inertial forces increase proportional with the square of the velocity, this leads to that in general a higher Reynolds number means a higher lift to drag ratio.

2.1.3 Boundary layer

Given the no-slip condition, zero velocity at the surface, on a wall, the fluid passing by close to the wall will be affected by it, causing a velocity gradient normal to the surface. This again is causing a shear stress to be formed that is proportional to the normal gradient of the tangential velocity component [19]:

$$\tau_w = \mu \frac{dU}{dy}|_w \tag{2.3}$$

where μ is the viscosity of the fluid. This creates a friction force along the surface that can be calculated by integrating the shear stress over the surface. This friction force will naturally slow down the fluid particles around the wall and cause a displacement of the fluid near the wall. The boundary layer will grow as the particles slowing down near the wall will affect other particles further and further away from the wall, Figure 2.1. The thickness of the boundary layer is usually defined as the distance between the wall and where the velocity is 99% of the free stream velocity, $U(y) = 0.99U_\infty$. In this area, due to continuity, the streamlines are bent around the body.

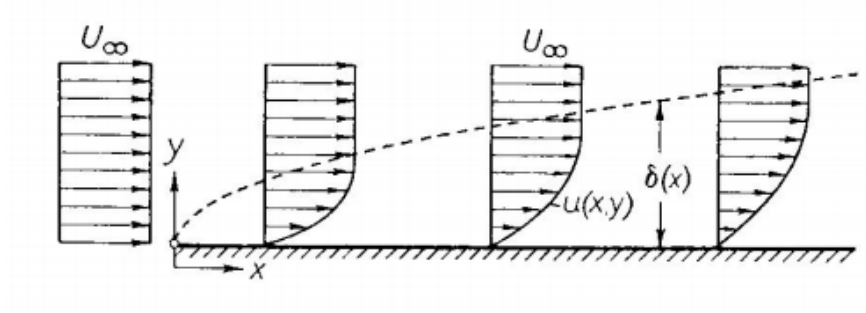

Figure 2.1: Boundary layer growing as the flow moves over a plate, from [20]

2.1.4 Transition

The area where the flow goes from laminar to turbulent is an essential phenomenon when considering a flow around an airfoil. A laminar boundary layer is characterized by having a flow divided into layers without much communication between them. If, however, the Reynolds number is large enough, it will destabilize the boundary layer and the flow will turn turbulent at some point. Turbulent flows are characterized by irregular fluctuating motion that is strongly rotational and three dimensional [32]. The transition is not a single point, but rather a transition zone. The initial disturbances become bigger and bigger and eventually changes the flow into a turbulent one, as shown

in Figure 2.2. The transition is also affected by roughness on the surface and turbulent motion in the free stream.

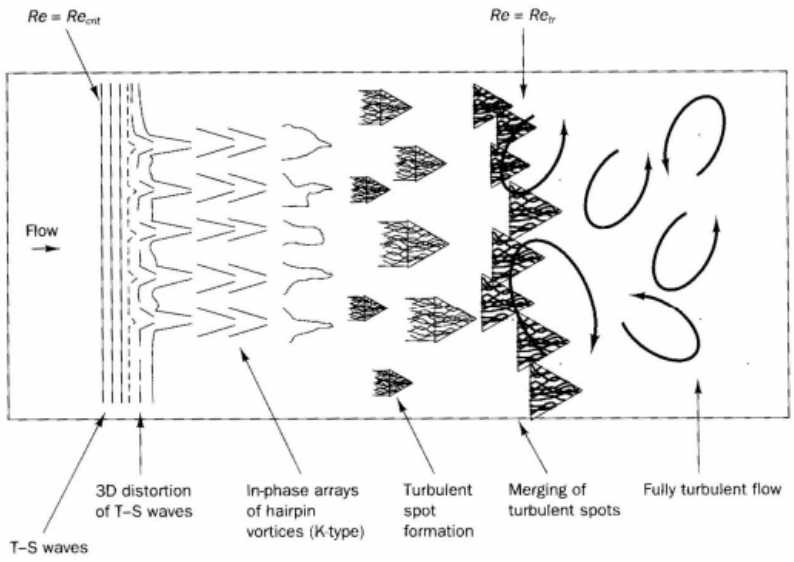

Figure 2.2: Illustration of the transition of a flow. Re_{crit} is found at the laminar instability point. From Versteeg and Malalasekera [34]

The length scales of a laminar flow is on the molecular level, while the turbulent length scales are far larger. This results in the turbulent flow being more diffusive than the laminar one. The difference in boundary in Figure 2.3 show that there will be a higher tangential velocity gradient in the turbulent case, causing increased viscous drag. However, an effect of the low velocity gradient when the flow is laminar is that it is more vulnerable to separation.

Often turbulence models ignore the transition zone, and models the flow as either laminar or fully turbulent. As the flow over an airfoil in general is both laminar and turbulent, this could be a significant source of error [6].

2.1.5 Separation

When considering airfoils the boundary layer is thin compared to the curvature of the airfoil. This makes the pressure distribution at the edge of the boundary layer very sim-

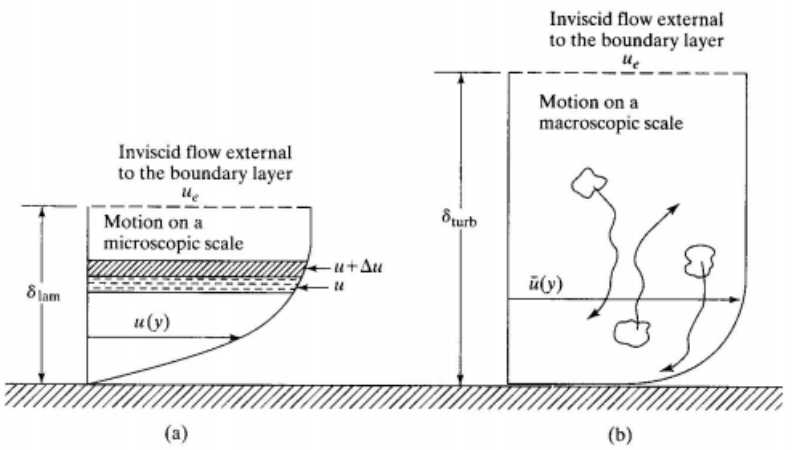

Figure 2.3: Difference in momentum transport. a) Laminar boundary layer and b) Turbulent boundary layer. From Bertin [3]

ilar to that on the airfoil itself. This leads to the conclusion that the pressure is only a function depending on the position on the airfoil. When comparing and examening pressure, the pressure coefficient is often used, it is defined as:

$$C_p = \frac{p - p_\infty}{\frac{1}{2}\rho U_\infty^2} \tag{2.4}$$

Where ρ is the density, U_∞ is the freestream velocity, p is the pressure and p_∞ is the pressure in the freestream. At the stagnation point, where the velocity is zero, the $C_p = 1$. From here, the fluid flowing over the leading edge is accelerated being drawn towards the lower pressure. At this point the pressure gradient, $\frac{dp}{dx}$, is decreasing. The fluid then reaches the minimum pressure point and begins to deaccelerate because it now faces an increasing or adverse pressure gradient. If the viscous forces has drained enough energy from the flow, or the curvature of the airfoil is large enough, the adverse pressure gradient will deaccelerate the flow to zero. If that occurs, the flow can separate, as shown in Figure 2.4.

Since the velocity is zero at the separation, point a good way to detect it is by check-

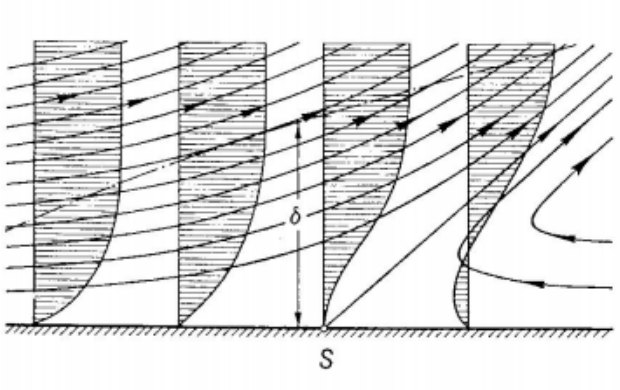

Figure 2.4: Flow approaching the seperation point, marked with an S. At the separation point, the velocit gradient is zero [20]

ing where the skin friction coefficient is zero, as the viscous friction force also has to be zero at this point. The skin friction coefficient is defined by:

$$C_f = \frac{\tau_w}{\frac{1}{2}\rho U_\infty^2} \tag{2.5}$$

where τ_w is the local wall shear stress, ρ is the density and U_∞ is the free stream velocity. In fluent the wall shear stress is calculated as an absolute value, and the skin friction coefficient will as a result always be positive. To see where separation occurs and the flow changes direction at the surface, the point where the skin friction coefficient decreases to zero before increasing again must be determined.

Since separation occurs where the flow cannot overcome the adverse pressure gradients, these areas are characterized by low pressure. As separation is most frequent on the back half of the wing, this causes high drag. The Cp curve will also flatten out at this point as the pressure no longer increase. The small and even negative velocities will increase the size of the boundary layer and hence change the effective geometry of the airfoil, often decreasing its aerodynamical efficiency.

When increasing the angle of attack the separation point will move towards the leading edge. You will eventually reach a point where the drag increases rapidly and the lift begin to decrease. This point is called stall. Depending on the airfoil and the flow this

can occur gradually or abrupt.

2.1.6 Laminar separation bubbles

In the laminar boundary layer, you have less momentum and the pressure gradients might overcome the kinetic energy, and the flow will separate around the leading edge. This will cause large disturbances in the flow, causing the transition to occur earlier. If the Reynolds number is high enough, and the curvature of the airfoil allows for it, the flow might reattach too the airfoil and cause a separation bubble [12]. However, if the curvature is high or the pressure gradients are to big, the separation bubble might burst and the flow might remain separated far downstream from the airfoil. These physics are very complicated to model and require both computational power and sophisticated models. A schematic of a laminar separation bubble can be seen in Figure 2.4.

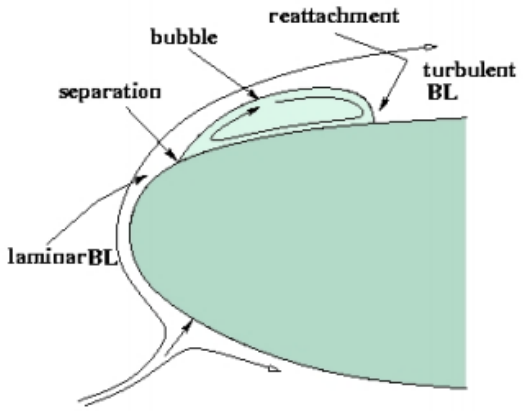

Figure 2.5: Laminar separation bubble forming. From Hu and Yang [10]

2.1.7 Near the wall

Near the wall of the airfoil the velocity profile of a turbulent boundary layer can be divided into three layers. An inner viscous layer, a middle log layer and an outer defect

layer. In Figure 2.6 a velocity profile for a turbulent boundary layer is illustrated. y^+ is the non-dimensional distance normal to the wall defined as

$$y^+ \equiv \frac{yu_\tau}{\nu} \tag{2.6}$$

where

$$u_\tau \equiv \sqrt{\frac{\tau_\omega}{\rho}} \tag{2.7}$$

where y is the distance from the wall, u_τ is the friction velocity, ν is the kinematic viscosity, τ_ω is the shear stress at the wall and ρ is the density. As can be seen from the equation 2.6 and 2.7 y^+ is dependent on the conditions in the flow, and can therefore not be calculated before running a simulation. It is important to have nodes as close to the wall as the model requires, the y^+ values therefore need to be analysed in post-processing to be sure the values are acceptable.

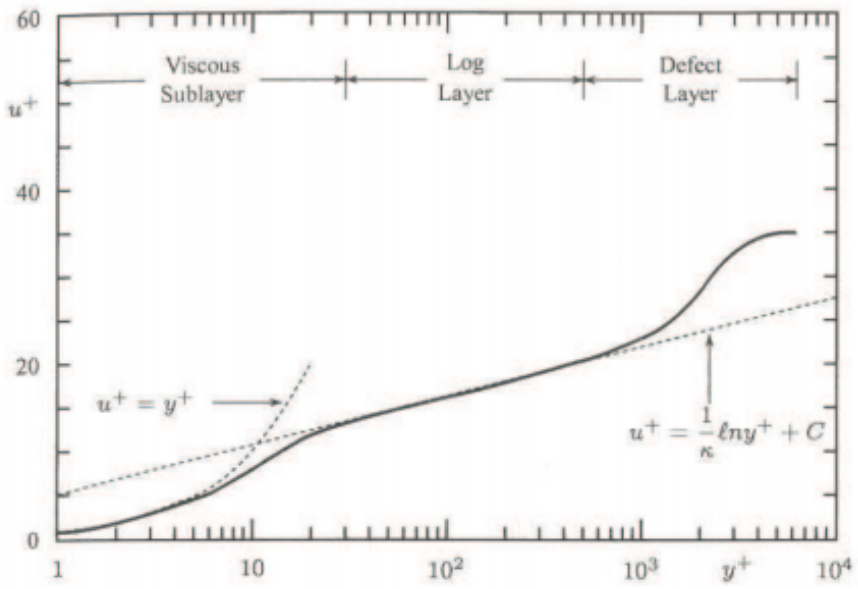

Figure 2.6: Velocity profile for a turbulent layer. From Wilcox [35]

2.1.8 Lift, Drag and Moment coefficients

The forces acting on the airfoil can be divided into a lift force acting normal to the stream wise direction and a drag force acting in the stream wise direction. In both cases, you will have to integrate both the pressure and viscous forces along the surface of the airfoil to find the total forces acting on the airfoil. These again are non-diemensionalized by dividing them by the dynamic pressure and the area. The coefficients are then given by:

$$C_d = \frac{D}{\frac{1}{2}\rho U_\infty^2 A} \tag{2.8}$$

$$C_l = \frac{L}{\frac{1}{2}\rho U_\infty^2 A} \tag{2.9}$$

Where D and L are the forces acting on the airfoil normal and parallel to the free flow direction respectively, ρ is the density, U_∞ is the free flow velocity and A is the surface area. In the wind turbine perspective, these are the forces actually creating the torque that is converted into electric energy.

The moment coefficient, or the pitching moment coefficient, is defined as:

$$C_m = \frac{M}{\frac{1}{2}\rho U_\infty^2 A} \tag{2.10}$$

where M is the moment or pitching moment. It is measured positive in clockwise direction and in this study the moment is measured around the point $\frac{x}{c} = \frac{1}{2}$ on the chord line.

2.2 Turbulence modeling

Computational fluid dynamics (CFD) tries to predict the properties of a fluid flow using numerical methods to approximate the governing equations. The base for most of the calculations are the Navier Stokes equations, which describe fluid flows. As these equations cannot be solved for almost any realistic flow, the equations need to be simplified.

When simplifying it, it is important to keep the essential parts for a correct solution. This way a good approximation can be made. The conservation laws relevant for this study are the incompressible momentum conservation

$$\rho \frac{\partial}{\partial t}(\mathbf{v}) + \rho(\mathbf{v} \cdot \nabla)\mathbf{v} = -\nabla p + \nabla \cdot (\tau) \tag{2.11}$$

and the incompressible mass conservation equation

$$\nabla \cdot (\mathbf{v}) = 0 \tag{2.12}$$

where ρ is the fluid density, t is time, $\mathbf{v}$ is the velocity vector, p is the mean pressure and τ is the viscous stress tensor.

Real flows are normally too complex to be solved by the Navier Stokes equation. This is due to turbulence, which is a normal element in flows proximate to solids, as for flow over a wind turbine blade at moderate Reynold numbers. Turbulent flow is both three dimensional, time dependent and random. The randomness makes is impossible to create a universal model that involves turbulent elements. Since real flows are too complex to be calculated, the Navier Stokes equations are simplified to make them solvable. In CFD these equations are discretized and often solved iteratively. In order to do this, the domain being studied also needs to be discretized. When a domain is discretized, smaller volumes are created over the domain being studied and the equations are solved in each smaller volume.

There exist many alternatives for modelling turbulent flow. The use of the Reynolds averaged Navier Stokes (RANS) equations has for long been the only realistic alternative due to the low computational cost of using the models. Nevertheless, with the growing computational power available, more accurate and complex models have become more accessible which give greater accuracy in their calculations. Large eddy simulation (LES) is now used in industry to some extent. However, due to the large increase in grid refinement demanded for flows over surfaces, hybrid solutions between RANS and LES (RANS/LES) models are studied with the hope of finding a balance between accurate solutions of the flow away from the walls and good modelling in the boundary layer

regions. The delayed detached eddy simulation (DES) will be used for this study. It is a hybrid RANS/LES model that can be used with many of the well known RANS models.

The following section presents the RANS models applied in combination with LES in this study.

2.2.1 Reynolds Average Navier Stokes (RANS) models

When applying a RANS model the flow variables in the instantaneous Navier-Stokes equations are divided into two groups: the mean and the fluctuation:

$$\phi = \overline{\phi} + \phi' \tag{2.13}$$

where ϕ is any scalar (as a velocity component or pressure), $\bar{\phi}$ is the mean- and ϕ' is the fluctuating part of the flow variable. The division into the two parts is often done by applying time averaging to the model, creating the mean.

The two governing equations for RANS are the averaged continuity and momentum equations (the mean bar ($\overline{u}$) is removed for simplification in 2.15):

$$\frac{\partial u_i}{\partial x_i} = 0 \tag{2.14}$$

$$\frac{\partial u_i}{\partial t} + \frac{\partial}{\partial x_j}(u_i u_j) = -\frac{1}{\rho}\frac{\partial p}{\partial x_i} + \nu\frac{\partial}{\partial x_j}\left(\frac{\partial u_i}{\partial x_j} + \frac{\partial u_j}{\partial x_i}\right) + \frac{1}{\rho}\frac{\partial}{\partial x_j}\left(-\rho\overline{u_i' u_j'}\right) \tag{2.15}$$

where p is the mean pressure, μ is the dynamic viscosity, the elements inside the square brackets are two times the elements of the mean strain-rate tensor and $-\rho\overline{u_i' u_j'}$ is the Reynolds stress. The strain-rate tensor is symmetric and by averaging it, six new unknowns are created additionally to the three mean velocities and the mean pressure. With only four equations to solve ten unknowns, different closing methods has been developed. Some of the more common ones will be discussed in the following sections.

They are based on Boussinesq hypothesis to model the Reynolds stress [35]:

$$-\rho\overline{u_i' u_j'} = \mu_t\left(\frac{\partial u_i}{\partial x_j} + \frac{\partial u_j}{\partial x_i}\right) \tag{2.16}$$

where k is the turbulent kinetic energy defined as:

$$k \equiv \frac{1}{2}\left(\overline{u_i'^2}, \overline{u_j'^2}, \overline{u_l'^2}\right) \tag{2.17}$$

where μ_t is the turbulent viscosity. This model is popular because of how efficiently it uses the turbulent viscosity for the Reynolds stress like the viscosity for the viscous stress. Performing this approximation the number of unknowns created in the time averaging is reduced to two. Acquiring the extra equations needed to close the problem has spawned many models.

The first equation is the turbulent kinetic energy equation. Some models, like Spalart-Allmaras, only use this equation. To use the model some additional information about the flow would be needed, often the length scale. The second equation is typically used to calculate another turbulent property of the flow. It could be the turbulent length scale, the dissipation rate, ϵ, like in $k-\epsilon$, or dissipation rate per unit turbulent kinetic energy, ω, like in the $k-\omega$ model. There are also even more complex models combining the strengths of the other, like the Shear Stress Transport (SST) model.

This study will focus on:

- Spalart-Allmaras
- $k-\epsilon$
- SST $k-\omega$

These models will give a wide range of complexity, accuracy, strengths and weaknesses. In Fluent all these models assume turbulent flow in the whole domain. While Spalart-Allmaras is the simplest one, it is tailor made for flow over an airfoil. $k-\epsilon$ has been the most widely used turbulence model in commercial codes, but has limitations

in the near wall treatment. SST $k-\omega$ is the most complex model used in this study, but is getting more and more popular, also in commercial use, as the computational power rises. In this study, the same grid will be applied for all models and all models will be used all the way up to the wall, not using any wall functions.

Spalart Allmaras

The Spalart-Allmaras turbulence model is a one-equation model developed for aerodynamic applications. A single transport equation is solved for the kinematic eddy viscosity ν_T resulting in efficient computation of the boundary layer. The model has proven to give good results in boundary layer flows with adverse pressure gradients, in particular in external flows over airfoils. It is also becoming more popular for turbo-machinery applications [**?**]. However, the model has its limitations, and due to difficulties when predicting length scales, the model is not suitable for industrial and free shear flows. The transport equation for the eddy viscosity is expressed as [15]:

$$\frac{\partial(\rho\tilde{\nu})}{\partial t}+\frac{\partial\rho\tilde{\nu}u_i}{\partial x_i}=G_{\tilde{\nu}}+\frac{1}{\sigma_{\tilde{\nu}}}\left[\frac{\partial}{\partial x_j}\left\{(\mu+\rho\tilde{\nu})\frac{\partial\tilde{\nu}}{\partial x_j}\right\}+C_{b2}\rho\left(\frac{\partial\tilde{\nu}}{\partial x_j}\right)^2\right]-Y_\nu+S_{\tilde{\nu}} \tag{2.18}$$

where $G_{\tilde{\nu}}$ is the turbulent viscosity production, Y_ν is the destruction of turbulent viscosity, $S_{\tilde{\nu}}$ is the source term, ρ is the density and $\sigma_{\tilde{\nu}}$ and C_{b2} are constants.

By default, in ANSYS Fluent, the scalar measure of the deformation tensor in the turbulent production modelling is formulated as in the original model by Spalart and Allmaras [28]. It is based on the magnitude of the vorticity. ANSYS Fluent additionally offers a modified formulation of the scalar measure of the deformation tensor that combines the measures of both vorticity and the strain tensors [7]. The objective is to make sure that the production of eddy viscosity is reduced in regions where the strain rates are exceeded by measured vorticity. This is often the case inside vortices.

Turbulent flows often involve streamline curvature and system rotation. The standard Spalart Allmaras model is insensitive to these elements. This can lead to errors in calculation of the eddy-viscosity in these sorts of flows. ANSYS Fluent therefore offers an option that includes curvature correction [7] for calculation of the turbulence pro-

duction term in the Spalart Allmaras model. This curvature correction option is closely related to the modification of the production term derived by Spalart and Shur in [26] and by Shur et al. in [24].

The Spalart Allmaras turbulence model has proven to give good results for boundary layer flows with adverse pressure gradients as well as for external flows, as over an airfoil. Additionally, it has been shown to be useful for turbo-machinery applications [15]. The model's disadvantages are difficulties predicting the length scale that makes them less useful for industrial and free shear flows.

$k-\epsilon$ model

The k-ϵ-model is a two-equation model that is frequently used in the field of CFD. The model looks at the mechanisms which influence the kinetic energy of the turbulent flow (k). It sums up the various transports of k and production of k and subtract the turbulent dissipation rate (ϵ). The model gives good predictions in the fully developed turbulent regions, but show excessive levels of turbulent shear stress in areas close to walls and stagnation points. Other limitations including reduced accuracy in flows with adverse pressure gradients are described in [2].

The k-transport equations:

$$\frac{\partial}{\partial t}(\rho k)\frac{\partial}{\partial x_i}(\rho k u_i) = \frac{\partial}{\partial x_j}\left[\left(\mu + \frac{\mu_t}{\sigma_k}\right)\frac{\partial k}{\partial x_j}\right] + G_k + G_b - \rho\epsilon - Y_M + S_k \tag{2.19}$$

and the transport equation for its dissipation rate (ϵ):

$$\frac{\partial}{\partial t}(\rho\epsilon)\frac{\partial}{\partial x_i}(\rho\epsilon u_i) = \frac{\partial}{\partial x_j}\left[\left(\mu + \frac{\mu_t}{\sigma_\epsilon}\right)\frac{\partial \epsilon}{\partial x_j}\right] + C_{1\epsilon}\frac{\epsilon}{k}(G - k + C_{3\epsilon}G_b) - C_{2\epsilon}\rho\frac{\epsilon^2}{k} + S_\epsilon \tag{2.20}$$

Where G_b is the turbulence kinetic energy generation from buoyancy, Y_M is the contribution of the fluctuating dilatation in compressible turbulence, σ_k is the turbulent Prandtl number for k, σ_ϵ is the turbulent Prandtl number for ϵ and $C_{1\epsilon}$, $C_{2\epsilon}$ and $C_{3\epsilon}$ are

constants. Both the Prandtl numbers and the constants have default settings in ANSYS Fluent and where not modified.

The model gives good predictions in the fully developed turbulent regions, but show excessive levels of turbulent shear stress in areas close to wall and stagnation point.

$k-\omega$ model

The $k-\omega$ model is a two equation model that is frequently used in the field of fluid dynamics. It specializes in boundary layer flows and performs very well at in this region. However, it struggles dealing with non-turbulent free-stream boundaries. The model looks at the mechanisms which influence the kinetic energy of the turbulent flow (k) and at the dissipation rate (ω), also called the turbulent frequency ($\omega = \frac{\epsilon}{k}$). The transport equations for k and ω respectively can be formulated as:

$$\frac{\partial}{\partial t}(\rho k) + \frac{\partial}{\partial x_i}(\rho k u_i) = \frac{\partial}{\partial x_j}\left(\Gamma_k \frac{\partial k}{\partial x_j}\right) + G_k - Y_k + S_k \tag{2.21}$$

$$\frac{\partial}{\partial t}(\rho \omega) + \frac{\partial}{\partial x_i}(\rho \omega u_i) = \frac{\partial}{\partial x_j}\left(\Gamma_\omega \frac{\partial \omega}{\partial x_j}\right) + G_\omega - Y_\omega + S_\omega \tag{2.22}$$

Where G_k is the turbulence kinetic energy generation from mean velocity gradients, G_ω is the generation of ω, Γ_k and Γ_ω is the effective diffusivity of k and ω respectively which is dependent on the turbulent viscosity, μ_t, Y_k and Y_ω are the dissipation of k and ω respectively due to turbulence and S_k and S_ω are source terms.

$k-\omega$ shear stress transport (SST) model

The $k-\omega$ F.R. Menter's shear stress transport (Menter's SST) model combines the benefits from both the $k-\epsilon$ model and the $k-\omega$ model with the goal of increasing the overall performance. The model use $k-\epsilon$ in the free stream region and ω in the boundary layer region close to surfaces. Both $k-\epsilon$ and $k-\omega$ is two equation models, making $k-\omega$ SST a two equation eddy-viscosity model. The crossover between the two models is made

possible by introducing a cross-diffusion term to the ω/ϵ equation:

$$\frac{\partial}{\partial t}(\rho\omega) + \frac{\partial}{\partial x_i}(\rho\omega u_i) = \frac{\partial}{\partial x_j}\left(\Gamma_\omega \frac{\partial \omega}{\partial x_j}\right) + G_\omega - Y_\omega + D_\omega + S_\omega \tag{2.23}$$

Where

$$D_\omega = 2(1 - F_1)\rho \frac{1}{\omega \sigma_{\omega,2}} \frac{\partial k}{\partial x_j} \frac{\partial \omega}{\partial x_j} \tag{2.24}$$

and F_1 is a blending function dependent on the distance to the surface and $\sigma_{\omega,2}$ is a constant. Additionally, the turbulent viscosity μ_t is modified with a limiter for the formulation of the eddy-viscosity giving a more correct calculation of the diffusivity.

2.2.2 Large eddy simulation (LES)

LES is a technique that directly computes the large eddies by numerically solving the Navier-Stokes equations, while the smaller eddies are modelled. This way, the calculation takes far less Central Processing Unit (CPU) time than if every eddy were to be solved directly, as in the direct numerical simulation (DNS), but still greater than if a RANS model were used. LES has no limitations in free flow calculations as increasing the grid resolution will bring it closer to a DNS solution [22]. LES is motivated by the logic that almost all the momentum, mass and energy is transported by the large eddies and they cannot be generalized because of their case dependency and anisotropic nature. At the same time, small eddies are more universal and can therefore be successfully modelled. In LES the time averaging of the momentum equations, which is normally used in RANS, is exchanged for a spacial averaging for the large eddies to be resolved directly, and the smaller eddies to be modelled. There exist various sub-grid scale (SGS) models and, as with RANS models, they are often based on a Boussinesq approximation. Thereby, the effect the small eddies has on the large eddies is captured and accounted for in the calculation. Still, results of a LES calculation are more dependent on the grid resolution than on the SGS model [22]. The default SGS-model for ANSYS Fluent is the Wall-Adapting Local Eddy-Viscosity (WALE) model [14] which

employs the Boussinesq hypothesis. It models the eddy viscosity as:

$$\mu_t = \rho L_s^2 \frac{\left(S_{ij}^d S_{ij}^d\right)^{3/2}}{\left(\overline{S}_{ij}\overline{S}_{ij}\right)^{5/2} + \left(S_{ij}^d S_{ij}^d\right)^{5/4}} \ , \tag{2.25}$$

where

$$L_s = min\left(\kappa d, C_w V^{1/3}\right) \tag{2.26}$$

and

$$S_{ij}^d = \frac{1}{2}\left(\overline{g}_{ij}^2 + \overline{g}_{ij}^2\right) - \frac{1}{3}\delta_{ij}\overline{g}_{kk}^2 \ , \ \overline{g}_{ij} = \frac{\partial \overline{u}_i}{\partial x_j} \tag{2.27}$$

where $\overline{S}_{ij}$ is the rate-of-strain for the resolved scale and C_w, the WALE constant, is set to 0.325 as default in ANSYS Fluent based on validation completed by a European Union research project [7]. $\kappa = 0.41$ is the von Kármán constant, d the distance to the wall and V the volume of the grid cell.

LES can be used with a much coarser grid than DNS, since the small eddies are modeled. LES is still more expensive than RANS. This is especially the case for wall bounded flows, where the grid resolution has to be greatly improved to capture the eddies for LES. Here even the large eddies are so small that the grid resolution needs to be greatly increased, which again increases the computational cost. An alternative approach exists, where the increased grid resolution issue is solved for wall bounded flow. This is the simulation used for this study and it is described in the next section.

2.2.3 Detached eddy simulation (DES)

DES is designed for wall bounded flow by applying a RANS model in the attached boundary layer while LES is applied in detached flow and free flow. This way, the grid resolution can be greatly reduced compared to using pure LES. DES is a hybrid model between RANS and LES, and the switch between the two approaches is done by a re-definition of the length scale. In DES with the Spalart Almaras RANS model, the length scale is

defined as:

$$\tilde{d} = min\Big(d, C_{DES}\Delta_{max}\Big), \tag{2.28}$$

where

$$\Delta_{max} = max\Big(\Delta x_i, \Delta x_j, \Delta x_l\Big) \tag{2.29}$$

Here d is the distance to the wall, C_{DES} is an empirical constant set to 0.65 [22] and Δ_{max} is the maximum grid spacing of the grid cell considered. For different RANS models, the length scale is defined differently. The C_{DES} will also vary as the accuracy offered by the model applied will change [22]. The goal for all of the length scales is to use RANS in attached boundary layer flow, and LES elsewhere. When $d < C_{DES}\Delta_{max}$ the model will run the RANS part of the model, and LES otherwise.

In DDES a different definition of the length scale is used in order to continue to use the RANS model throughout the boundary layer.

$$\tilde{d} = d - f_d max\Big(0, d - C_{DES}\Delta_{max}\Big), \tag{2.30}$$

where

$$f_d = 1 - \tanh\big(\Big(8r_d\Big)^3\big) \tag{2.31}$$

and

$$r_d = \frac{\tilde{\nu}}{\sqrt{U_{i,j}U_{i,j}}\kappa^2 d^2} \tag{2.32}$$

Chapter 3

Numerical Methods

Some of the sections in this chapter are partly taken from [16].

In this study, the software ANSYS Fluent Version 16.2 was the main numerical solver used in calculating the solution. Using this software, there are many parameters to consider which could affect your solution. Through this chapter, both what choices were made and the reasoning behind the choices will be presented.

3.1 Finite Volume Method

ANSYS Fluent uses the finite volume method where the integral form of Navier-Stokes is discretized. In this method, the integral form of the steady transport equation is considered:

$$\nabla(\rho \mathbf{u}\phi) = \nabla \cdot \left(\Gamma \nabla \phi\right) + S_\phi \tag{3.1}$$

where ρ is the density,ϕ is the variable, u is the velocity of the fluid, Γ is the diffusion coefficient and S_ϕ is the source term. The equation is then integrated over the control

volume, CV, with boundary A

$$\int_{CV} \nabla(\rho \mathbf{u}\phi)dV = \int_{CV} \nabla \cdot (\Gamma \nabla \phi) + S_\phi \tag{3.2}$$

applying the Gauss theorem

$$\int_V \nabla \cdot \mathbf{F} dV = \int_A \mathbf{n} \cdot F dA \tag{3.3}$$

equation 3.2 can then be expressed as

$$\int_A \rho\phi \mathbf{u} \cdot \mathbf{n} dA = \int_A \Gamma \nabla \phi \cdot \mathbf{n} dA + \int_{CV} S_\phi dV \tag{3.4}$$

and then integrated over the boundaries

$$\sum_f (\rho\phi \mathbf{u} \cdot \mathbf{n})_f = \sum_f (\Gamma \frac{\partial \phi}{\partial n} A)_f + S_\phi V_p \tag{3.5}$$

where f denotes the faces of the quadrilateral control volume and V_p its area. Interpreting this we can see that the finite volume method says that the flux difference between the faces is equal in convective and diffusive terms. The method can be expanded to higher dimensions using the same approach, only increasing the number of faces.

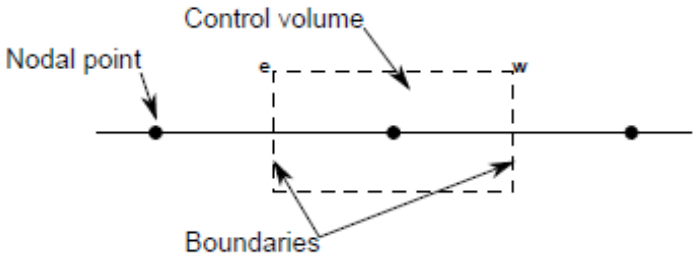

Figure 3.1: Example of a one dimensional control volume. From Tveiteraas [33].

3.2 ANSYS Fluent settings

In this study the Reynolds number will be varied frem $5 \cdot 10^4 - 10^6$ for the full Reynolds number dependency study. The grid dependence study, section 4.6, and the sensitivity analysis, chapter 5 will be conducted at Reynolds number 10^5, to compare it with both experimental and numerical results from NTNU and DTU.

The pressure based solver is used, where a pressure equation is derived from the Navier-Stokes equations. The velocities are chosen to be given in an absolute formulation. Air at 15 degrees Celsius is the modelled fluid, while the airfoil is modelled as a wall. The reference values are given in Table 3.1

Table 3.1: Reference values. The chord length decides the length, while the density and dynamic viscosity are properties of air at 15 degrees celsius. The reference velocity varies with the Reynolds number and is decided by the inlet velocity.

Parameter	Value
Length	1 m
Density	1.225 $\frac{kg}{m^3}$
Dynamic viscosity	1.802 $\frac{kg}{m\cdots}$

3.2.1 Relaxation factors

The relaxation factors decide how big the changes of flow properties are for each iteration.

$$\phi_{new} = \phi_{old} + \beta\delta_\phi \tag{3.6}$$

where ϕ is a variable, δ_ϕ is the computed change and β is the relaxation factor. If the relaxation factor is too big and the properties changes too much, the solution might diverge. Tuning the relaxation factor down can help the calculation towards converging. In this thesis the values are mostly kept at their default values except in a very few diverging cases. In these cases, the values will be specified.

3.2.2 Boundary Conditions

The boundary conditions (BC) decide the initial conditions for the outer boundaries of the domain. When modelling true free flow conditions all BCs where set to either velocity-inlets, pressure outlets or walls, as there is no reason to expect any symmetry or periodicity in this study. The west C-shaped boundary is set as the inlet, while the outlet is set to a pressure outlet with zero gauge pressure. The boundary conditions on the top, bottom, front and back of the geometry are set to slip walls, the specified shear are set to zero in all directions. This is done to try to replicate the walls in the wind tunnel, without needing to refine the mesh to capture the boundary layer effects, as would have been the case if the windtunnel walls had been modelled with the no-slip condition. These boundary conditions also make the comparison with the LES study from DTU more comparable as they have used the same boundary conditions for mimicking the top and bottom walls of the windtunnel. The inlet velocity is dependent on the Reynolds number and is specified in each case. The turbulent characteristics are specified by the turbulent intensity and turbulent length scale. Turbulent intensity is a measure on the relationship between the velocity fluctuations and the average velocity

$$TI \equiv \frac{u'}{u_{avg}} \tag{3.7}$$

where u' is the root mean square of the velocity fluctuations and u_{avg} is the average velocity [8]. TI is dependent on the flow and is set based on measured quantities in the different wind tunnels. For the simulations referring to the low wind speed tunnel at NTNU the values are based on what was measured Aksnes' master thesis [1].

Turbulent length scale is describing the size of the large eddies in a flow. It is believed to be of the same order as the cord length [33], which is 1m.

For the direct comparisons with the wind tunnels, the walls are modelled with slip condition as to compensate for the growing boundary layer without having to refine the grid in these areas. The backflow turbulent levels are always set similar to the inlet values. The walls are modelled with zero roughness [1], and the airfoil has the no-slip condition.

3.2.3 Spatial discretization

The finite volume method needs the value of the flow at the faces, and since the value are stored at the nodes, a good interpolation scheme is needed. To calculate the face values the values in the surrounding are used. The setup is illustrated in Figure 3.2

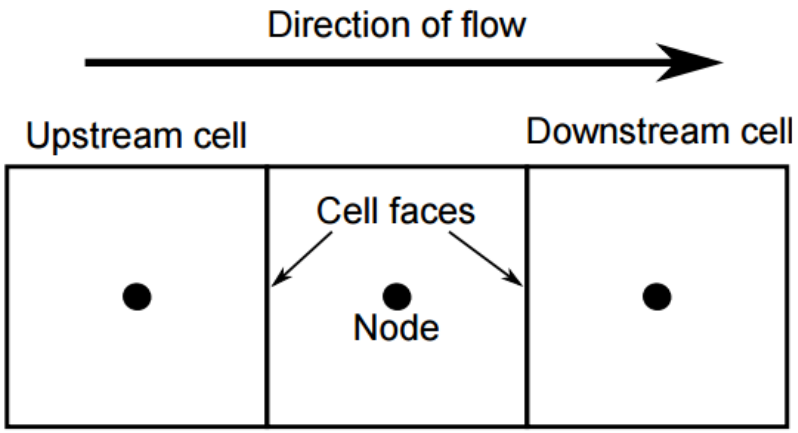

Figure 3.2: Nodal points upstream and downstream of cells to be interpolated. From Tveiteraas [33]

Since the information travels mostly downstream, the scheme should focus on what is happening upstream when interpolating the face values [7]. When using DES in fluent the momentum term has to be calculated by the Bounded Central differencing (BCD) scheme. For all the other convective terms the second order, Monotonic Upstream-Centered Scheme for Conservation Laws (MUSCL) and BCD schemes are tested and compared concerning accuracy and computational costs. Second order is known to be far more robust and accurate than the first order version. The higher order options is not expected to give an improvement on accuracy in the type of flow investigated here [8], but will be tested to make sure.

3.2.4 Gradient scheme

The gradient of the variables are used to determine diffusive fluxes, velocity derivatives and in higher-order discretization schemes. In ANSYS Fluent there are three options:

- Green-Gauss Cell-Based
- Green-Gauss Node-Based
- Least-Squares Cell-Based

The latter two give more accurate results than the Green-Gauss Cell based scheme. Even though the Least-Squares Cell-Based scheme is the fastest of the two, looking at computational costs, in a structured grid like the one used in this study, the Green-Gauss Node-Based scheme should have a better accuracy [8]. Both are therefore tested and compared in both categories.

3.2.5 Pressure interpolation scheme

The pressure interpolation is needed so the pressure can influence the velocity even though they are both defined at the center of each cell. The options for this interpolation in ANSYS Fluent are:

- Standard
- Linear
- Second-Order
- Body force weighted
- PRESTO! (Pressure staggering option)

The standard and linear schemes are the most inaccurate ones and use the momentum equation and average values of the adjacent cells respectively to calculate the face values [17]. Body force weighted is better when large body forces are apparent. PRESTO! is best in flows with very steep pressure gradients [7] and second-order is recommended for good overall accuracy [8]. The latter two are tested and compared in this study.

3.2.6 Pressure-velocity coupling

The governing Navier-Stokes equations that Fluent is trying to solve here consists of the continuity equation (2.12) and the momentum equations (2.11). As the pressure cannot be solved by the continuity equation, a pressure-velocity scheme is needed. Fluent can solve this by four different methods:

- Semi Implicit Method for Pressure Linked Equations (SIMPLE)
- Semi Implicit Method for Pressure Linked Equations Correction (SIMPLEC)
- Pressure-Implicit with Splitting of Operators (PISO)
- Fractional Step Method (FSM)

The SIMPLEC and PISO algorithms are modified versions of SIMPLE. PISO specializes in unsteady flow and SIMPLEC is limited to simple problems, preferably laminar. FSM is a coupled scheme also aimed at unsteady flows. Below is an outline of the different steps used in SIMPLE [33]:

1. Start with starting values; p^*, u^*, v^*
2. Solve momentum equations to get the new u^* and v^*
3. Solve pressure correction equation for p'
4. Calculate correction terms u' and v'
5. Correct p, u and v
   $p = p^* + \alpha_p p'$
   $u = u^* + u'$
   $v = v^* + v'$
6. Update p^*, u^* and v^* by p, u and v
7. Repeat from 1. until solution has converged

Where p is the pressure, p', u' and v' are the correction terms and p^*, u^* and v^* are the preliminary pressure and velocity components respectively. Since unsteady flows often need many repetitions for the momentum balance to be satisfied, the PISO algorithm aim to improve the efficiency of the SIMPLE scheme by adding the neighbour and skewness correction.

The neighbour correction moves the repeated calculation above inside the solution stage of the pressure-correction equation [7], while the skewness correction helps with the convergence of skewed cells.

In this study we have a transient formulation with a grid which have some degree of skewness to it, so the PISO algorithm is the recommended one [33]. Although it uses a little more CPU per iterations than SIMPLE, it can drastically reduce the amount of iterations. SIMPLE will also be tested to see how it affects accuracy and computational costs.

3.2.7 Time-Advancement Algorithm

The discretized form of the transport equation for a variable ϕ in a time-dependent flow is:

$$\int_V \frac{\partial \rho\phi}{\partial t} dV + \oint \rho\phi \mathbf{v} \cdot d\mathbf{A} = \oint \Gamma_\phi \nabla\phi \cdot d\mathbf{A} + \int_V S_\phi dV \tag{3.8}$$

where ϕ is the transported variable ρ is the density, $\mathbf{v}$ is the velocity vector, $\mathbf{A}$ is the surface area vector, Γ_ϕ is the diffusion coefficient for ϕ, $\nabla\phi$ is the gradient of ϕ and S_ϕ is the source of ϕ per unit volume.

Since we are applying the pressure based solver, the standard approach is that all convective, diffusive and source terms are calculated for the time level n+1.

$$\int_V \frac{\partial \rho\phi}{\partial t} dV + \oint \rho^{n+1}\phi^{n+1}\mathbf{v}^{n+1} \cdot d\mathbf{A} = \oint \Gamma_\phi^{n+1} \nabla\phi^{n+1} \cdot d\mathbf{A} + \int_V S_\phi^{n+1} dV \tag{3.9}$$

The total time discretization error is divided into both how the temporal discretization is made up and how the time-advancement scheme used to advance the solution to the next time step.

Time-advancement scheme

In an iterative time-advancement scheme for each time step, the equations are solved iteratively until either a convergence criterion is met or a constraint on the number of iterations per time step is met. The latter condition was used in this study, and this was often the limiting factor as the criteria was set to maximum 20 iterations per time step. This iterative method is the default scheme in ANSYS Fluent and is exclusively used in this study, see Figure 3.3.

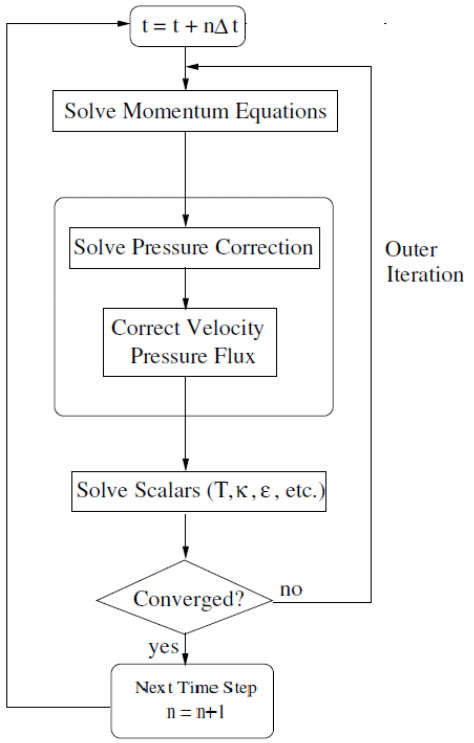

Figure 3.3: Overview of the iterative time advancement scheme from the Fluent theory guide [7]

Since this method needs many iterations per time it has a high computational cost. Fluent therefore has another option that is a Non-Iterative Time Advancement method, where the philosophy is that you only need to reduce the error to the same order as

the truncation error. The NITA scheme only performs one outer iteration per time step, illustrated in Figure 3.4, although it needs some inner iterations to solve the individual set of equations, this speeds up the computational time significantly.

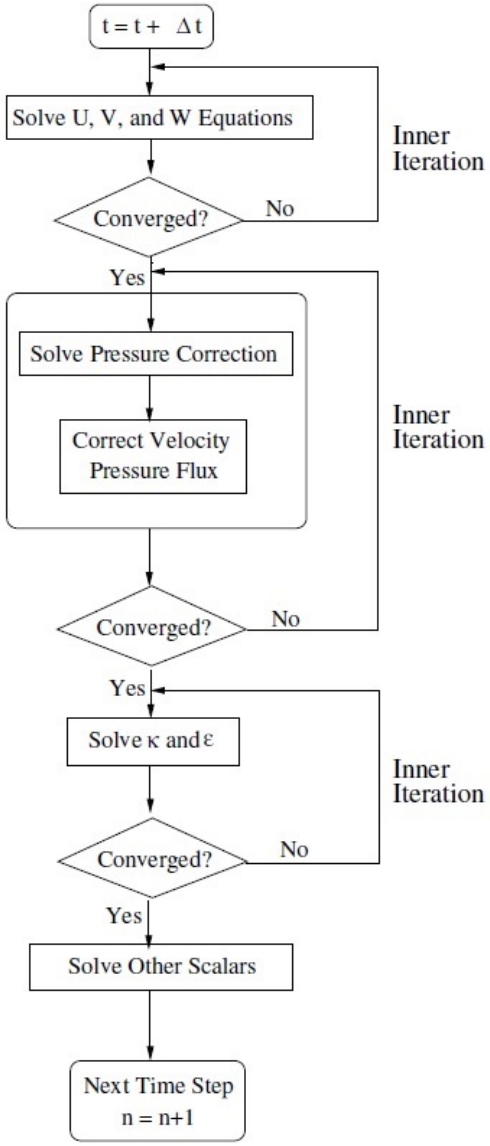

Figure 3.4: Overview of the non-iterative time advancement scheme from the Fluent theory guide [7]

Temporal Discretization

For transient simulations, the equations must be discretized in time as well as in space. The temporal discretizations over each timestep involves the integration of every term in the equations. When using DES the Bounded Second Order Implicit Time Integration scheme is recommended and used throughout this study. A brief explanation is shown below.

An independent variable ϕ in time is described by

$$\frac{\partial \phi}{\partial t} = \frac{\phi_{n+\frac{1}{2}} - \phi_{n-\frac{1}{2}}}{dt} \tag{3.10}$$

$$\phi_{n+\frac{1}{2}} = \phi_n + \frac{1}{2}\beta_{n+\frac{1}{2}}(\phi_n - \phi_{n-1}) \tag{3.11}$$

$$\phi_{n-\frac{1}{2}} = \phi_{n-1} + \frac{1}{2}\beta_{n-\frac{1}{2}}(\phi_{n-1} - \phi_{n-2}) \tag{3.12}$$

where n, $n-1$, $n-2$, $n+\frac{1}{2}$ and $n-\frac{1}{2}$ are different time levels, $\beta_{n+\frac{1}{2}}$ and $\beta_{n-\frac{1}{2}}$ are bounding factors for each variable at the respected timestep. For turbulent flows the bounded variables include turbulent kinetic energy, dissipation rate and specific dissipation rate. This method cannot be used in density-based solver or with moving and/or deforming meshes.

Chapter 4

Grid generation and time stepping

Some of the sections in this chapter are partly taken from [16].

As important as choosing the right turbulent model and the solver setting is how the grid, that discretizes the geometry, is built up. Especially when using DES as the grid quality not only improves the resolution of the solution, but is also a deciding factor on whether RANS or LES is used in the calculations. A grid cannot be generically made for all different cases, since the quality is dependent on the shape of the airfoil, what kind of flow that is being modelled and the Reynolds number among others. The grids used in this study where created in ANSYS griding which uses a collocated grid where both the pressure and velocity are defined at the center of each cell.

In this chapter both the grid setup and the grids used in this study will be discussed, the time stepping size and the total amount of time steps is also a central theme as it is closely linked to the grid. There will also be a section on the grid-quality and how to improve it.

4.1 Structured vs unstructured

In 3D, a structured grid is built up by hexahedra cells, while an unstructured grid typically has tetrahedon cells. Although it may consist of hexahedra cells as well. A third possibility is the hybrid grid where there are areas of the domain covered by structured grid and the rest covered by an unstructured grid. Examples of these possibilities are illustrated in Figure 4.1.

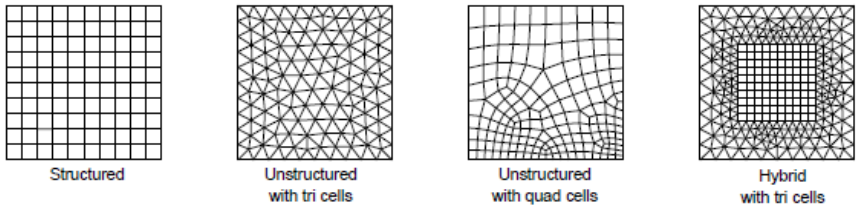

Figure 4.1: Different grid setups. The structured grid shown is a Cartesian grid and can be varied from this simple form, from[33]

.

The advantage of the unstructured grid is that it easier adapts to complex geometries. It can follow the geometry locally without caring for the rest of the geometry. In addition, it is easier to control the size of the cells in certain areas, in contrast to the structured grid that often ends up with an abundance of cells in areas where it is not needed. The advantage of structured grids, if they can be applied, are that far less memory is needed to store and that they in general require less memory and computational time than the unstructured version. As this study considers only one airfoil, but require a lot of computational time, a structured grid is used.

4.2 Grid quality

The quality of the grid is important to obtain a high quality solution. A grid with more cells will in general give a better solution, while a coarser grid will converge faster and use less computational power, although it might not converge at all or the converged solution might be very inaccurate. The reason why the coarser grid solution is more

inaccurate is that the larger cells might miss the small vortices or diffuse them because of numerical diffusion. Consequently, the grid should be fine in the areas with higher gradients and coarser in the remote parts of the domain. While constructing the grid it is important not to skew the grid too much, as this will have a negative impact on the solution.

Fluent measures the quality of the grid in aspect ratio and orthogonal quality. The aspect ratio is the ratio between the longest and shortest side of a cell. In Figure 4.3 different aspect ratios from smallest to largest are illustrated.

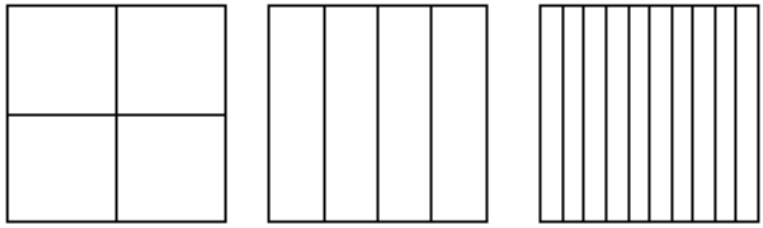

Figure 4.2: Three different aspect ratios from smallest to largest, from [33]

The reason why some of the cells have a big aspect ratio is that the velocity gradients vary in the various directions. There might for example be huge gradients in the direction normal to the airfoil, while the gradients are small parallel to the surface of the airfoil. The grid then needs to be finer in the normal direction than in the parallel direction. In crucial areas, the aspect ratio should be kept not higher than 10, while it is acceptable to have a much higher aspect ratio further from the airfoil.

Orthogonal quality is how skewed a cell is, illustrated in Figure 4.3. The measure on this is how much the angle between the different sides of the cell deviates from 90 degrees. ANSYS Fluent gives this as a number between 1 and 0, where 1 is good and 0 is bad. It will give a warning if the value is below 0.01. It is important to keep in mind that even if the general grid quality is low, this might be affected by local cells and if placed far away from the airfoil, might not affect the solution noticeably.

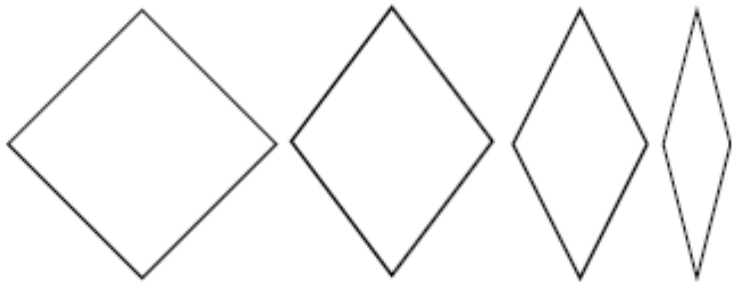

Figure 4.3: Different cell skewness. The orthogonality quality is decreasing towards the right. From [33]

4.3 C-grid

Throughout this study, a C-grid is used to model the flow. The C-grid gets its name from it characteristic shape in front of the airfoil as illustrated in Figure 4.4. Using this type of mesh the whole domain can be discretized in a structured grid as well as keeping the skewness of the cells at a reasonable level. However, as seen in Figure 4.4 the side effect is the abundance of cells in normal direction from the tail and behind the trailing edge towards the outlet.

With a C-mesh it is very easy to get good resolution in the boundary layer as can be seen in Figure 4.5.

Another alternative would be to use an O-grid. Where the geometry forms a circle around the airfoil. In general, this leads to fewer total cells, but might lead to cells with an extremely high skewness, especially at the trailing edge of the airfoil.

The drawback of using a C-grid in an angle of attack study is that there is no part of the grid you can rotate compared to the boundaries. The two approaches to changing the angle of attack is then either changing the direction of the velocity at the inlet or building a completely new geometry where the airfoil is tilted differently for each angle of attack. The first approach might be an acceptable approximation if free flow is modelled, as the boundaries around the airfoil then can be put as inlets or outlets depending on where the flow is approaching from. However, when replicating a wind tunnel, as is

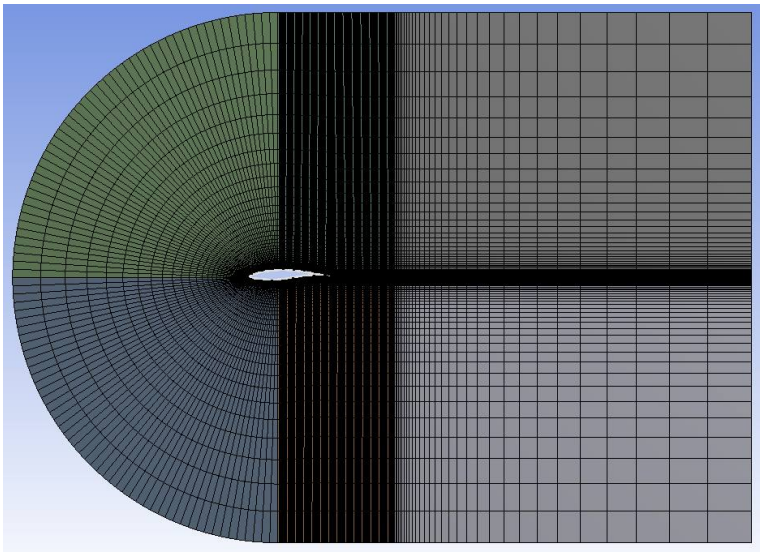

Figure 4.4: Plot of one of the C-grids applied in this study.

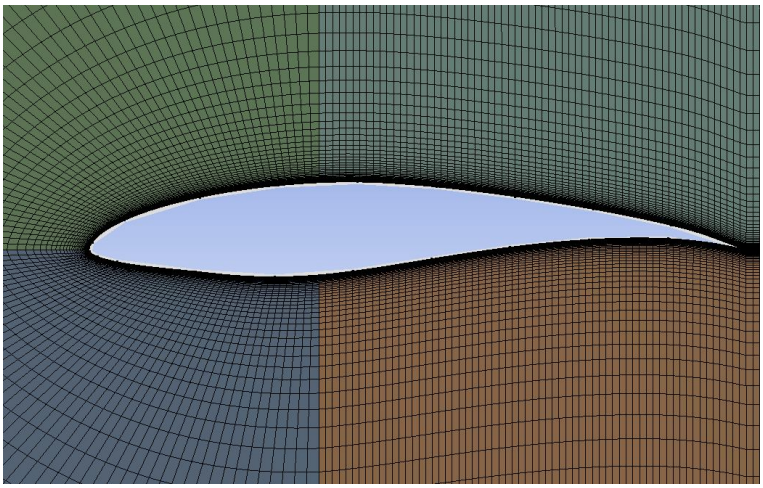

Figure 4.5: Close-up of the grid around the airfoil.

done in this study, the approximation is considerably worse. The flow will bend around the walls, diminishing the effect of the incoming angle of the flow. This will result in coefficients giving the impression of a lower angle of attack than what is really wanted.

In this study, it was therefore chosen to do it using the first approach. Trying to keep the grid as similar as possible to each other when creating the different geometries it

was chosen to not have one horizontal slice through the whole middle geometry, but rather have one horizontal slize going from the inlet to the leading edge, and another one going from the trailing edge to the outlet, illustrated in Figure 4.6. This decision also improves the orthogonality factor compared to keeping the one horizontal slice.

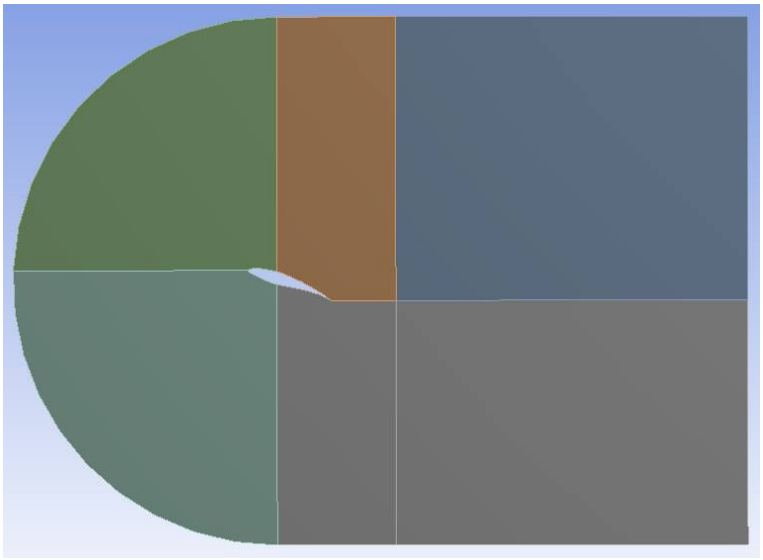

Figure 4.6: The domain for angle of attack = 8°.

4.4 Grid setup

The dimensions of the flow domain used in this study is based on the experiments in the NTNU wind tunnel, which will be the main validation source. One additional domain with boundaries further away from the airfoil was used to test the approximation towards free flow.

To more easily manage the cells around the airfoil, as well as improving the orthogonality of the cells even more, the domain was divided into six different quadrants instead of the usual four used in C-meshes, as can be seen in Figure 4.6. This leads to more parameters needing to be adjusted when the grid is too changed. When sizing a segment both number of divisions and bias factor were set. The bias factor is defined as the ratio between the largest and smallest cells on the edge. All the edges were defined

such that the cells becomes smaller the closer you come to the airfoil. Since the grid is structured, the edges not labeled in Figure 4.7 is decided by symmetry.

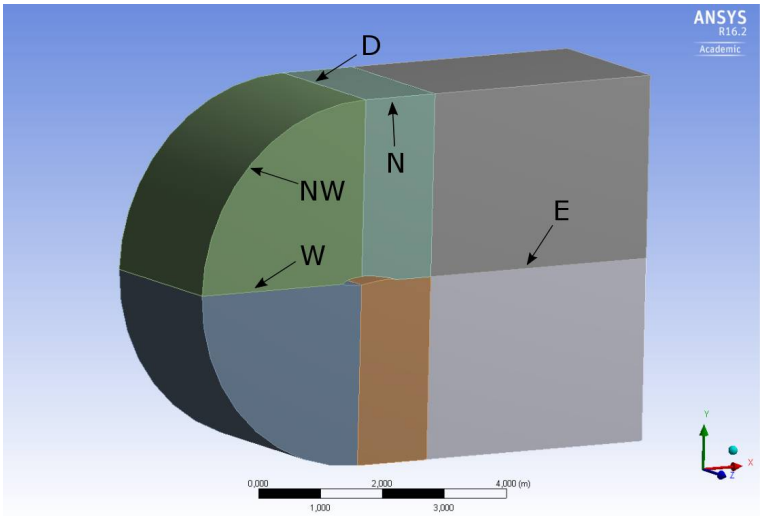

Figure 4.7: The six quadrants together with the named segments that need initialization. N is North, NW is North West, W is West, E is East and D is Depth. The rest of the segments in the geometry are decided by the symmetry of the structured grid.

The grid used to determine the time step size and amount of time steps needed to get the correct converging solution is based on the grid used in the 2D investigation of the same airfoil conducted by one of the authors earlier [16]. As many of the same turbulence models are used close to the wall, it is assumed that the refinement requirements are rather similar and that the condition $y^+ \leq 1$ holds for the grid points adjacent to the airfoil wall. After deciding the proper time step sizes, the grid will be refined and the time step sizes with it.

The boundary conditions were dictated by the conditions in the experimental setup at NTNU, as this is the main validation source. The different boundary faces are shown in Figure 4.8 and the different type of boundary assigned to each face is tabulated in Table 4.1. The parameters used at the inlet and outlet are shown in Table 4.2 and the Reynolds number is set to 10^5. The initial conditions are the ones given at the boundaries and zero velocity in the rest of the domain.

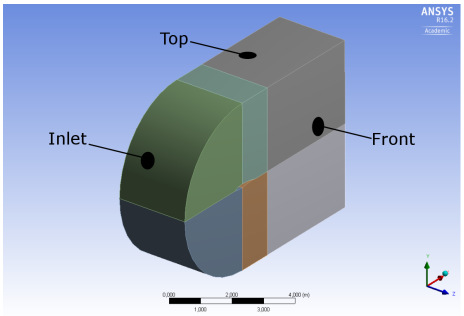

(a) Front of the domain

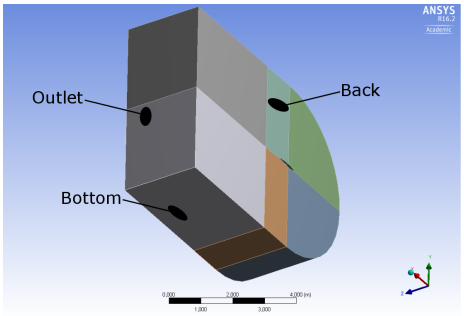

(b) Back of the domain

Figure 4.8: Front and back of the domain

Table 4.1: Boundary conditions

Face	Type of boundary
Inlet	Velocity inlet
Outlet	Pressure outlet
Airfoil	No-slip wall
Top, Bottom, Front and Back	Slip wall

Table 4.2: Flow parameters

Parameter	Value
Pressure	1 atm
Velocity	$1.470 \frac{m}{s}$
Density	$1.225 \frac{kg}{m^3}$
Dynamic viscosity	$1.802 \frac{kg}{m \cdot s]}$
Temperature	15°C
Turbulence intensity	0.44%
Turbulent length scale	$1m$

4.5 Time step study

When running a transient simulation it is important to run it long enough for two reasons. First of all the flow needs to fully develop over the whole domain, secondly the flow needs to be simulated long enough in the developed stage so that the simulated flow data can be averaged over a long enough time to accurately represent the characteristics of the flow. From Sarlak [18] we get that all the forces and pressures extracted from the flow should be averaged over approximately four non-dimensional time units (NTUs), defined as

$$NTU = \frac{c}{U_\infty} \tag{4.1}$$

where c is the cord length and U_∞ is the free flow velocity magnitude. The flow needs to be run for at least 5 NTUs to fully develop. In this study, there is only one inlet at the front of the domain. As the initial conditions are zero velocity everywhere except at the inlet, it is important to consider that the flow needs time to reach and develop across the whole domain. For the windtunnel replica domain in this study and for a Reynolds number of 10^5, this amounted to having the flow to run for at least 12 NTUs or a little over 7 seconds in real flow time for $U_\infty = 1.47\frac{m}{s}$ and $c = 1m$.

When determining the time step size, the Courant number needed to satisfy the Courant-Friedrichs-Lewy condition is used to decide the first time step. The Courant number for three dimensions is defined as:

$$C = \frac{u_x \Delta t}{\Delta x} + \frac{u_y \Delta t}{\Delta y} + \frac{u_z \Delta t}{\Delta z} \tag{4.2}$$

For an explicit solver the Courant number should not exceed one to ensure a converging solution. In this study an implicit solver is used and this kind of solver is often far less sensitive to large Courant numbers regarding stability. Still if the Courant number is pushed to higher values by increasing the time step size too much, it might result in a wrongly converging or even diverging solution. Different time step sizes are tested and driven to convergence to find a suitable time step size to be used further in the study.

4.5.1 Time step size

For the time step size investigation a grid based on the 2D simulation is used, taking the approximately same number of points over the airfoil and keeping approximately the same y^+ criteria. As the grid will be refined or the Reynolds number increased the time step size has to be changed according to the Courant number chosen, see equation 4.2. Unfortunately we do not have the capacity to conduct a full time step study on each of the grids tested in the grid dependency study, and where only run on the grid defined in Table**??**.

Table 4.3: Base grid for time step study. The edges are shown in Figure 4.7

Edge	Number of divisions	Bias factor
W	64	3000
NW	50	0
N	128	0
E	32	50
D	32	0

With this grid the time step required to reduce the Courant number to one is $10^{-3}s$. This time step size will be run at both 8192 and 16384 time steps, corresponding to approximately 12 and 24 NTUs, to be sure the flow has developed properly. Then the time step size will be increased and the number of time steps decreased and the results compared with the results of the $10^{-3}s$ time step. The most computationally efficient time step size, which also satisfies both accuracy and a reasonable Courant number will be chosen for the further studies.

The different time step sizes simulated with the different flow, times for each time step are tabulated in Table 4.4

The different time step sizes are simulated for different flow times, because they might converge for different flow times. Typically, the larger time step sizes will require longer flow time to fully converge. The time steps will be presented from the lowest to the highest. At the end of the section, a brief discussion on the time step sizes will

Table 4.4: Overview over the different time step size runs and for how many time steps they are run for.

Time step size (s)	0.001	0.0035	0.007	0.014	0.028	0.056	0.112
Time steps first run	8192	1024	512	256	128	64	32
Time steps second run	16384	2048	1024	512	256	128	64
Time steps third run		4096	2048	1024	512	256	128
Time steps fourth run		8192	4096	2048	1024	512	256

be made and a time step size will be chosen. The Courant number plots are shown in appendix A. In the following sections, the force coefficients and the computational time will be presented. The moment coefficient is defined around the z-axes from $\frac{1}{4}$ of the chord length and the CPU time is the time it takes to run the simulation on one of the cores described in appendix F.

Time step size = $0.001s$

The lift, drag and moment coefficients are tabulated in Table 4.5.

Table 4.5: Force coefficients for $\Delta t = 0.001s$.

Time steps	8192	16384
Lift coefficient	0.582809	0.583422
Drag coefficient	0.03242	0.032377
Moment coefficient	-0.28023	-0.28068
CFL_{Max}	1	1
CPU Time	452h 48m	895h 48m

As expected, the changes in running the flow twice as long are minimal. The force coefficients have converged and the Cp plots are almost identical. This means that this time step size represents a good comparison base for the larger time steps.

Time step size = 0.0035s

The lift, drag and moment coefficients are tabulated in Table 4.6.

Table 4.6: Force coefficients for $\Delta t = 0.0035s$.

Time steps	1024	2048	4096	8192
Lift coefficient	0.560	0.582	0.583	0.583
Drag coefficient	0.034	0.032	0.032	0.032
Moment coefficient	-0.264	-0.280	-0.281	-0.281
CFL_{Max}	3.5	3.5	3.5	3.5
CPU Time	53h 24	115h 24m	251h 24m	522h

From this, it is observed that the solution converges for around 2048 time steps or a little more than 7s, which coincides with the calculation made above.

Time step size = 0.007s

The lift, drag and moment coefficients are tabulated in Table 4.7.

Table 4.7: Force coefficients for $\Delta t = 0.007s$.

Time steps	512	1024	2048	4096
Lift coefficient	0.557855	0.581682	0.583456	0.583425
Drag coefficient	0.034112	0.03255	0.032382	0.032377
Moment coefficient	-0.26226	-0.27935	-0.28069	-0.28068
CFL_{Max}	7	7	7	7
CPU Time	27h 12m	54h 24m	114h	244h 12m

From this, it is observed that the solution converges for around 1024 time steps or a little more than 7s, which coincides with the calculation made above. Compared to the previous time step size, the same accuracy level can be reached while reducing the computational costs by over 50%.

Time step size = $0.014s$

The lift, drag and moment coefficients are tabulated in Table 4.8.

Table 4.8: Force coefficients for $\Delta t = 0.014s$.

Time steps	256	512	1024	2048
Lift coefficient	0.551504	0.582139	0.583793	0.583459
Drag coefficient	0.034778	0.032749	0.032409	0.032381
Moment coefficient	-0.25773	-0.27935	-0.28087	-0.2807
CFL_{Max}	16	14	14	14
CPU Time	14h	27h 24m	52h 12m	117h 24m

From this, it is observed that the solution converges for around 512 time steps or a little more than 7s, which coincides with the calculation made above. Compared to the previous time step size, the trend that when the time step is doubled the total time steps, and then the computational requirements, can be halved.

Time step size = $0.028s$

The lift, drag and moment coefficients are tabulated in Table 4.9.

Table 4.9: Force coefficients for $\Delta t = 0.028s$.

Time steps	128	256	512	1024
Lift coefficient	0.528301	0.584431	0.585871	0.583804
Drag coefficient	0.037791	0.033338	0.03252	0.032409
Moment coefficient	-0.23715	-0.27982	-0.28202	-0.28088
CFL_{Max}	45	32	27	27
CPU Time	7h 12m	13h 48m	28h 12m	52h 12m

From this, it is observed that the solution converges for around 512 time steps or a little more than 14s, which is double the flow time for the smaller time steps. Compared to the previous time steps sizes, the trend that when the time step is doubled the total time steps can be halved still continues, but it is observed through the drag coefficient

and CFL number that the flow is not fully developed at the usual 7s which here coincides with the 256 time steps. To be sure of convergence it needs to be run for 512 time steps, the same as with half the time step size.

Time step size = $0.056s$

The lift, drag and moment coefficients are tabulated in Table 4.10.

Table 4.10: Force coefficients for $\Delta t = 0.056s$.

Time steps	64	128	256	512
Lift coefficient	0.467688	0.557017	0.591428	0.585966
Drag coefficient	0.045922	0.036512	0.033043	0.032409
Moment coefficient	-0.23715	-0.27982	-0.28202	-0.28088
CFL_{Max}	180	100	70	55
CPU Time	4	7h 24m	14h 36m	28h 36m

From this it is observed that the solution converges for around 512 time steps or a little above 28s, which clearly continues the development that even when the time step size is doubled, the flow time needs to be double as well to be sure of convergence. Compared to the previous time steps, the Courant number is increasing a lot. If this time step is used that is an error to consider, and also a source of error that might have a bigger impact on different grids and different angles of attack.

Time step size = $0.112s$

The lift, drag and moment coefficients are tabulated in Table 4.11.

With such a large time step, which is not converged with the time steps used here it, becomes evident that no computational power can be saved on increasing the time step size more. Instead, the solution becomes more insecure as the Courant number rises rapidly. Needing close to a minute of flow time to converge it is way above the flow time it should need which is pointing towards a not very stable solution.

Table 4.11: Force coefficients for $\Delta t = 0.112s$.

Time steps	32	64	128	256
Lift coefficient	0.304743	0.467557	0.574175	0.589592
Drag coefficient	0.041239	0.046511	0.035692	0.033256
Moment coefficient	-0.08399	-0.17626	-0.26842	-0.28088
CFL_{Max}	400	350	180	130
CPU Time	1h 48m	3h 36m	6h	14h 12m

Concluding remarks

The main criteria for choosing a suitable time step is stability, accuracy and computational time. Even though the computational time is relatively small in all the time steps tested above, it is expected to rise exponentially when refining the grid and is an important criteria. It is a clear sign of stability if the solution converges around 7s, or 12 NTUs. The largest, and also then most computationally efficient, time step size to do this is 0.014 s with 512 time steps. This setup also satisfy the accuracy level by being almost identical to the smaller time steps. Looking at the computational time, it might be possible to marginally decrease it, and still keeping the same accuracy level, by choosing a larger time step size, but that comes with the cost of a higher Courant number and needing a longer flow time to converge and thus a more insecure and unstable solution. For the following studies the 0.014 s with 512 time steps is chosen as a base to ensure a stable, accurate and efficient solution. It is important to keep in mind that this time step changes inversely proportional to the Reynolds number in the final study and proportional to some of the grid refinements in the following grid dependence study.

4.6 Grid dependence study

For this particular study, the solution is very grid dependent. The grid is a deciding factor in when to use RANS or LES as well as being of huge importance on capturing the 3D effects in the flow. Unlike a RANS study, however the solution will not end up being grid independent. Instead, more and more cells will turn into LES and therefore, like in

an LES study, refining the mesh will converge towards the DNS solution. This will for obvious reasons need an extremely fine grid and an excessive amount of computational power. Therefore, when conducting the grid dependency study the change in solution is weighted against the increase in computational power.

Keeping all this in mind a more systematic approach to determine the right grid for our study was chosen. Instead of refining the whole grid in each refinement, each of the edges are refined independent of the other edges. Firstly, this makes it possible to see exactly what refinements that effects the solution to give a better understanding, secondly it makes it possible to not use excessive computational power on refinements not changing the solution. This is a more costly approach as the amount of simulations in the grid dependence study will multiply, but in this particular study it was judged to be worth it. The study is also run at an angle of attack of 8° to see if the refinements have a bigger impact on a case where there is expected to be more separation and turbulence.

The grid dependence study will be presented by going through all the different directions the grid was refined in, before a brief conclusion will be presented where a grid for the ensuing studies will be presented. While refining one edge all other edges will be kept at the same values as when investigating the time step size, seen in Table 4.3. The Cp-plots for all refinements will be presented in appendix **??**.

Depth

The refinement of the grid in the depth direction is believed to be the most important regarding capturing the 3D effects of the flow. Because of this a comparison of the x-wall shear stress is shown in Figure **??**. As the cells are much larger in the z-direction than the other directions, it is believed not to effect the choice of time step size and so a time step size of 0.014 is used with 512 time steps for all refinements.

The lift, drag and moment coefficients are tabulated in table 4.12.

From the pressure distribution, Figure C.2, we see little difference from the different refinements, while the forces is showing a definitive change for the two finer grids. This discrepancy is explained when investigating the x-wall shear stress. In Figure 4.9 the separation lines along the airfoil is shown. In the coarsest case, the flow looks com-

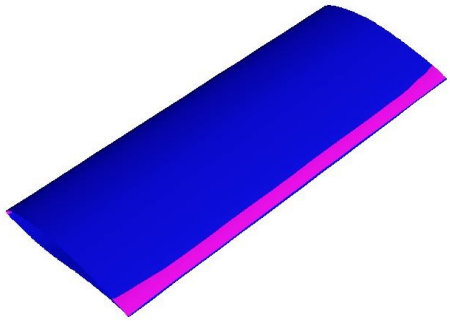

(a) 16 cells in the depth direction

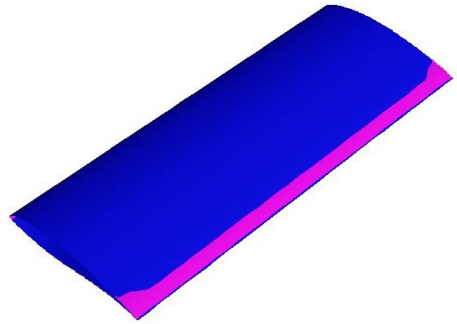

(b) 32 cells in the depth direction

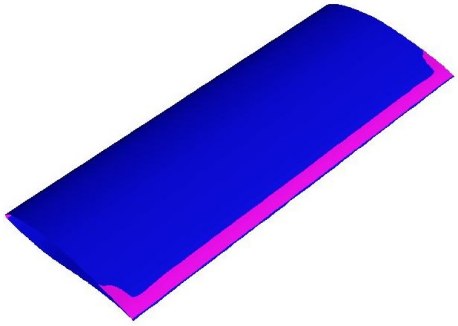

(c) 64 cells in the depth direction

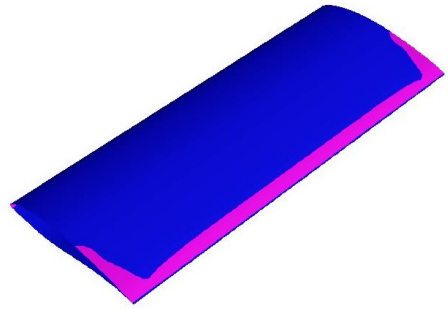

(d) 128 cells in the depth direction

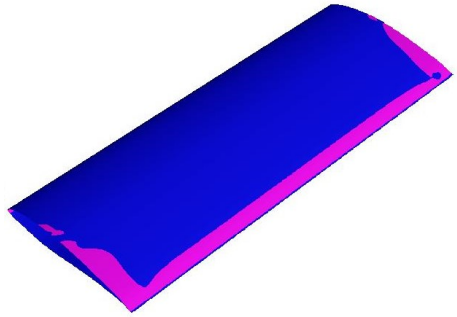

(e) 256 cells in the depth direction

Figure 4.9: X-wall shear stress over the top of the airfoil at $\alpha = 8$, $Re = 10^5$, with various numbers of cells in depth direction. Separation marked in pink

Table 4.12: Force coefficients and CPU-time for the different divisions on the Depth edge.

Division on the Depth edge	16	32	64	128	256
Lift coefficient	1.324502	1.322631	1.316795	1.292817	1.276933
Drag coefficient	0.068861	0.068705	0.068223	0.068576	0.073176
Moment coefficient	-0.83701	-0.83597	-0.83277	-0.81715	-0.80307
CPU-time	3h 48m	6h 36m	11h	24h 48m	110h 24m

pletely two-dimensional, for the grid with 32 points in the depth direction a little difference is shown towards the slip walls, but it still looks very two-dimensional. However, for the three finest grids the separation close to the walls are increasing steadily. This is not captured by the Cp-plot as this is extracted from the middle of the wing and most of the big changes in the z-velocities are occurring close to the slip walls. The force coefficients, however, are averaged over the whole wing and are therefore showing these changes. The change in the lift is less from 128 points to 256 than from 64 to 128 points, so it is believed that the change is decreasing. At the same time, the computational costs are rising very fast.

West

The amount of points placed on the west edge, or normal to the airfoil surface, is important to get a good enough resolution in the boundary layer as well as being a major deciding factor in when to use RANS or LES. In addition to the normal refinements, it is also run a case where the grid is extra fine and the bias factor is tuned down to 100. This gives much more similar sizes on all the cells outside the boundary layer, maybe improving the accuracy of the LES part of the DES. Since the cell size in the normal direction to the airfoil are the smallest in the grid, the time step size needs to be halved when the points are doubled to keep the same Courant number. To keep flow time the same the amount of time steps then needs to be doubled.

The lift, drag and moment coefficients are tabulated in table 4.13.

When refining the grid a small change in the forces can be observed, but refining

Table 4.13: Force coefficients and CPU-time for the different divisions on the West edge.

Divisions on the West edge	32	64	128	256 (100 in bias)
Lift coefficient	1.310609	1.322631	1.329466	1.315795
Drag coefficient	0.066368	0.068705	0.069881	0.068578
Moment coefficient	-0.83014	-0.83597	-0.83888	-0.83234
CPU-time	2h 48m	6h 36m	36h 36m	43h 48m

from 64 points to 128 points only gives a difference in the lift coefficient of under 0.5%, while almost six doubling the computational power needed. It is no indication that changing the bias will induce any better solution.

North and Northwest

These are the edges defining how many divisions there are around the airfoil, and they are divided into two different edges because of the choice of geometry and are changed simultaneously. Even though the spacing parallel to the airfoil surface is larger than the spacing parallel to the surface, the velocities also tends to be higher in this direction, so to be sure to keep an accurate and stable solution the time step is also here decreased proportionally when the number of points are increased.

The lift, drag and moment coefficients are tabulated in table 4.14.

Table 4.14: Force coefficients and CPU-time for the different divisions over the airfoil.

Divisions around the airfoil	114	228	456
Lift coefficient	1.32788	1.322631	1.31085
Drag coefficient	0.073756	0.068705	0.066306
Moment coefficient	-0.83664	-0.83597	-0.83058
CPU-time	4h 48m	6h 36m	12h 24m

In the finest grid there is a slight change in the lift and drag coefficients, while the computational costs double. The pressure coefficients are also on top of each other in the Cp-plot, viewed in Figure C.1.

East

The east edge decides the density of grid points in the wake of the airfoil starting a distance behind the trailing edge. These cell sizes are rather big so no changes are made with the time step when refining the grid. To keep the points over the airfoil constant, only the amount of divisions over the East edge was varied, see Figure 4.7

The lift, drag and moment coefficients are tabulated in table 4.15.

Table 4.15: Force coefficients and CPU-time for the refinements on the East edge.

Divisions on the East edge	16	32	64
Lift coefficient	1.325374	1.322631	1.320203
Drag coefficient	0.068908	0.068705	0.068556
Moment coefficient	-0.83749	-0.83597	-0.8346
CPU-time	5h	6h 36m	7h

When refining the grid in the tail region it results in minimal changes in all coefficients as well as in computational time.

Concluding remarks

Considering the amount of points in the span wise direction, it seems clear that a good resolution is very important to capture the 3D-effects of the flow. Even though the computational requirements increase with the increased resolution, it was deemed necessary to increase the accuracy of the results for the verification part of the study. In the normal direction it does not seems to be any noticeable change in accuracy compared to the rise in computational costs related to it after satisfying the y^+ criteria. The same is true for the amount of points around the airfoil. For the points in the tail, however, there seems to be no loss of flow characteristics or accuracy when reducing the amount of grid points. The limiting factor here is rather keeping the aspect ration to a reasonable number. Rooted in this the grid chosen to be run on the verification study is tabulated in Table 4.16

Table 4.16: Edge sizes of grid used in the verification study

Edge	Number of divisions	Bias factor
W	64	3000
NW	50	0
N	128	0
E	16	50
D	256	0

Chapter 5

Verification and Validation

For every CFD study the verification and validation parts are of paramount importance. **Verification** implies that the models are solved right, the grid is good and the solver works correctly. It is defined as:

"The process of determining that a model implementation accurately represents the developer's conceptual description of the model and the solution to the model." [4]

by the American Institute of Aeronautics and Astronautics(AIAA). A usual way to test this is by comparing results to a simple problem where an analytical solution is available. As ANSYS Fluent is a well tested code and is not believed to have any significant coding errors, this step is skipped and we only focus on comparing the solution with other specific numerical solutions, mainly from an LES study conducted at DTU [18]. The **validation** says how close the results obtained mirror the reality. It is defined as:

"The process of determining the degree to which a model is an accurate representation of the real world from the perspective of the intended uses of the model." [4]

by the AIAA. For flow around the NREL S826 airfoil at moderate Reynolds numbers, there are two main sources for experimental data to compare with; the experiments

conducted at DTU documented in Sarlak's PHD thesis [18] and the experiments conducted at NTNU documented in Aksnes master thesis [1]. Both of these will be used as validation bases. Lift and drag coefficients will together with the pressure distribution be compared with the simulated data at an angle of attack set to zero.

The grid used in this chapter for all simulations is the one tabulated in Table 4.16. As the Reynolds number will be 10^5 for all simulations in this chapter a time step size of $0.014s$ will be used and the simulations will be run for 512 time steps, corresponding to approximately 12 NTUs.

5.1 Verification

With the grid now chosen in the grid dependency study, see Table 4.16, numerous numerical settings will be tested to fine-tune the model we are running. These tests will also be run at an angle of attack of $\alpha = 8°$ and a Reynolds number of 10^5. For comparison the LES study conducted at DTU [18]. Accuracy and computational efficiency are the deciding factors when choosing which numerical settings will be used in the complete Reynolds number study. Except from the RANS model test, the Cp-plots were very similar and are therefore presented in appendix D.

This section will be divided into the different types of settings that can be changed, and comparing the different settings in each section. The different setting are tabulated in Table 5.1. Except from the different models, all other numerical settings are run on the Spalart Allmaras model as this is the most common and tested model in DDES.

Table 5.1: Different numerical settings within DDES in ANSYS Fluent. The acronyms and different settings are explained in chapter 2 or shown in abbreviations.

Model	**Pressure-Velocity Coupling**	**Gradient Discr.**	**Pressure Discr.**	**Convective Discr.**
SA	SIMPLE	Least Squares Cell Based	PRESTO!	Second order
Spalart Almaras, DES	PISO	Green-Gause Node Based	Second order	Third order MUSCL
Spalart Almaras CC				BCD
Realizable $k-\epsilon$				
SST $k-\omega$				
SST $k-\omega$, IDDES				

Models

The three base models in this study are Spalart Allmaras, realizable $k-\epsilon$ and SST $k-\omega$. In addition to these the curvature correction and strain/vorticity settings and the ordinary DES is tried with the Spalart Allmaras model as this is the most tested model, as well as the IDDES with the SST $k-\omega$ model because this is the only model possible to test this on.

The lift, drag and moment coefficients are tabulated in Table 5.2. Looking at the force coefficients there are two models that stand out. The $k-\epsilon$ model predicts a far higher lift than the others do, while the SST $k-\omega$ IDDES model predicts a lower lift. Looking further into the Cp-plots in Figure 5.1, it looks like the $k-\epsilon$ model is closest to the values from the LES study, while IDDES is for sure the one furthest away. Taking into consideration computational time it is clear that the SST $k-\omega$ models are the slowest to be computed. This is expected, as these are the most advanced models. $k-\epsilon$ is slightly faster than the SA options.

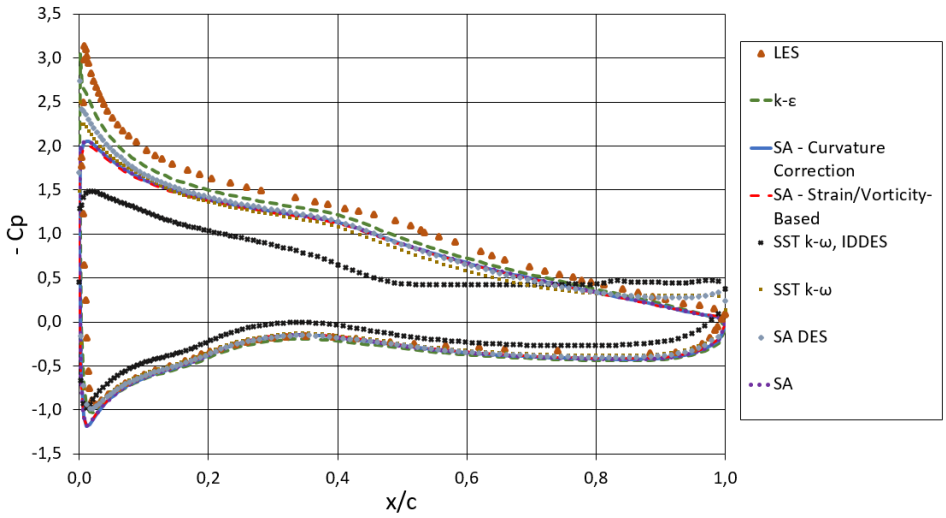

Figure 5.1: Various models compared to LES Cp results

Table 5.2: Force coefficients and CPU time for the different models. The acronyms and different settings are explained in chapter 2 or shown in abbreviations.

Model	SA	SA, S/V	SA, DES	SA, CC	$k-\epsilon$	SST $k-\omega$	SST $k-\omega$, IDDES
Lift coefficient	1.283332	1.252104	1.293993	1.283363	1.400599	1.234845	0.943652
Drag coefficient	0.068062	0.069803	0.052731	0.068059	0.050532	0.050081	0.072692
Moment coefficient	-0.81192	-0.78943	-0.8129	-0.81195	-0.88496	-0.78005	-0.57461
CPU-time	50h 48m	64h 12m	134h 36m	50h 12m	36h 24m	217h 24m	198h 12m

Pressure-Velocity coupling

For more information on the different schemes see section 3.2.6. In these tests, the PISO scheme diverged with the default relaxation factors, so the pressure relaxation factor was halved. The velocity relaxation factor was then changed according to the guideline where if the pressure relaxation factor = α, then the velocity factor should be = $1-\alpha$ [8].

The lift, drag and moment coefficients are tabulated in Table 5.3.

Table 5.3: Force coefficients and CPU time for the different pressure-velocity couplings.

Scheme	SIMPLE	PISO
Lift coefficient	1.283332	1.269317
Drag coefficient	0.068062	0.070797
Moment coefficient	-0.81192	-0.8027
CPU-time	50h 48m	220h 12m

The easiest parameter to look at here to see the differences is in the computational efficiency. SIMPLE is order of magnitudes faster than the alternative. In addition PISO shows some huge differences on the bottom of the wing, see Figure D.3.

Gradient Discretization

For more information on the different gradient discretizations see section 3.2.4 The lift, drag and moment coefficients are tabulated in Table 5.4.

Table 5.4: Force coefficients and CPU time for the different gradient discretizations.

Scheme	Green-Gauss Node Based	Least Squares Cell Based
Lift coefficient	1.283332	1.276587
Drag coefficient	0.068062	0.068543
Moment coefficient	-0.81192	-0.80785
CPU-time	50h 48m	49h

These two schemes are very similar to each other in coefficient values, while the Least Squares Cell Based method is the faster of the two.

Pressure Discretization

For more information on the different types of pressure discretization see section 3.2.5. The lift, drag and moment coefficients are tabulated in Table 5.5.

Table 5.5: Force coefficients and CPU time for the different pressure discretizations.

Scheme	Second Order	PRESTO!
Lift coefficient	1.283332	1.265186
Drag coefficient	0.068062	0.071467
Moment coefficient	-0.81192	-0.79639
CPU-time	50h 48m	180h 24m

Again, the main difference is in the efficiency of the calculation. The more advanced model does not bring with it an improvement in accuracy compared to the LES values when looking at Figure D.4

Convective Discretization

When applying DDES Fluent wants to run the momentum discretization on Bounded Central Differencing (BCD) [8]. The other convective discretizations will be changed as tabulated in Table 5.6. For more information on the different schemes see section 3.2.3.

Table 5.6: Force coefficients and CPU time for the different convective discretizations.

Scheme	Second Order Upwind	Third Order MUSCL	BCD
Lift coefficient	1.283332	1.277283	1.28626
Drag coefficient	0.068062	0.069196	0.068461
Moment coefficient	-0.81192	-0.82166	-0.81326
CPU-time	50h 48m	48h 48m	50h 36m

There is no reason for suggesting that any of these discretizations are more accurate than the other compared with LES, looking at the coefficients they are very similar and the Cp-plots, Figure D.1, are almost identical. Although the BCD and Second order

upwind are the most similar. Third order MUSCL is slightly faster than the two when looking at computational time.

Concluding remarks

The most important observation was that the $k-\epsilon$ model both yields pressure coefficients over the airfoil in best agreement with the experiment results and is the fastest to compute. It is usually not thought to be the most efficient and accurate RANS-model, but as it is the most widely used in industrial scale It might be so fine-tuned in ANSYS Fluent that it still turns out to be the best one in a relatively simple flow regime as the one investigated in this study. The schemes Least Squares Cell Based for gradient discretization and third order MUSCL for convective discretization, were faster with the traditional SA model than the default options. To see if this is also true for the realizable $k-\epsilon$ model another small study was conducted where the realizable $k-\epsilon$ model was tested with the different discretizations and compared concerning computational time and accuracy. The force coefficients with the different options are given in Table 5.7, and compared with the $k-\epsilon$ base case, where the schemes Green-Gauss Node Based and second order upwind are used.

Table 5.7: Force coefficients and CPU-time for the $k-\epsilon$ comparison study.

Scheme	$k-\epsilon$	$k-\epsilon$ with MUSCL	$k-\epsilon$ with Least Squares Cell Based
Lift coefficient	1.400599	1.406226	1.358697
Drag coefficient	0.050532	0.051044	0.053415
Moment coefficient	-0.88496	-0.88797	-0.85785
CPU-time	36h 24m	41h 24m	42h 36m

As is clearly shown by the CPU-time, what was applicable to the Spalart-Allmaras model is not necessarily the same for the $k-\epsilon$ model. The accuracy is the same, with the Least Squares Cell Based predicting a little lower lift, but judging by the CPU-time, the first option is the fastest. For the other settings the main criteria to separate them where looking at the CPU-time, as the accuracy in general was rather similar.

The settings that are chosen for the rest of the Reynolds number study is tabulated in Table 5.8

Table 5.8: The numerical settings decided to be used in further studies, and will now only be denoted as DDES or DDES $k-\epsilon$.

Model	Realizeble $k-\epsilon$
Pressure-Velocity Coupling	SIMPLE
Gradient Discretization	Green-Gauss Node Based
Pressure Discretization	Second Order
Moment Discretization	Bounded Central Differencing
Convective Discretization	Second Order Upwind

5.2 Validation

For validating the numerical setup in this study the simulated values are compared with the experimental results from wind tunnels at both DTU and NTNU, at angle of attack = 0° and Reynolds numbers of 10^5 and $2 \cdot 10^5$, respectively. For the NTNU study there will also be a comparison of the force coefficients at different Reynolds numbers. The conditions for the rest of the tests in this chapter are tabulated in Table 4.2. The results are discussed below.

NTNU

The force coefficients for angle of attack 0.5° and Reynolds number $2 \cdot 10^5$ are tabulated in Table 5.9

Table 5.9: Coefficient comparison with NTNU experimental values, at $\alpha = 0.5$ and Re $= 2 \cdot 10^5$

Coefficients	Experimental	DDES, AoA = 0.5°	DDES, AoA = 1°	DDES, AoA = 0°
Cl	0.7237	0.678148	0.733269464	0.634119
Cd	0.0308	0.023102	0.02408566	0.021589

Since the mechanical error margin on the angle of attack in the NTNU wind tunnel is 0.5% [1], and it is hard to quantify how big an impact this has on the solution, this table includes the simulation results for angle of attack 1° and 0° to give an impression on how large the error is when having an error margin of 0.5°. It is observed that the difference in the lift coefficient is close to 10%. As the difference between the simulated and experimental lift coefficient values for 0.5° are less than the difference between the 0.5° and 1° simulations, it is evident that the lift coefficient is clearly within the NTNU wind tunnel angle error margin. The drag coefficient is a little bit off, but as the values are so small the error of reading them off a chart, even with pixel accuracy, is rather big. To get a better understanding of the forces around the airfoil the pressure coefficient is plotted against the experimental values in Figure 5.2.

The big difference between the experimental and simulated values is that the pressure on the suction side of the airfoil is much lower for the experiment than the numerical values. There is a rather big improvement from the values obtained in the 2D study, but still not quite at the experimental values. There can be numerous explanation for this. The first is that the uncertainty of the angle set in the NTNU wind tunnel is 0.5° [1], as can be seen in the same graph from our own "uncertainty" analysis varying the angle of attack with 0.5° this can make a big difference, up to about almost 10% and can account for most of the difference from the simulated to the experimental values. In Figure 5.2 it is easy to visualize the error margin as it would be the area between $\alpha = 0$ and $\alpha = 1$ in the numerical solution. In addition after information from Jan Bartl (personal communication, 22. April, 2016), there are numerous other sources of uncertainty. Firstly, the surface pressure of the wing is measured with a Digital Temperature Compensation (DTC) pressure scanner. They are accurate and only have an uncertainty of ±0.05%, but the uncertainty may give rise to an estimated maximum of ±0.1% because of the duration and temperature dependency of the measurements. The velocity measurements also have some uncertainties connected with temperature, pressure and calibrating the measuring device. Totally this amounts to approximately ±0.55%. The incoming velocity field is also constantly between ±1% of the given velocity. With these errors added to the angle error it is decided that the numerical results from this study

are within the uncertainty area for most of the values over the wing, validated through the experimental results from NTNU and can be viewed upon to represent the physical reality to a good accuracy.

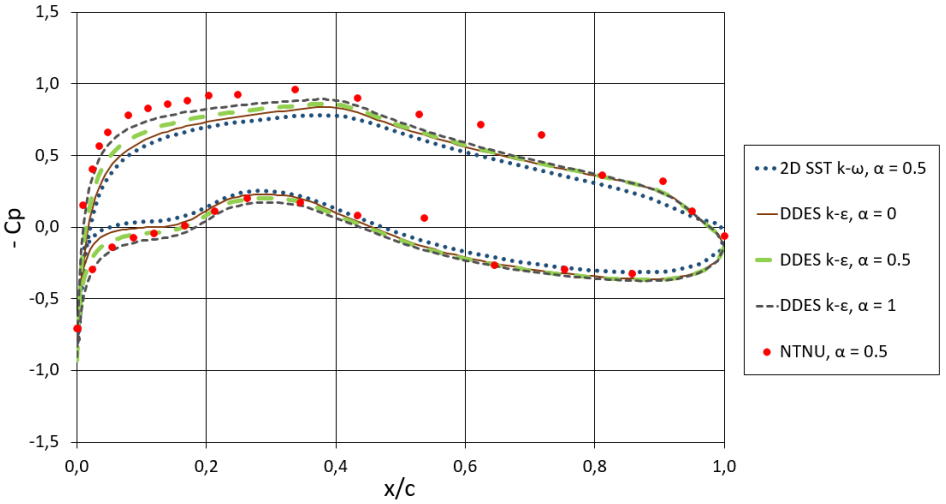

Figure 5.2: Cp distribution at Re = $2 \cdot 10^5$.

DTU

The force coefficients for angle of attack = 0° and Reynolds number 10^5 are tabulated in Table 5.10

Table 5.10: Coefficient comparison with DTU experimental values

Coefficients	Experimental	LES	DDES
Cl	0.5331	0.6244	0.6352
Cd	0.0308	0.0194	0.0254

From Table 5.10 it is observed that the experiment is getting higher drag than the two simulations. Still the drag is rather small, and the values obtained in this study lie between the experiment from DTU and the LES conducted at DTU. Lift from the experimental values is considerable lower than what both the numerical approaches

are showing. To try to explain this the Cp-plot is shown for the same conditions in Figure 5.3.

In this plot, it is evident that on the first half of the wing, both on the pressure and suction side, the simulated values agrees fairly well with the experiment. On the second half however, the results deviates quite a bit. While the simulated pressure goes up at the back of the airfoil as the velocity decrease, the experimental pressure from DTU stays low through the complete upper surface. This sort of pressure development is usually connected with separation. As the flow separates from the airfoil, momentum is lost, and the pressure on the airfoil surface is reduced. However, the simulations do not seem to capture any separation, something that might explain the deviating values. A possible separation at $x/c \approx 0.6$ in the experiment, but not in the LES, is also described by the DTU paper [18].

A more intricate subject is what is causing the gap between the experimental values and the simulations on the lower rear half of the airfoil. The first thing to consider is separation occurring on the lower side of the airfoil. As already mentioned this would induce a horizontal pressure development in the Cp-plot, but in the analysis conducted by Somers [25] this separation on the pressure side should arise at higher Reynolds numbers and different angles of attack than the ones DTU is dealing with in [18].

In the DTU paper [18] it is explained how the pressure on the lower rear of the airfoil is not actually measured, but extrapolated from the values surrounding it. If the values on the upper surface of the airfoil were measured at lower values because of the separation, it directly affects the calculated values at the lower surface. This might explain why the shapes of the pressure distributions from the experimental data and simulations are so different on the second half of the airfoil. A last option is that since pressure can communicate both up- and downstream the lower pressure on the upper surface of the airfoil can communicate down to the lower surface and lower the pressure here.

For the DTU experiment Sarlak [18] has given an uncertainty on the pressure readings of about 2%. This is enough to put all the Cp values, except the massive separation, within the error margin of the experiment from DTU.

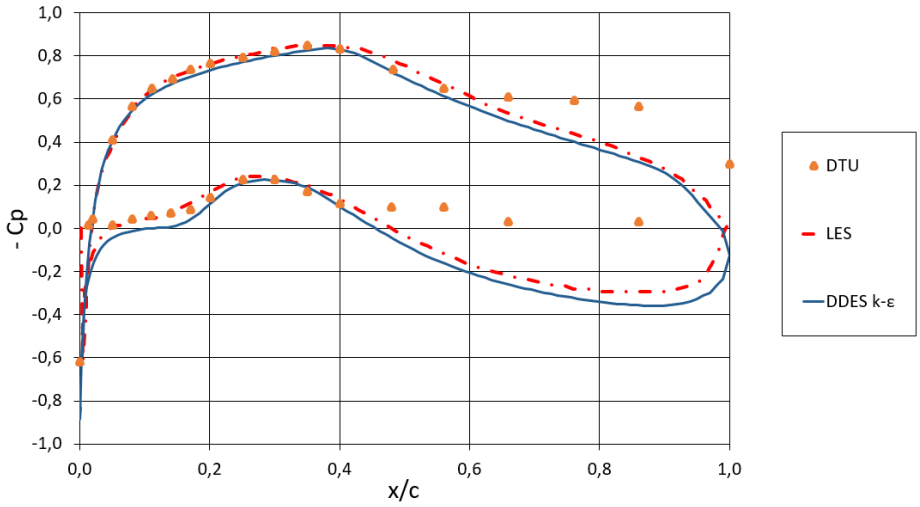

Figure 5.3: Cp distribution at $\alpha = 0°$ at Reynolds number 10^5, DTU and LES results taken from Sarlak [18]

5.2.1 Free flow approximation

A goal was also to see if the wind tunnel is a good approximation for the free flow it is actually made to represent. To test this in this study the domain was doubled in every direction, including spanwise direction, to see if it would affect the results. Even though this new domain is not big enough to be a free flow approximation in itself, if the change in results is small enough it might be enough to tell something about what would have happened if the domain was extended even more. The reason why the domain only was doubled was the computational limitations. To make sure that nothing else was affecting the results, all other conditions were kept the same except the grid which was doubled in the west, east and depth edge, defined in Figure 4.7. This was done to keep the resolution as similar as possible close to the wing, and in the depth direction to keep the same grid spacing. The free flow approximation test was run on angle of attack = 8° and a Reynolds number of 10^5. The rest of the conditions are tabulated in Table 4.2. The force coefficients are tabulated in Table 5.11, and the Cp-plot is given in Figure 5.4.

As can be seen from the Cp-plot the two geometries are almost inseparable over the whole wing. There is a slight difference in the force coefficients. These differences prob-

Table 5.11: Coefficient comparison between normal and double domain

Coefficient	Standard domain	Double domain
Cl	1.414806	1.435383
Cd	0.053489	0.049997

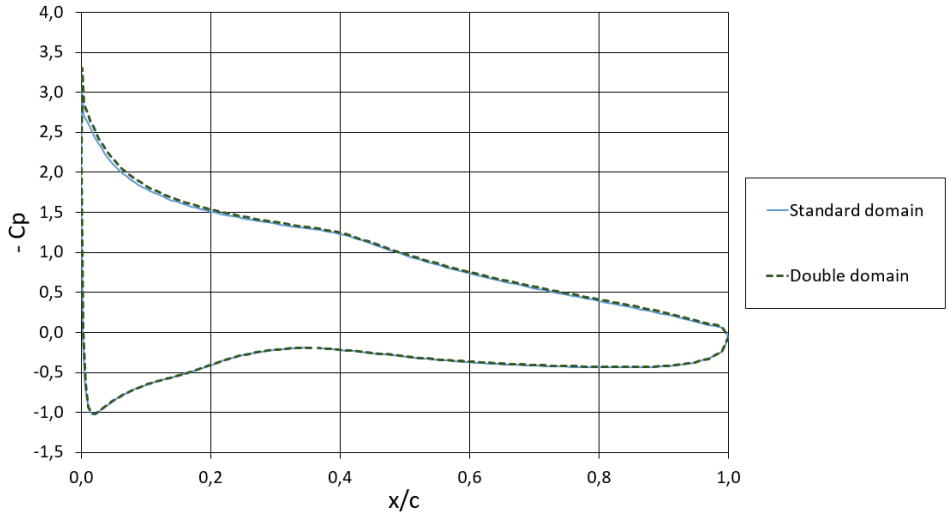

Figure 5.4: Double domain dimensions compared to standard domain at $Re = 10^5$, $\alpha = 8°$

ably originates from the fact that most of separation are centered around the slip walls. Comparing Figure 5.5 and 4.9 it is observed that the separation trends are the same for both geometries, it is just further between the slip walls where there is more separation. Extending the domain will therefore lead to a slight change in the coefficients that are averaged over the whole wing as the area of the wing grows larger. However, the coefficients change very little when doubling the domain. In addition the small area close to the walls are becoming smaller and smaller compared to the total area of the airfoil, illustrated in Figure 5.5. This change is expected to be less and less the more the domain is extended, because the separation area becomes smaller and smaller compared to the total area of the wing. Therefore, the force coefficients in the wind tunnel might be off by some percent compared to the free flow conditions, but the pressure coefficient over

the middle of the airfoil is very much closer to the free flow values.

Figure 5.5: x-wall shear stress over the top of the airfoil for double domain dimensions. Separation marked in pink

5.2.2 Concluding remarks

In this validation section, it has been found that the grid and numerical settings that have been decided in the previous sections and chapters definitely have some merit in explaining real physical phenomena. The numerical setup in this study seems to replicate the experimental data to a satisfactory degree. Especially for the results from NTNU, where the wind tunnel has been replicated by the geometry in this study, the values obtained in the simulations are satisfactory both in magnitude and development. In the DTU experiments they have an early separation. This might be caused by a lower turbulent intensity, which lead to a more laminar flow. This again might lead to sudden

changes in momentum in the boundary layer and cause adverse pressure gradients that lead too earlier separation.

Section 5.2.1 shows that the simulation, and therefore the NTNU wind tunnel, are good approximation to free flow conditions, although not perfect ones.

Chapter 6

Reynolds number study

In this study the flow over the NREL S826 airfoil will be tested for different angles of attack and different Reynolds numbers. The base of the different testing conditions will be those conducted experimentally in the NTNU windtunnel by Aksnes [1]. The different conditions with its associated turbulent intensities and different time step sizes are tabulated in Table 6.1. The rest of the flow parameters are as tabulated in Table 4.2, the grid used is tabulated in Table 4.16 and the numerical settings are tabulated in Table 5.8. All simulations are run for 512 time steps, corresponding to approximately 12 DTUs.

Table 6.1: Flow parameters

Reynolds Number	50 000	70 000	100 000	200 000	300 000	400 000	500 000	600 000	10^6
Velocity $[\frac{\mathbf{m}}{\mathbf{s}}]$	0.735	1.029	1.47	2.94	4.41	5.88	7.35	8.82	14.7
Turbulent Intensity (TI)	0.7	0.7	0.71	0.44	0.33	0.31	0.27	0.26	0.25
Time step [s]	0.028	0.020	0.014	0.007	0.00467	0.0035	0.0028	0.00233	0.0014

Table 6.2: Angles of attack

Angles of attack (AoA)	−12°	−10°	−8°	−6°	−4°	−2°	2°	4°	6°	8°	10°	12°	14°

The turbulent intensities (TIs) are mostly taken directly from the measured values by Aksnes [1]. But for the Reynolds numbers $5 \cdot 10^4$ and 10^6, they are approximated to the closest Reynolds number where the TI is given. This is as these numbers are not tested in the wind tunnel. All of these conditions are tested at the angles listed in the Table 6.2.

For a discussion on angle of attack 0° see section 5.2

6.1 Angles of attack

The choice of using whole angles instead of half angles contrary to what Aksnes did in his master's thesis is to better be able to compare the results with the LES and experimental results from DTU. Also this enables the comparison between the 2D results, which are also done on whole angles [16], DDES and LES, which is the main objective of this study. Aksnes results are still valid for comparison as the error margin on measuring the angle of the wing in the wind tunnel is 0.5°.

This study was a rather massive undertaking with the 14 different geometries and 9 different Reynolds numbers resulting in 126 simulations with an average of approximately 10 hours CPU-time. Therefore many of the Cp-plots and visualizations of the different test cases are shown in appendix E, but the plots referred to most are shown in the text. In this chapter some of the individual angles and their respective experimental counterparts will be presented first, then a comparison study with lift and drag curves over all the angles for all the Reynolds numbers will be presented.

6.1.1 AoA $= -6°$

The Reynolds number dependency and Cp-plots are shown in Figures 6.1 and 6.2 respectively.

At this angle, the flow is pushing the wing down creating a negative lift. Looking at the Reynolds number dependency the airfoil seems rather Reynolds number independent from $5 \cdot 10^4$ to $1 \cdot 10^6$, but still the lift is taking a small dip at the lowest Reynolds number.

Looking at the Cp-plots all of the Reynolds numbers predicts almost identical Cp curves, yielding Reynolds number independent results. Compared to the experimental and LES values from DTU the simulations in this study the big difference is the big separation occurring at about 0.1 chord length in the DTU experiment. The pressure on the rest of the airfoil is in fairly good agreement with the LES and experiment from DTU. Especially the bottom of the airfoil is in very good agreement. The experimental values from NTNU are in much better agreement with the results obtained in this study, not getting any separation at the front of the suction side.

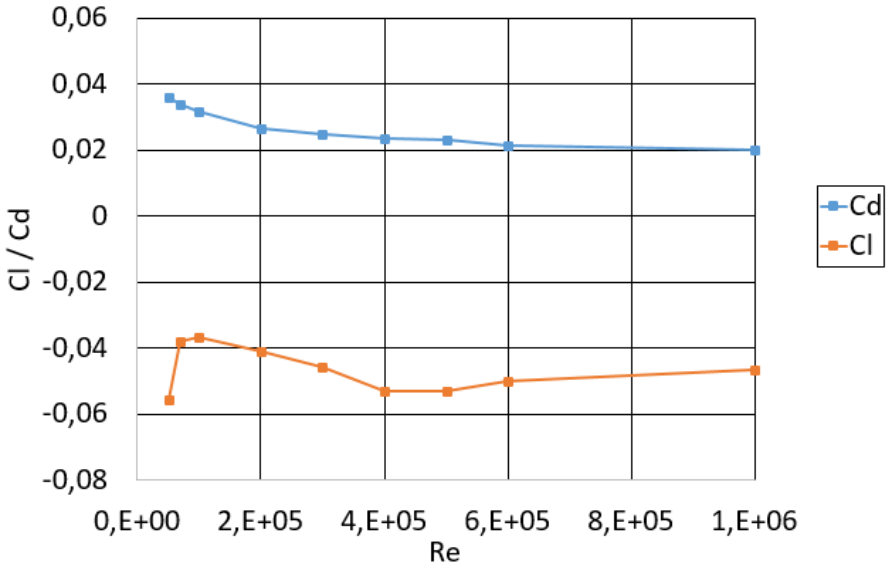

Figure 6.1: Reynolds number dependency at $\alpha = -6°$

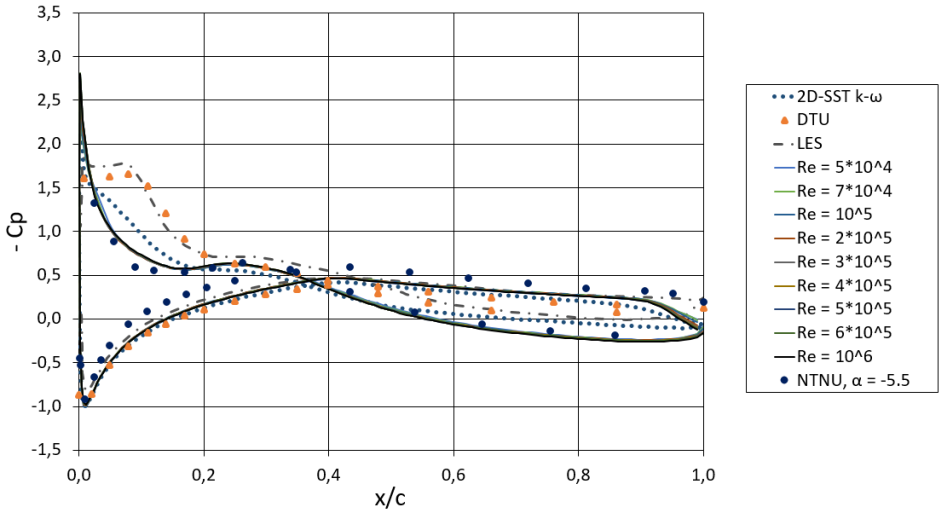

Figure 6.2: Cp distribution at $\alpha = -6°$

6.1.2 AoA $= -4°$

The Reynolds number dependency and Cp-plots are shown in Figures 6.3 and 6.4, respectively.

Even though the magnitude of the lift has changed, the exact same development as for the previous angle is observed. Both the lift and drag coefficients are Reynolds number independent for all the Reynolds numbers between $5 \cdot 10^4$ to 10^6, see Figure 6.3, though a slight decrease in lift and a slight increase in drag is observed for the lowest Reynolds number. This is also the first angle of attack creating a positive lift.

On the Cp-plot for AoA $= -4°$, in Figure 6.4 the first thing to notice is that it looks very Reynolds number independent for all the tested Reynolds numbers. Except for a slightly lower pressure some places on both the pressure and suction side of the airfoil, the different Cp-values from this study are inseparable. Both the LES and experimental values from DTU are also being followed by the values from this study extremely well, with the LES results being slightly closer to the DTU experiment on the pressure side, while the results from this study being slightly closer to the DTU experiments on the suction side. The DDES results are also a clear improvement of the 2D study at this angle. Looking at the experimental results from NTNU, they are following the same

development, but having a little lower pressure on the suction side and a little lower amplitude of low pressure close to the leading edge of the pressure side, this is presumably due to the half degree difference in higher attack angle.

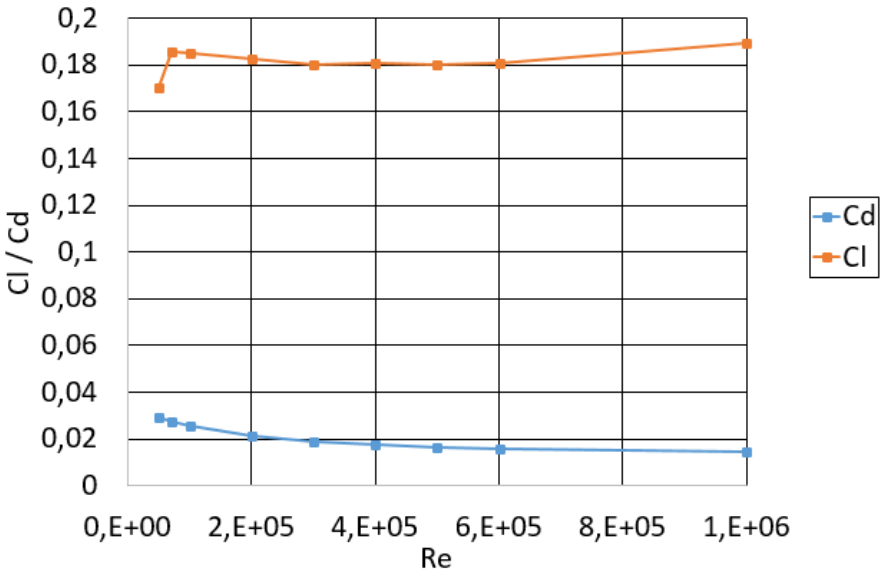

Figure 6.3: Reynolds number dependency at $\alpha = -4°$

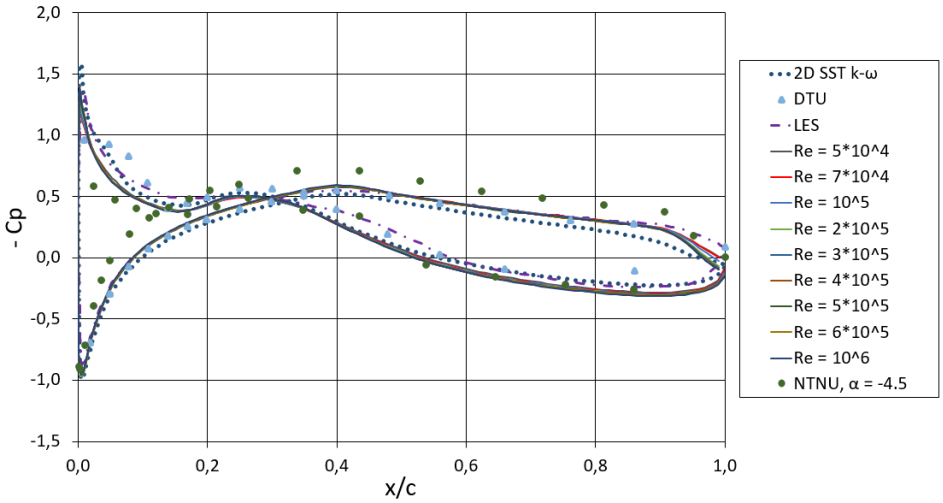

Figure 6.4: Cp distribution at $\alpha = -4°$

6.1.3 AoA $= -2°$

The Reynolds number dependency and Cp-plots are shown in Figures 6.5 and 6.6, respectively.

The lift is continuing the steady rise with the increasing angle of attack. The drag is behaving similarly to previous angles of attack both in magnitude and in Reynolds number dependency.

Compared to the LES results the values from this study matches them over the whole airfoil, except on what looks like a separation at about 0.5 chord length on the pressure side of the airfoil. The experimental values from DTU are having a massive separation on the back of the pressure side which is similar to what we have seen at AoA = 0°, which is discussed in the validation section in section 5.2. The NTNU results are having the same development of the Cp as the values obtained in this study, although having a lower pressure on the suction side, possibly due to the slightly higher angle of attack.

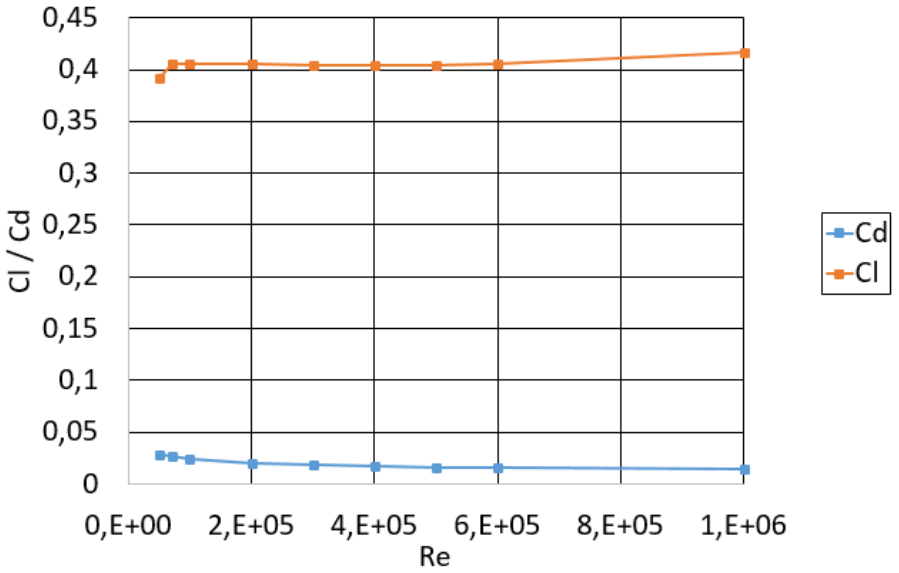

Figure 6.5: Reynolds number dependency at $\alpha = -2°$

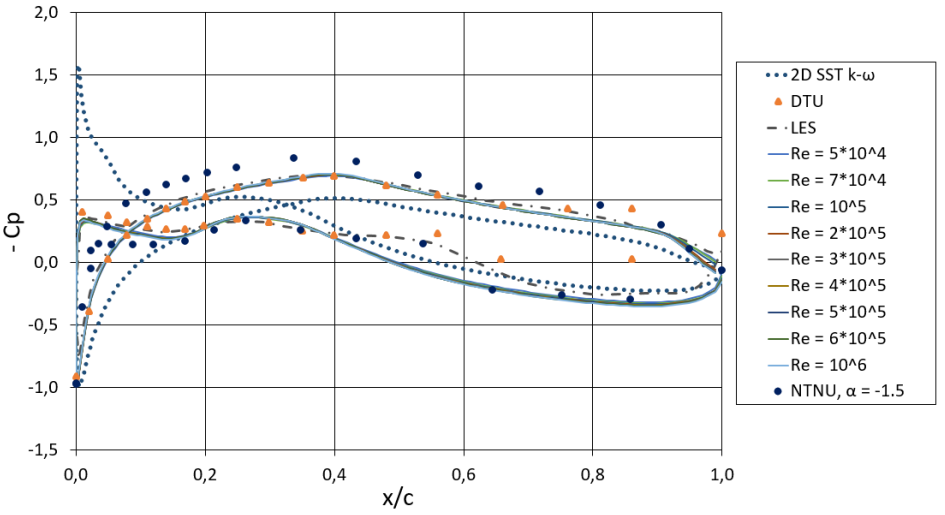

Figure 6.6: Cp distribution at $\alpha = -2°$

6.1.4 AoA = 2°

The Reynolds number dependency and Cp-plots are shown in Figures 6.7 and 6.8, respectively.

Looking at the Reynolds number dependency, the same trends as for previous angles of attack are seen. The lift is taking a small dip at the lowest Reynolds number, while the drag is staying more or less the same, see Figure 6.7.

The pressure distribution is very Reynolds number independent, while the remnants of the separation in the middle of the airfoil on the pressure side for the LES study is still present, along with the big separation in the experiment at the rear of the pressure side. It is observed that the values from this study are far closer to the LES results than the results from the earlier 2D study. For the experimental values from NTNU, they are again followed by the development of the numerical results, while producing a lower pressure on the suction side of the airfoil.

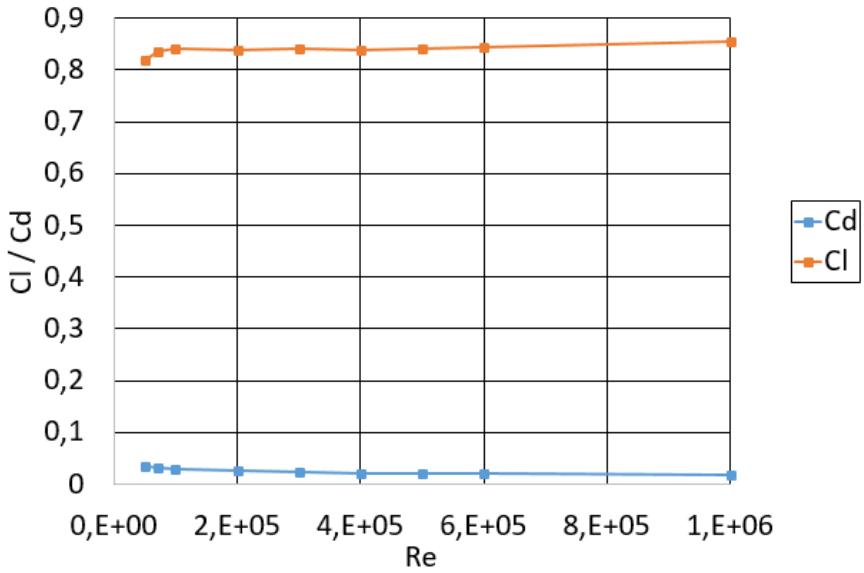

Figure 6.7: Reynolds number dependency at $\alpha = 2°$

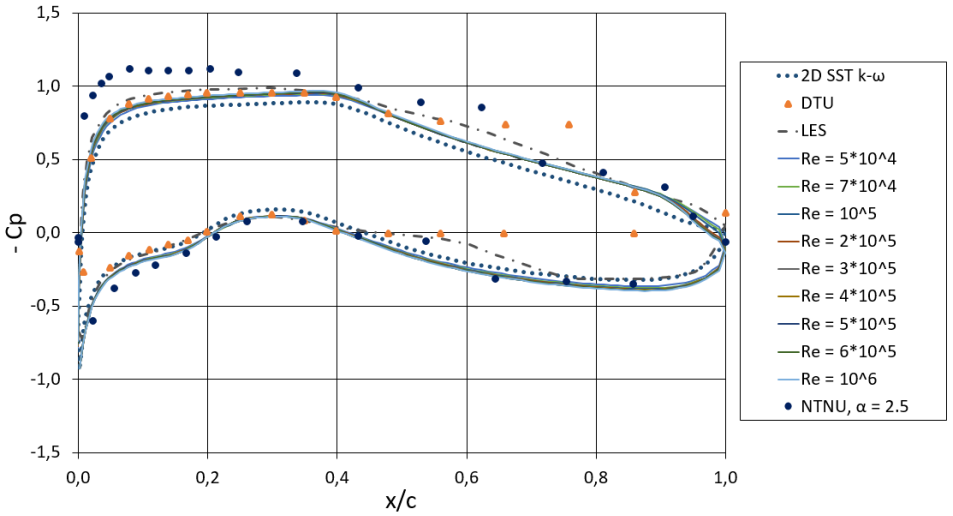

Figure 6.8: Cp distribution at $\alpha = 2°$

6.1.5 AoA = 4°

The Reynolds number dependency and Cp-plots are shown in Figures 6.9 and 6.10, respectively.

While the magnitude of the lift continues its linear rise, the magnitude of the drag continues to stay constant.

The Cp-plot is showing Reynolds number independence for all the Reynolds numbers, except for the lowest one. The results from the LES study are similar to the DDES results over almost the whole wing. On the first part of the suction side of the airfoil, the DDES results are closer to the experimental values than the LES, while on the rear the LES is slightly closer. The experimental values from DTU are still getting a separation at the suction side of the airfoil. The results from Aksnes are showing lower pressure on the front of the suction side, probably because the higher angle of attack is inducing higher velocities there. These results are, however, not showing any major signs of separation, even though having a higher angle of attack than the experiment conducted at DTU. Other than this the experimental and the numerical values from this study are in good agreement. There is also a distinctive improvement over the 2D results.

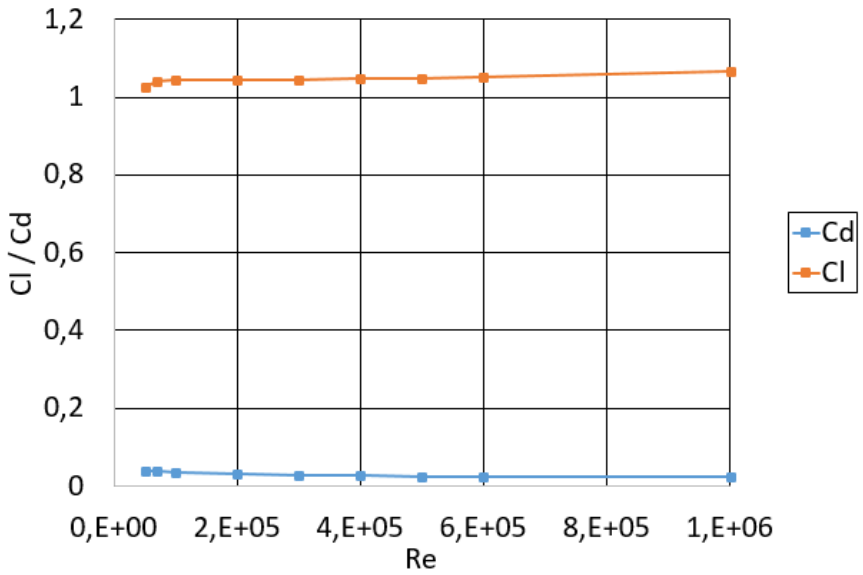

Figure 6.9: Reynolds number dependency at $\alpha = 4°$

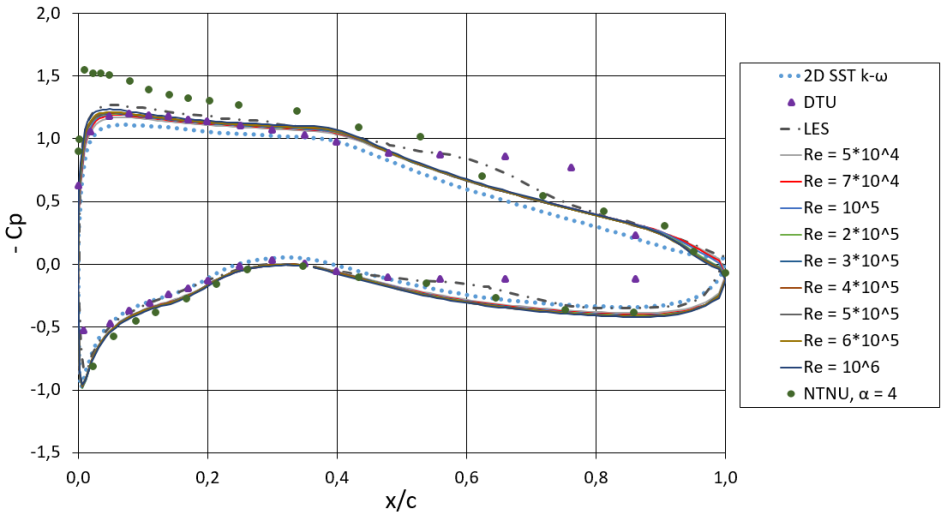

Figure 6.10: Cp distribution at $\alpha = 4°$

6.1.6 AoA = 6°

The Reynolds number dependency and Cp-plots are shown in Figures 6.11 and 6.12, respectively.

The same trend is continuing for the lift and drag coefficients.

The Cp-plot is very Reynolds number independent and the LES values and the results from this study agree almost completely for the values over the whole airfoil. The experimental values from DTU are also in much better agreement with the numerical results than for the angles around zero, as can bee seen in Figure 6.12. The only difference are the remnants of the separation on the middle of the suction side. The simulated values are also in very good agreement with the results from the NTNU windtunnel.

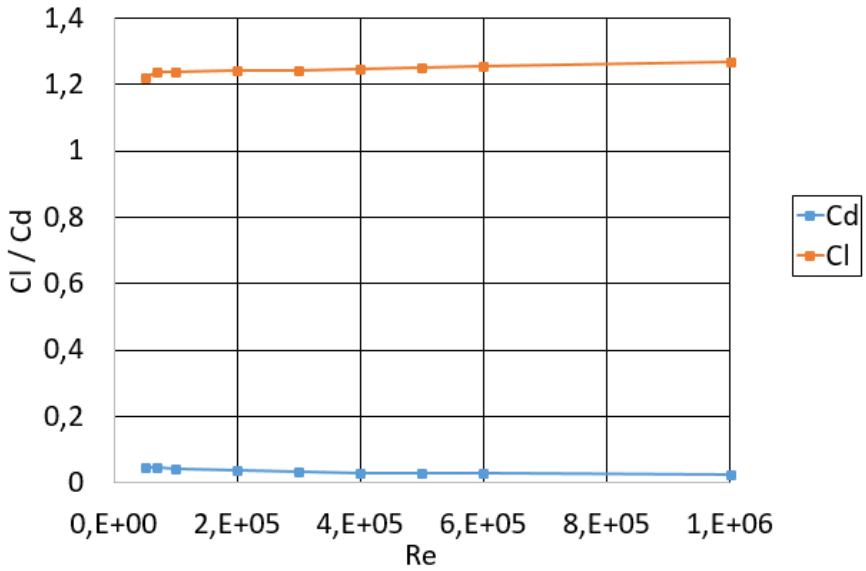

Figure 6.11: Reynolds number dependency at $\alpha = 6°$

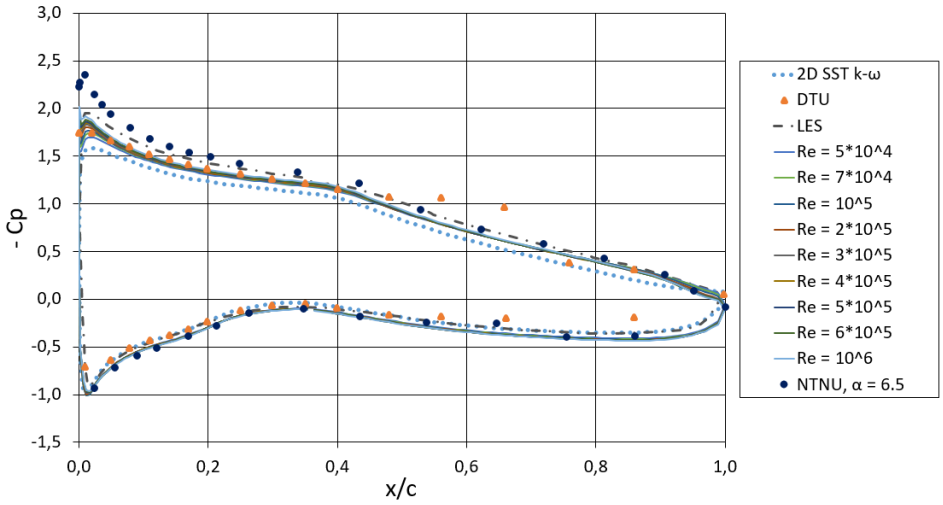

Figure 6.12: Cp distribution at $\alpha = 6°$

6.1.7 AoA = 8°

The Reynolds number dependency and Cp-plots are shown in Figures 6.13 and 6.14, respectively.

If anything, the force coefficients seem to be less Reynolds number dependent than for the smaller angles. It is also possible to spot the first signs that the lift is not rising as rapidly as for the previous steps between the angles. The drag is behaving as it has done for all the previous angles.

The results for this angle are Reynolds number independent for the pressure distribution everywhere, except for right at the leading edge of the suction side. For this particular angle of attack, the LES study is predicting too low pressure on the suction side, while the 2D simulations predict too high pressure compared to the experimental data. The results from this study, however, are producing Cp values that are in astonishingly good agreement with the experimental results from DTU as well as the NTNU data, see figure 6.14.

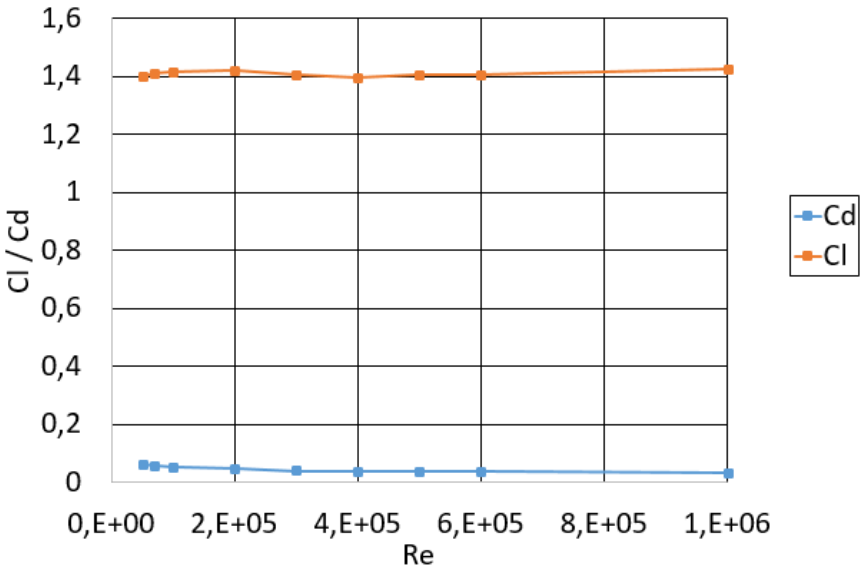

Figure 6.13: Reynolds number dependency at $\alpha = 8°$

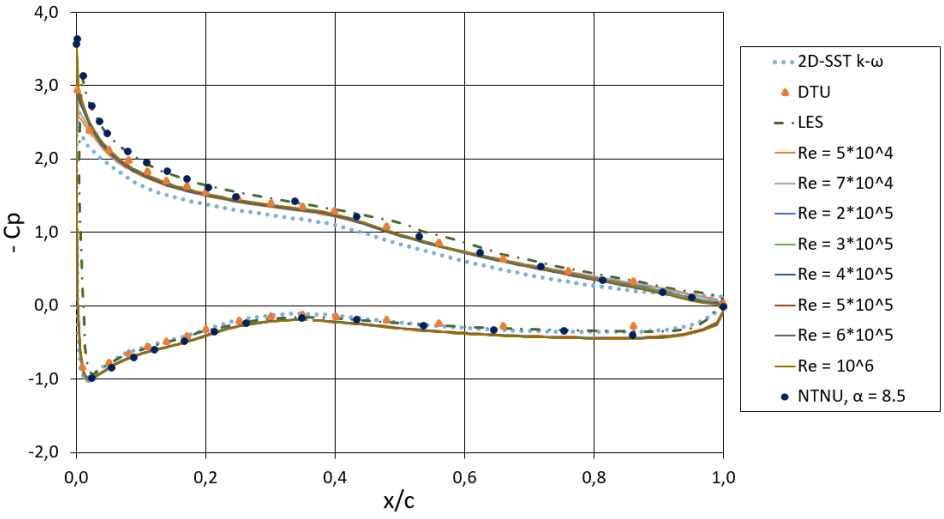

Figure 6.14: Cp distribution at $\alpha = 8°$

6.1.8 **AoA** = 10°

The Reynolds number dependency and Cp-plots are shown in Figures 6.15 and 6.16, respectively.

Both the lift and drag coefficients are looking very Reynolds number independent for $\alpha = 10°$. Contrary to the previous angles, the lift is actually slightly increasing towards the lower Reynolds numbers. Here it is also evident that the magnitude of the lift is starting to stay constant when increasing the angle of attack. This could be an indication that the stall angle is not much higher than 10°.

Considering the Reynolds number independence, the same applies here as for $\alpha = 8°$. Comparing it with the previous studies and experimental data it is observed that also here the DDES simulations from this study are closer to the experiment than the LES, which is getting a separation at the front half of the suction side of the airfoil. On the pressure side all of the results are in good agreement, as has been seen for most of the angles of attack. Comparing with the 2D results, the DDES simulation gives better agreement with the DTU experiment on the first and last part of the airfoil, while the 2D simulation performs better for the middle part. For the NTNU results, however, the DDES simulations yield better agreement than the 2D results over the whole wing, see Figure 6.16.

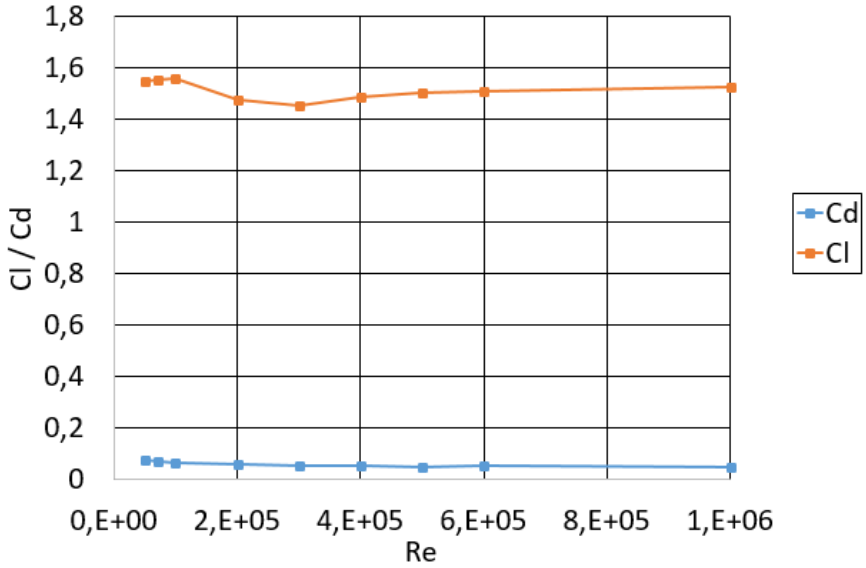

Figure 6.15: Reynolds number dependency at $\alpha = 10°$

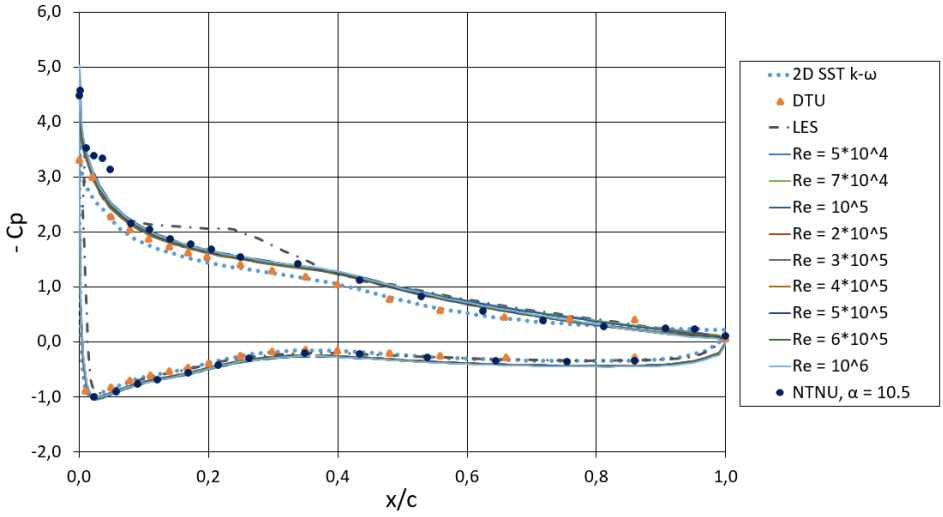

Figure 6.16: Cp distribution at $\alpha = 10°$

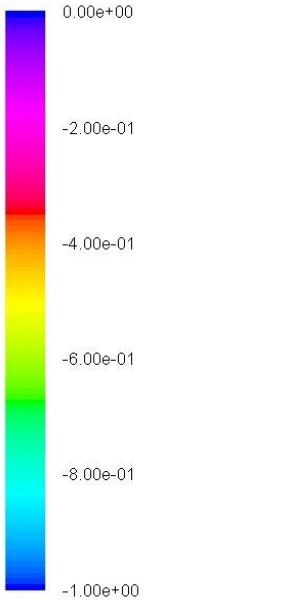

(a) x-wall shear stress range

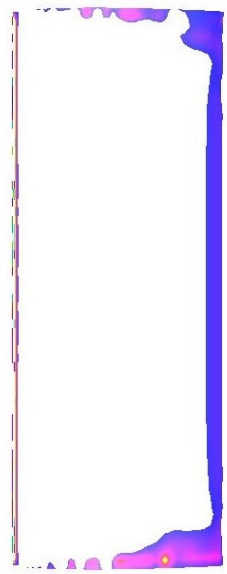

(b) $\alpha = 10$

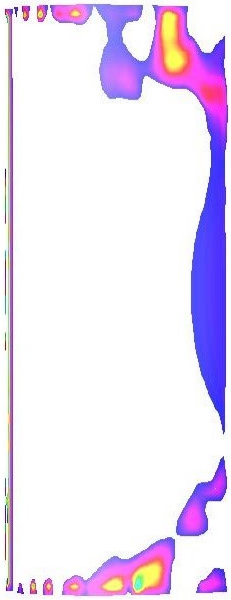

(c) $\alpha = 12$

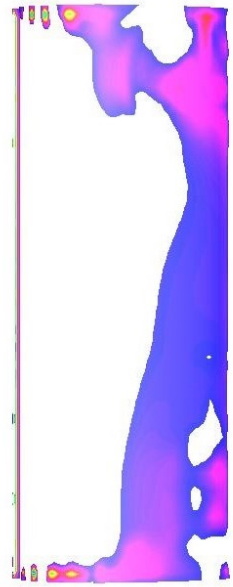

(d) $\alpha = 14$

Figure 6.17: x-wall shear stress at $Re = 10^6$ over the top of the wing. Leading edge and trailing edge at left and right respectively.

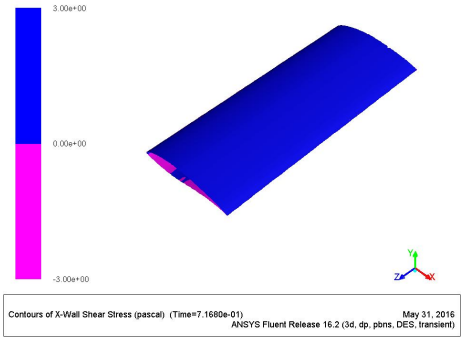

(a) $\alpha = -12$, top of the wing

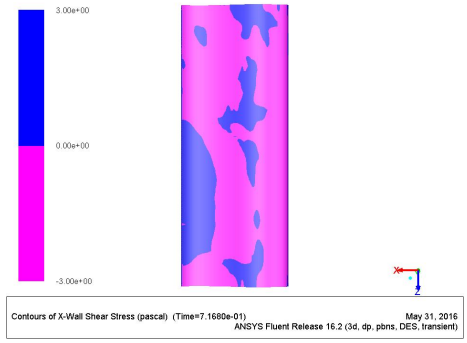

(b) $\alpha = -12$, under the wing

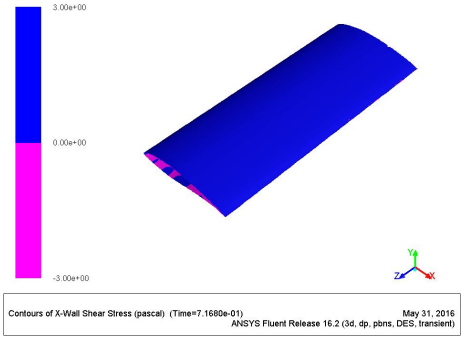

(c) $\alpha = -10$, top of the wing

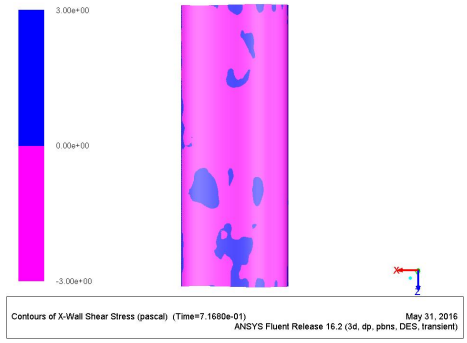

(d) $\alpha = -10$, under the wing

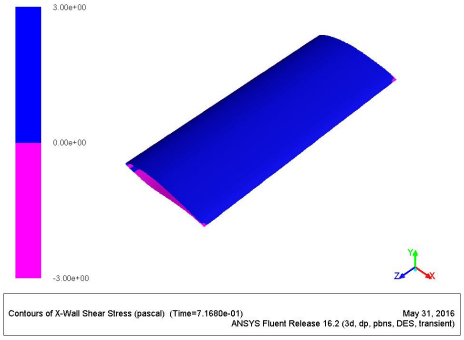

(e) $\alpha = -8$, top of the wing

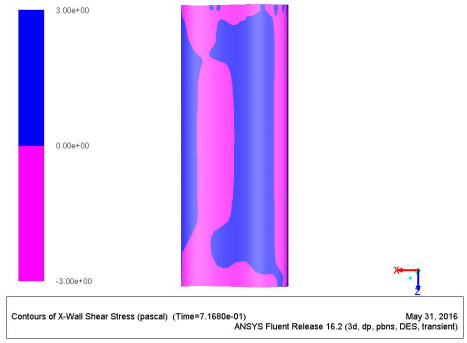

(f) $\alpha = -8$, under the wing

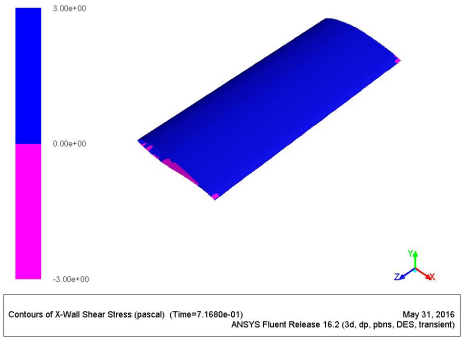

(g) $\alpha = -6$, top of the wing

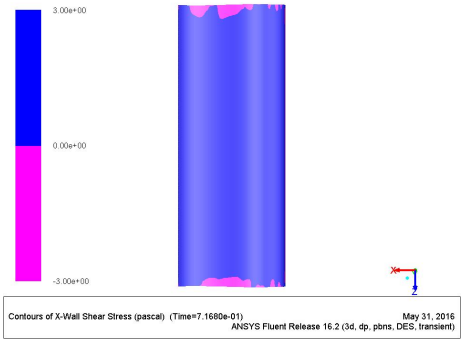

(h) $\alpha = -6$, under the wing

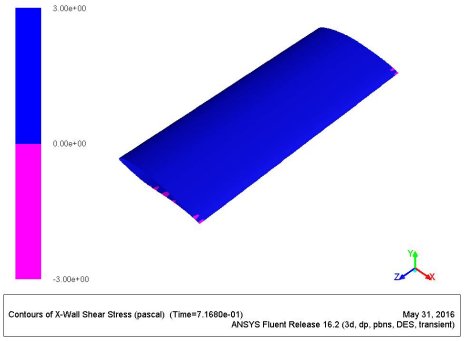

(i) $\alpha = -4$, top of the wing

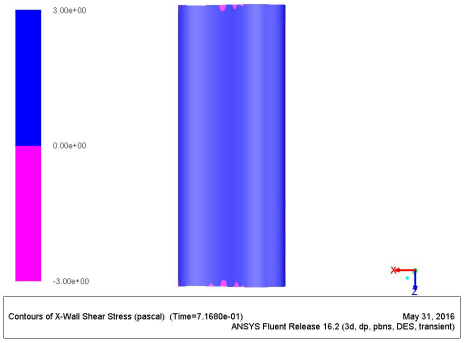

(j) $\alpha = -4$, under the wing

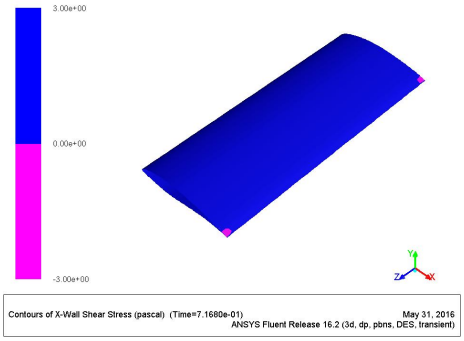

(k) $\alpha = -2$, top of the wing

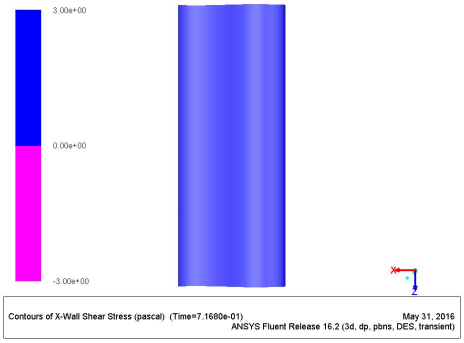

(l) $\alpha = -2$, under the wing

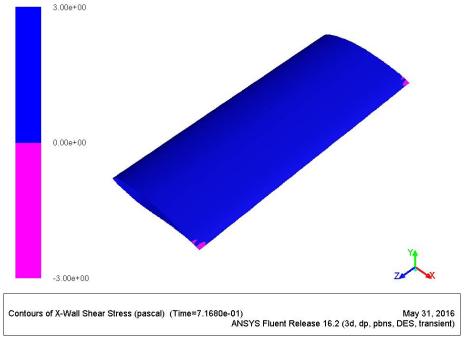

(m) $\alpha = 0$, top of the wing

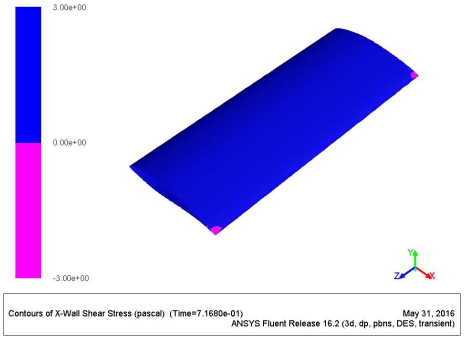

(n) $\alpha = 2$, top of the wing

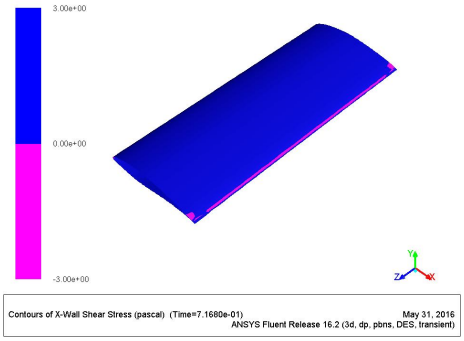

(o) $\alpha = 4$, top of the wing

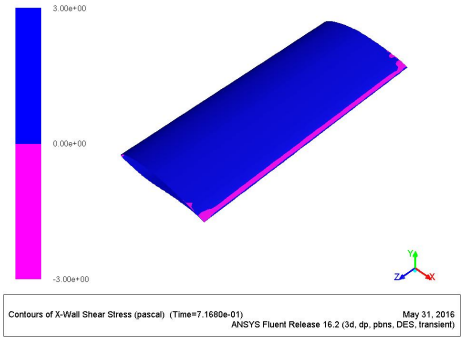

(p) $\alpha = 6$, top of the wing

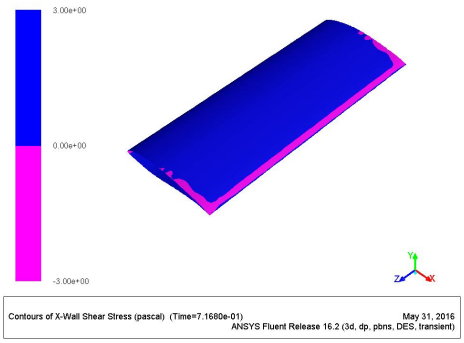

(q) $\alpha = 8$, top of the wing

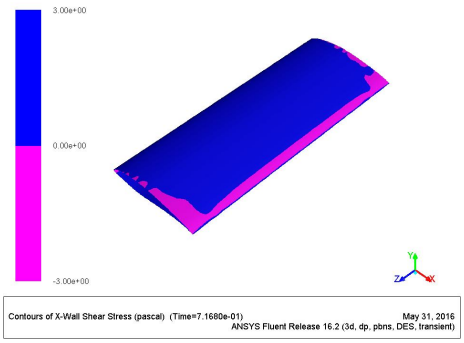

(r) $\alpha = 10$, top of the wing

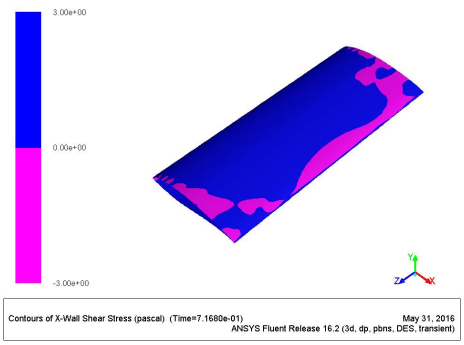

(s) $\alpha = 12$, top of the wing

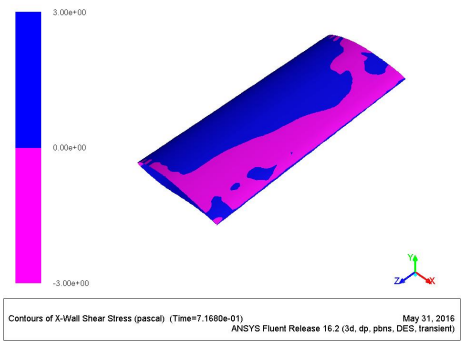

(t) $\alpha = 14$, top of the wing

Figure 6.18: Visualization of x-component of the wall shear stress for different angles of attack, $Re = 10^6$. Areas with separation is marked in pink (negative x-wall shear stress). Flow direction = +x

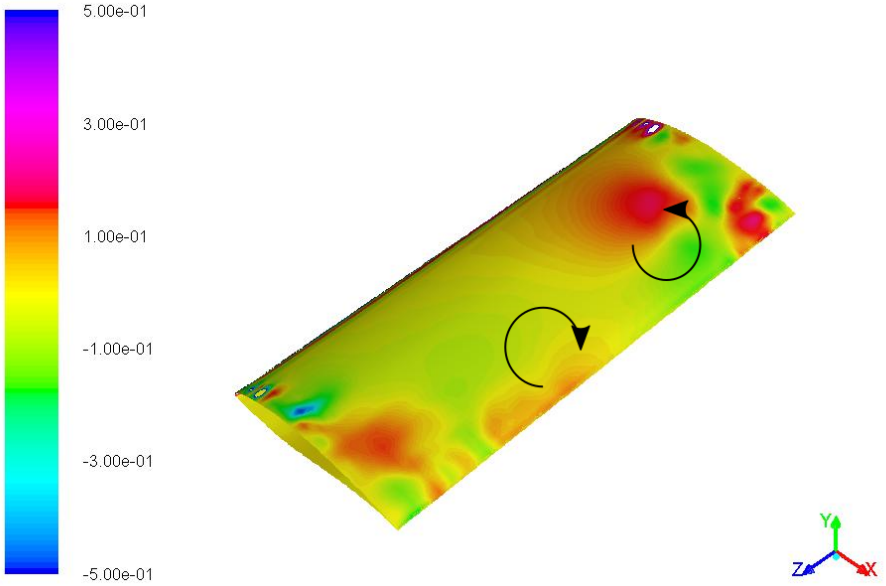

Figure 6.19: Wall shear stress in the z direction indicating stall cells over the suction side of the airfoil, marked with circular arrows. $\alpha = 14$, Re = 10^6. Flow in positive x-direction

6.2 Skin friction coefficient for higher angles of attack

For the three most negative angles of attack there is massive separation on the pressure side of the airfoil, see Figures 6.18a to 6.18f. This is expected as the curvature around the

leading edge is very high from these angles of attack. From $\alpha = -6$ to $\alpha = 8$ there is only small signs of separation either on the trailing edge or close to the slip walls, viewed in Figures 6.18g to 6.18q. Then more and more separation is developing over the suction side of the airfoil until there is a massive separation over much of the back half at $\alpha = 14$ 6.18t. The flow is not separating at the same place over the whole wing, but rather seems three dimensional and random. Looking at the shear stress in the z direction, Figure 6.19, a pair of counter rotating vortices is clearly visible over the suction side of the airfoil. These form what is called "stall cells" (SC). These are expected to appear around stall and shows that even a symmetrical setup in 3D , either experimental or simulated, will not produce a 2D flow. This is expected from previous studies [13].

6.3 Discussion

The pressure distribution gives a lot of data for an analysis. The lowest angle of attack, alpha = -6, is the one with the largest differences compared to experiment and LES from DTU [18]. The values in this study are agreeing well with the values from the NTNU experiment and not getting a separation on the front part of the suction side, which is the geometry that is actually replicated in this study. All the values are also agreeing to such an extended degree on the next angle of attack, AoA = -4, that it can be assumed that something, like lower turbulent intensity or different size of the windtunnel, is making it induce an early separation in the DTU experiments.

For the next angles of attack the same trends as the one discussed in the validation section in the previous chapter can be observed. The experiment from DTU gets a separation on the upper side of the airfoil. The LES study looks like it is capturing a small separation bubble on the pressure surface of the airfoil, following the experimental values slightly more than the DDES simulation in this study. This implies that the lower pressures on the pressure surface of the airfoil are due to a large separation bubble originating in the large curvature at around 0.4 of the chord length. Again here it can seem like some conditions around the DTU experiments are inducing separation more easily than in the NTNU experiments. The numerical DDES model results in this study are agreeing much better with the NTNU experiments than the 2D results from

the previous study in all cases.

The three higher angles, 6°, 8° and 10° (Figures 6.11, 6.13 and 6.15), have comparative little Reynolds number dependence. For all of these the simulated results agree with both experimental data from NTNU [1] and DTU [18]. For AoA = 6°, the remnant of the separation bubble in the DTU experiment is still visible around 0.6 of the chord length, and a noticeable difference is therefore present here. Looking at the two highest angles the simulated results follow the experimental results almost perfectly. For the higher angles of attack, the simulation results obtained in this study resemble the experimental data, both from DTU and NTNU, better than the LES study conducted at DTU. This can of course be affected by the fact that the verification process was run on AoA = 8°, and the numerical settings are fine tuned to match the LES results at this angle of attack. For the lower angles of attack it is harder to say which model yields the most accurate predictions. The reason why the DDES, a seemingly less accurate numerical model than the LES, can give as good or even better results might lie in the better representation of the wind tunnel using DDES. Since the grid requirements in the boundary layer were not that strict the whole domain of the wind was taken into account. However, in the LES study from DTU they had to create a thin slice with a spanwise depth of 0.5 chord length. Then a periodic approximation was made in the spanwise direction. But as our results show, there are more 3D effects close to the slip walls, and a periodic assumption might not be good enough. Even though the whole domain is built in this study, the whole grid ended up with 1 638 130 nodes in total, while the LES study had to have well over 10 000 000 cells [18]. In this regard, the DDES lived up to its expectations and was able to deliver an agreement with experiment totally comparable with LES, at a price comparable to RANS.

Comparing the results in this study with the previous 2D study it is clear that there are definitive 3D effects having an influence at all angles of attack and leads to a greater agreement with experiment when modelling the flow in 3D. This is confirmed when looking at the shear stresses, where especially at the higher angles attack around stall, the flow becomes clearly 3D.

6.4 Reynolds number study of lift and drag over angle of attack

In this section the lift and drag coefficients over angle of attack will be compared for different Reynolds numbers to see if the stall angle or any other part of the lift/drag curve is dependent on the Reynolds number. The results obtained in this study will also be compared to the results Aksnes [1] got in his master's thesis. In Figure 6.20 the LES study from DTU [18] is together with the 2D study and the results from the NTNU experiment compared with the DDES results with Reynolds numbers of $5 \cdot 10^4$, 10^5 and 10^6. The rest of the Reynolds numbers are plotted one by one in appendix E. Here, there are more angles added in both extremities than what was initially discussed for the individual angles.

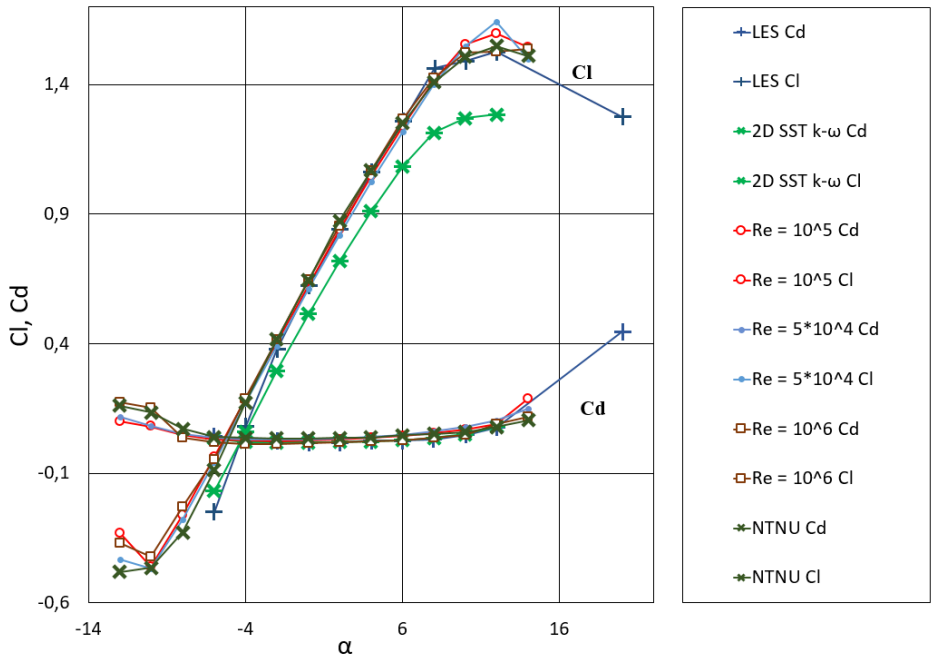

Figure 6.20: Cl and Cd variation over α. The Reynolds number for NTNU experiments and the LES and 2D studies are 10^5.

From Figure 6.20 it is observed that for the smaller angels of attack there is a clear

Reynolds independence, reflecting what was observed in the experiment at NTNU [1]. The lift and drag coefficients are slightly higher for the highest Reynolds numbers compared to the lower Reynolds numbers, but they are still rather similar. Also here it is evident that the DDES results are in far better agreement with the experimental data from NTNU than the 2D results which are predicting too low lift for most of the angles. Having the stall angle at approximately 12° is something most of the simulated and experimental values agree upon. An important observation is that the simulated DDES results from the highest angle are almost in perfect agreement with the experimental data from NTNU. This is an indication that the DDES is predicting the 3D effects after stall well and that the SCs are predicted in good agreement with experimental data.

The magnitude of the lift at angle of attack = 12° is not that similar. A trend towards being more Reynolds number dependent is observed at the highest angles. The reason for this might be the big separations taking place at these angles. These separations might lead to confusion in the DDES model if it is supposed to be running LES or RANS models, and they might be mixed and increase the inaccuracy of the solution. The Reynolds number dependency might be affected as the DDES might detect different areas as within the boundary layer with so much separation when considering different velocities. The results obtained for the high angles of attack could be a motivation for further studies with the DDES model in the stall and/or post-stall region. It is also interesting to see that for these high angles the 2D simulations are giving results in least agreement with the experimental data from NTNU. This difference is believed to be derived at least partly from the already mentioned SCs forming at these angles which is not possible to capture with a 2D simulation.

Looking at the most negative angles the lift and drag is rather constant and even starting to rise when decreasing the angle below −10°, see Figure 6.20. It is promising to see this trend also occurring in the experimental values as it proves that the DDES model can operate on angles with high pressure gradients and a lot of separation. A thing to notice here is that for these angles is that the drag is becoming more Reynolds number dependent. This might be explained in the same way as the lift for the higher angles as the pressure will have a bigger impact on the magnitude of the drag.

Chapter 7

Conclusions

7.1 Concluding remarks

In the literature study it was found that the new standard for DES study was the Delayed DES (DDES), which is better at using the RANS throughout the boundary layer and therefore less sensitive to changes in the grid than the original DES. Therefore, almost all of the simulations run in this study were using DDES.

The first investigation was a time step size study where a criterion for the time step size was found leading to efficient and accurate DDES simulations. For a Reynolds number of 10^5 that amounted to a $CFL_{max} \approx 14$. For the same Reynolds number it was found that the flow converged after approximately 512 time steps or a flow time a little above 12 NTUs.

In the grid dependency study it was as expected found that the solution did not become grid independent for any grid we had the capacity to test. The largest change occurred when the 3D effects significantly increased when refining the grid in the spanwise direction. Consequently when testing the different numerical models and settings, a grid with 256 divisions in the spanwise direction was used to be sure to get accurate enough results. This was computationally very costly. When moving on to the full Reynolds number study, a grid with 64 spanwise points was used, to give a good representation of the 3D effects and at the same time having manageable computational

costs. The rest of the grid, that was not found to need any major improvement from a 2D RANS grid, was chosen to 64 points in the normal direction, 228 points over the airfoil and 80 points in the tail direction.

The numerical tests led to some unexpected results. The first surprise was that the realizable $k-\epsilon$ model was the most accurate RANS model of the available options in the DDES model when verifying against the LES study conducted at DTU, and the least demanding when considering computational costs. The second surprise was that almost all the settings within a model gave the same level of accuracy, only differing in the computational costs.

After choosing the most accurate numerical model, based on the efficiency and accuracy compared with an LES study at DTU, a study on the most efficient numerical setup and a validation study was conducted. It was found that the numerical results were in close agreement with the experimental results from NTNU. The distribution of the pressure coefficient was very similar. Taking into consideration the different uncertainties concerning mechanical settings and measurements from the wind tunnels, the magnitude of the coefficients are within the uncertainty area. For the DTU experiment the difference is slightly larger, but for most of the airfoil the simulations in this study seems to represent the experimental pressure distribution well. The good agreement with the NTNU measurements are expected, as the geometry is built based on the NTNU wind tunnel and run under conditions representing the experimental conditions at NTNU. Seeing little difference in the results between the double and standard domain, it was also found that the wind tunnel is a good, within a few percent of the magnitude of the coefficients, representation of free flow.

The full Reynolds number study provided many cases for comparison with the NTNU measurements where the DDES performed well in almost all of them. Throughout the study the DDES model is outperforming the previous 2D RANS study when looking at the agreement with the experimental results for pressure distribution. The DDES results are also comparable to the LES study for most of the angles of attack, for some angles of attack the DDES results are closer to the experimental values than the LES values. This might be because the lighter grid refinement criteria free some computa-

tional power that can be used on constructing a larger and more accurate geometry. At the angles of attack around stall there started to be a trend for the results to be more Reynolds dependent. This might be because DDES finds it hard to predict when it is actually in the boundary layer and when it is not. It is also noted that the DDES correctly predicts a complicated 3D phenomenon like stall cells around the stall angles of attack, and shows that a 2D flow cannot be expected, even in a symmetrical 3D domain.

There might have been some losses in the accuracy when defining the walls as slip-walls and not considering the boundary layer at these walls. In addition, some flow characteristics are lost when not using the finest grid in the spanwise direction. Although these errors are believed to be small when the results are coinciding so well with the NTNU and DTU experimental results in addition to the LES study.

Overall the the DDES lived up to its expectations and was able to deliver results very comparable with LES, at a price comparable to RANS. The main goal of the study was to find out if DDES is a useful model to simulate turbulent airfoil flow at moderate Reynold numbers. Based on the results it can be concluded that DDES definitely is.

7.2 Further studies

Some possibilities regarding further studies based on this study are:

- Study in details how the DDES model behaves in stall and/or in post-stall regions with significant separation, turbulence and formation of stall cells.
- A DDES study focusing on replicating the DTU wind tunnel geometry and conditions to see if the experimental results from DTU around the smaller angles of attack can be replicated.
- Take the wind tunnel boundary layer into account by changing the location of the slip walls by the displacement thickness predicted by boundary layer theory.

Bibliography

[1] Aksnes, N. Y., 2015. Performance charecteristics of the NREL S826 airfoil.

[2] Bardina, J. E., Huang, P. G., Coakley, T. J., 1997. Turbulence modeling validation. AIAA paper 2121, 1997.

[3] Bertin, J. J., 1994. Aerodynamics for Engineers, 4th ed. Prentice Hall.

[4] Committee, A. S., et al., 1998. Aiaa guide for the verification and validation of computational fluid dynamics simuations (g-077-1998).

[5] Deck, S., 2005. Zonal-detached-eddy simulation of the flow around a high-lift configuration. AIAA Journal 43 (11), 2372–2384.

[6] Eppler, R., 1990. Airfoil design and data. Springer Science & Business Media.

[7] Fluent, A., 15. Theory guide, 2014.

[8] Fluent, A., 15. User's guide, 2014.

[9] Hamba, F., 2009. Log-layer mismatch and commutation error in hybrid RANS/LES simulation of channel flow. International Journal of Heat and Fluid Flow 30 (1), 20–31.

[10] Hu, H., Yang, Z., 2008. An experimental study of the laminar flow separation on a low-reynolds-number airfoil. Journal of Fluids Engineering 130 (5), 051101.

[11] Laboratory, N. R. E., 2000. Wind turbine airfoils, https://wind.nrel.gov/airfoils/.

[12] Lissaman, P. B. S., 1983. Low-Reynolds-number airfoils. Annual Review of Fluid Mechanics 15 (1), 223–239.

[13] Manolesos, M., Papadakis, G., Voutsinas, S., 2014. An experimental and numerical investigation on the formation of stall-cells on airfoils. In: Journal of Physics: Conference Series. Vol. 555. IOP Publishing, p. 012068.

[14] Nicoud, F., Ducros, F., 1999. Subgrid-scale stress modelling based on the square of the velocity gradient tensor. Flow, turbulence and Combustion 62 (3), 183–200.

[15] Pope, S. B., 2001. Turbulent flows. Measurement Science and Technology 12 (11).

[16] Prytz, E. R., 2015. Numerical of flow over the nrel s826 airfoil at moderate reynolds numbers, project Thesis, Norwegian University of Science and Technology.

[17] Rhie, C. M., Chow, W. L., 1983. Numerical study of the turbulent flow past an airfoil with trailing edge separation. AIAA Journal 21 (11), 1525–1532.

[18] Sarlak, H. C., 2014. Large eddy simulation of turbulent flows in wind energy. Uddannelse 2011.

[19] Schlichting, H., Gersten, K., 1999. Boundary layer teory, 8th ed. Springer.

[20] Schlichting, H., Gersten, K., 2003. Boundary-layer theory. Springer Science & Business Media.

[21] Schreck, S. J., Sørensen, N. N., Robinson, M. C., 2007. Aerodynamic structures and processes in rotationally augmented flow fields. Wind Energy 10 (2), 159–178.

[22] Shur, M., Spalart, P. R., Strelets, M., Travin, A., 1999. Detached-eddy simulation of an airfoil at high angle of attack. 4th International Symposium on Engineering Turbulence Modeling and Experiments 4 (January), 669–678.

[23] Shur, M. L., Spalart, P. R., Strelets, M. K., Travin, A. K., 2008. A hybrid RANS-LES approach with delayed-DES and wall-modelled LES capabilities. International Journal of Heat and Fluid Flow 29 (6), 1638–1649.

[24] Shur, M. L., Strelets, M. K., Travin, A. K., Spalart, P. R., 2000. Turbulence modeling in rotating and curved channels: assessing the spalart-shur correction. AIAA journal 38 (5), 784–792.

[25] Somers, D., 2005. The S825 and S826 Airfoils. National Renewable Energy Laboratory (January), 1994–1995.

[26] Spalart, P., Shur, M., 1997. On the sensitization of turbulence models to rotation and curvature. Aerospace Science and Technology 1 (5), 297–302.

[27] Spalart, P. R., 2009. Detached-Eddy Simulation. Annual Review of Fluid Mechanics 41 (1), 181–202.

[28] Spalart, P. R., Allmaras, S. R., 1992. A one equation turbulence model for aerodinamic flows. AIAA journal 94.

[29] Spalart, P. R., Deck, S., Shur, M., Squires, K., Strelets, M. K., Travin, A., 2006. A new version of detached-eddy simulation, resistant to ambiguous grid densities. Theoretical and computational fluid dynamics 20 (3), 181–195.

[30] Spalart, P. R., Jou, W. H., Strelets, M., Allmaras, S. R., 1997. Comments on the feasibility of LES for wings and on a hybrid RANS/LES approach. Advances in DNS/LES 1 (JANUARY), 4–8.

[31] Tanaka, N., 2010. World energy outlook 2010. International Energy Agency. Paris: IEA.

[32] Tennekes, H., Lumley, J. L., 1972. A first course in turbulence. MIT press.

[33] Tveiterås, V., 2011. Numerical Study of the Interaction of Flow over Two Airfoils in Relative Motion, 1–134.

[34] Versteeg, H. K., Malalasekera, W., 2007. Computational Fluid Dynamics, The finite volume method. Pearson.

[35] Wilcox, D. C., 1994. Turbulence modelling for CFD. 3rd edition. DCW Industries.

Appendix A

CFL values

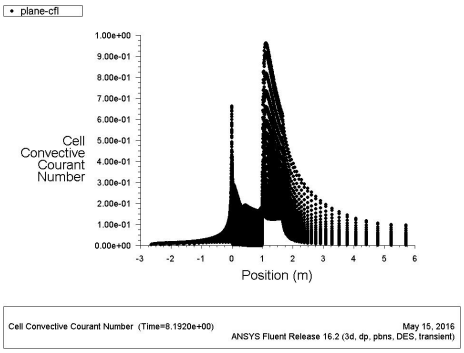

(a) tss = 0.001

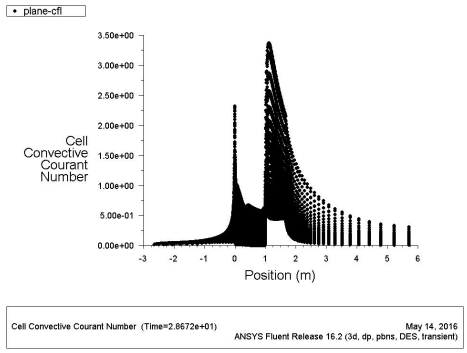

(b) tss = 0.0035

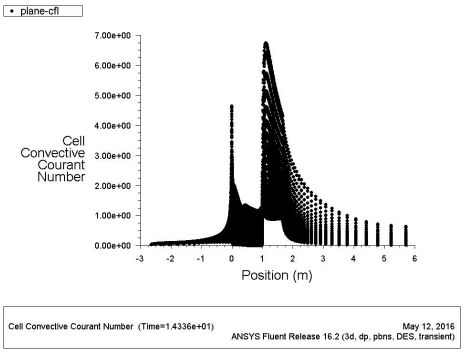

(c) tss = 0.007

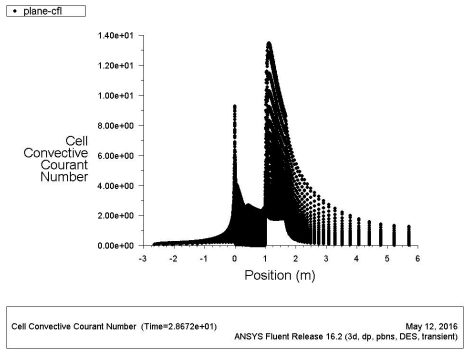

(d) tss = 0.014

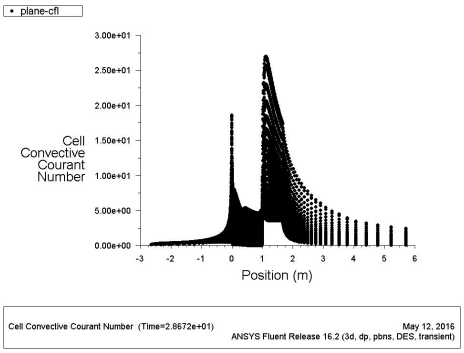

(e) tss = 0.028

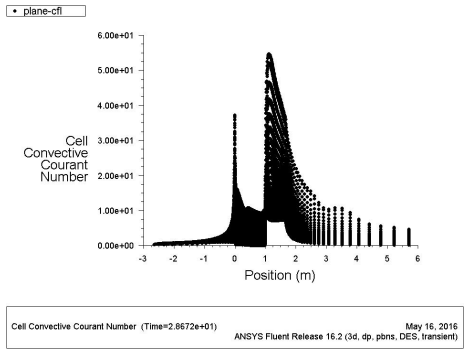

(f) tss = 0.056

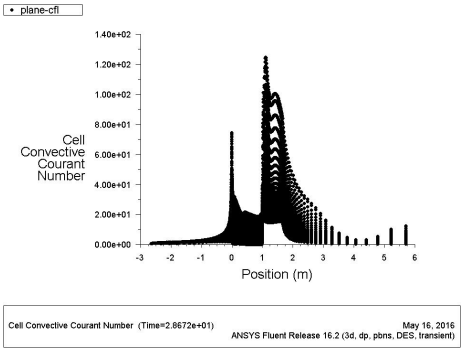

(g) tss = 0.112

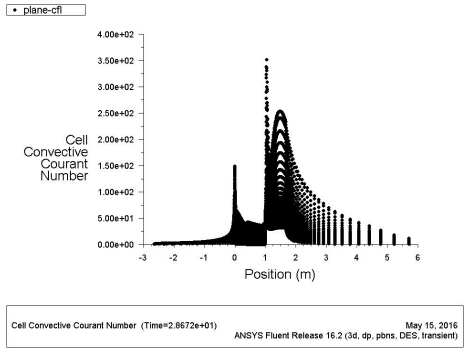

(h) tss = 0.224

Figure A.1: CFL numbers for various time step sizes (tss), $\alpha = 0$, $Re = 10^5$. 0 and 1 on the horizontal axes is the position of the leading and trailing edge of the airfoil respectively

Appendix B

z-direction velocities

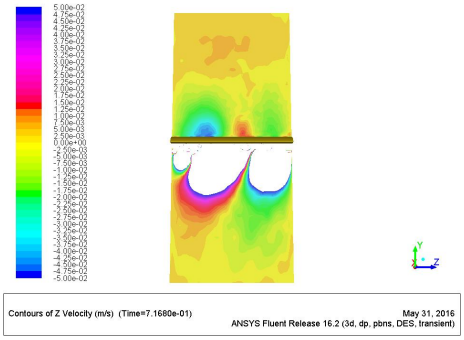

(a) $\alpha = -12$

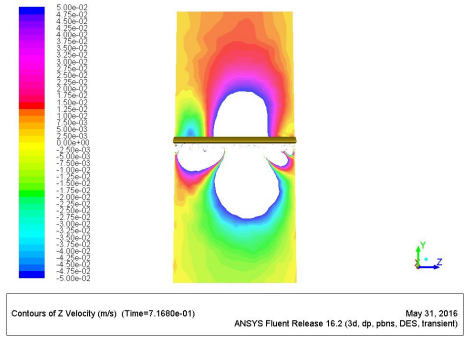

(b) $\alpha = -10$

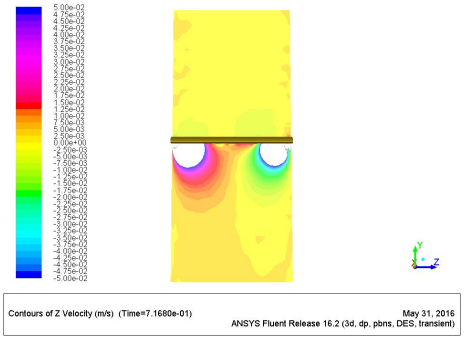

(c) $\alpha = -8$

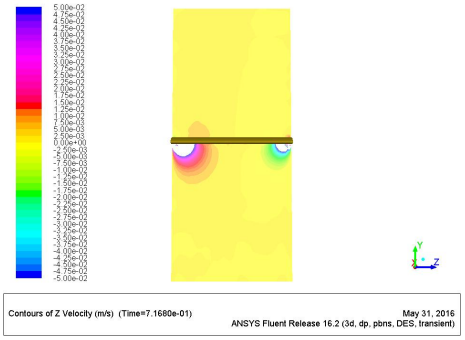

(d) $\alpha = -6$

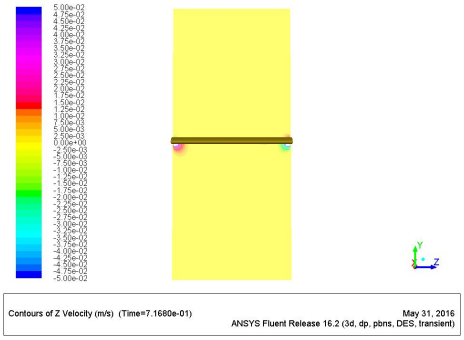

(e) $\alpha = -4$

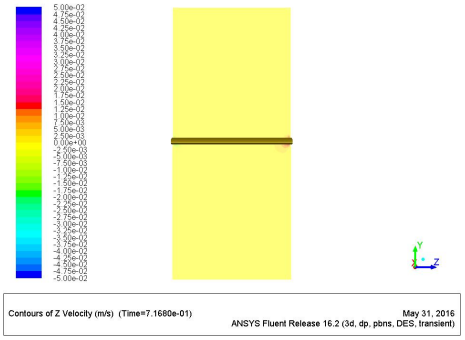

(f) $\alpha = -2$

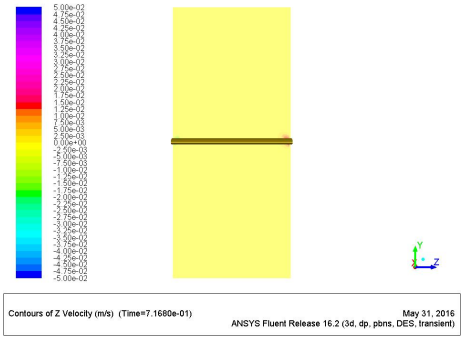

(g) $\alpha = 0$

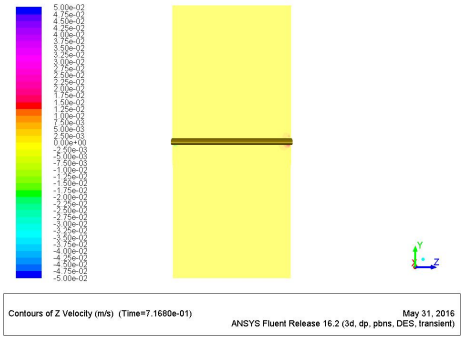

(h) $\alpha = 2$

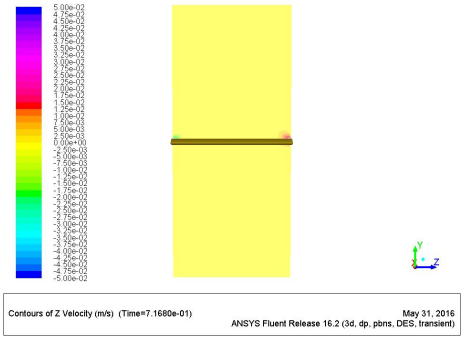

(i) $\alpha = 4$

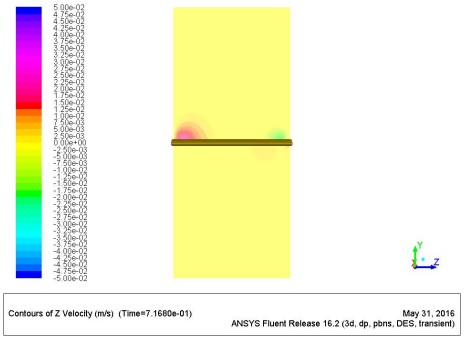

(j) $\alpha = 6$

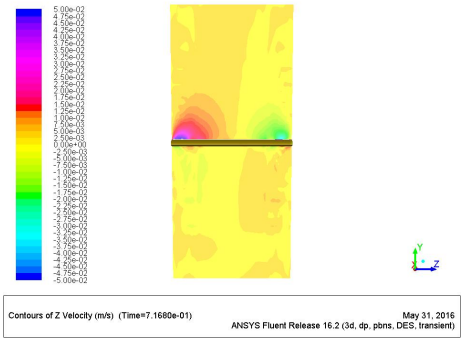

(k) $\alpha = 8$

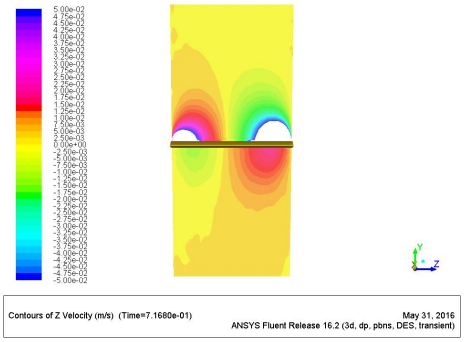

(l) $\alpha = 10$

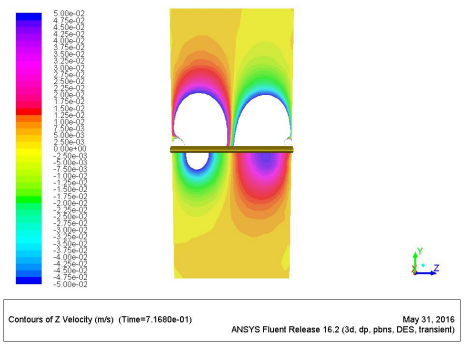

(m) $\alpha = 12$

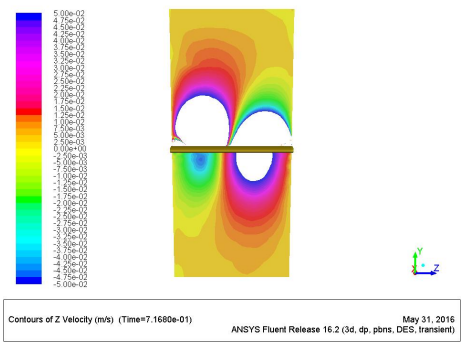

(n) $\alpha = 14$

Figure B.1: Visualization of z-velocities for different angles of attack, $Re = 10^6$. View from the front of the airfoil. The same velocity range is used for every α to make them comparable ($-0.05 m/s < z > 0.05 m/s$)

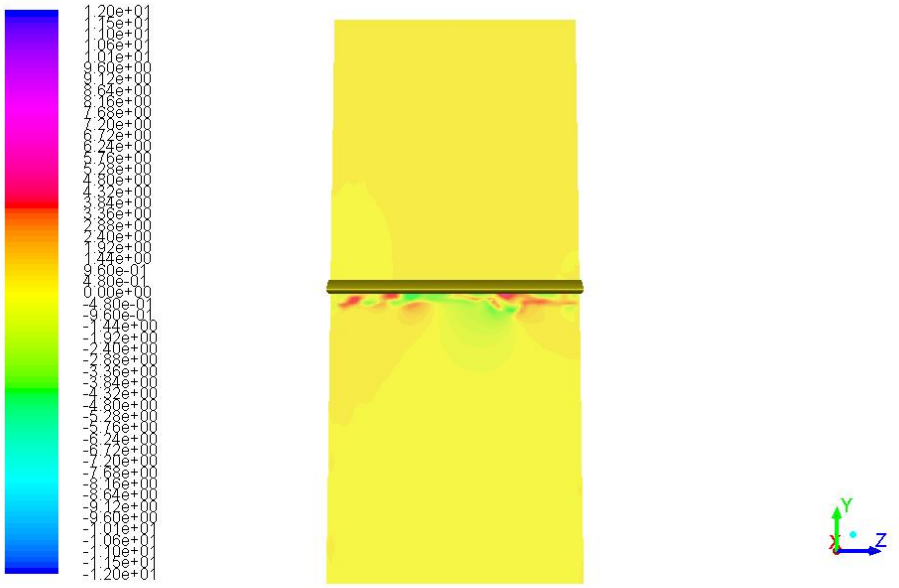

Figure B.2: Visualization of z-velocities for $\alpha = -10$, $Re = 10^6$. View from the front of the airfoil. The velocity range is expanded to capture the whole flow

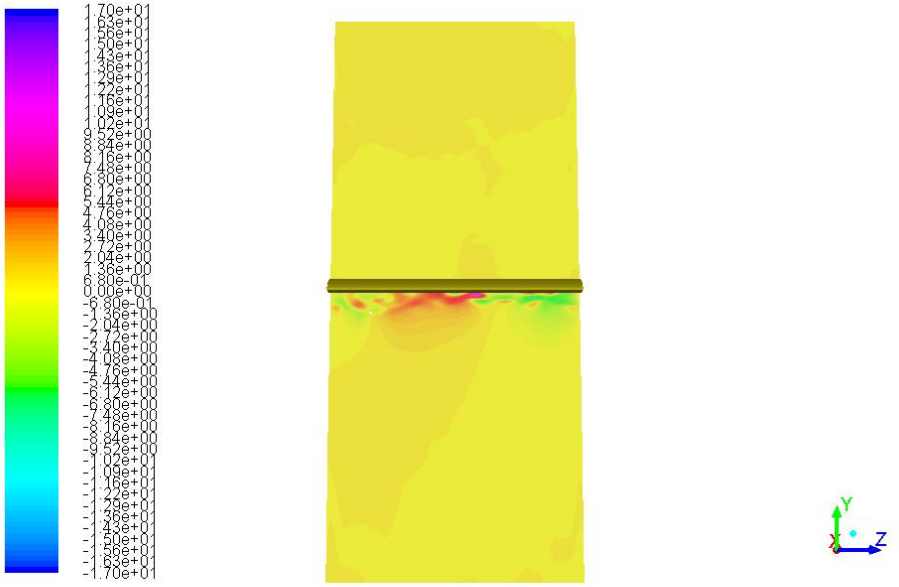

Figure B.3: Visualization of z-velocities for $\alpha = -12$, $Re = 10^6$. View from the front of the airfoil. The velocity range is expanded to capture the whole flow

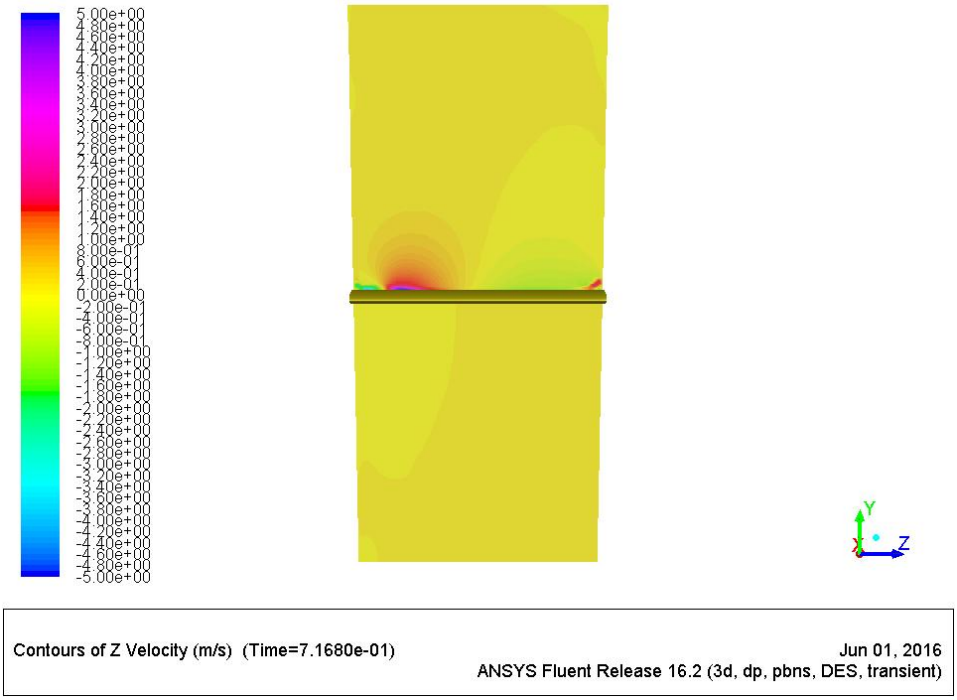

Figure B.4: Visualization of z-velocities for $\alpha = 14$, $Re = 10^6$. View from the front of the airfoil. The velocity range is expanded to capture the whole flow

Appendix C

Grid dependence Cp-plots

For all grid dependence simulation: $Re = 10^5$ and $\alpha = 8$.

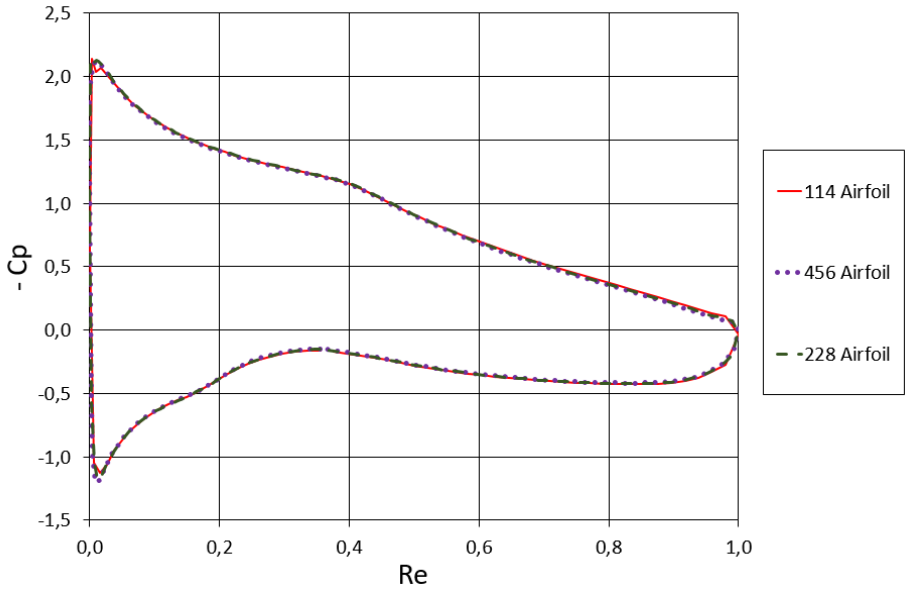

Figure C.1: Different divisions over the Airfoil

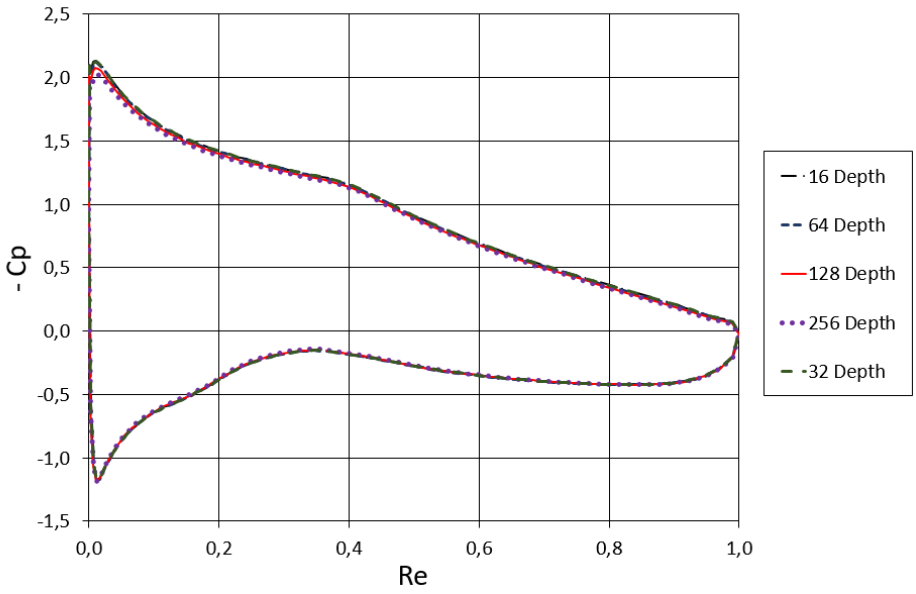

Figure C.2: Different divisions on the depth edge

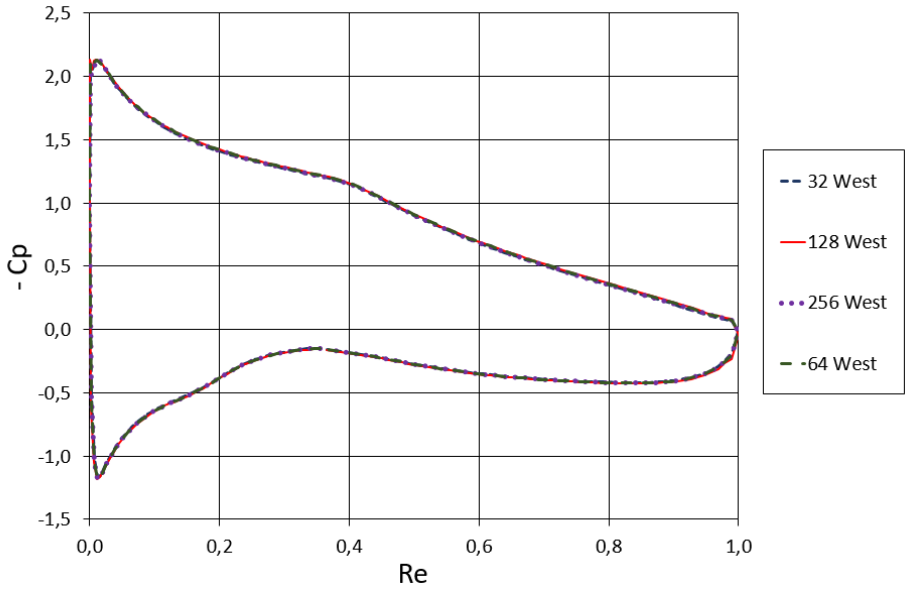

Figure C.3: Different divisions on the West edge

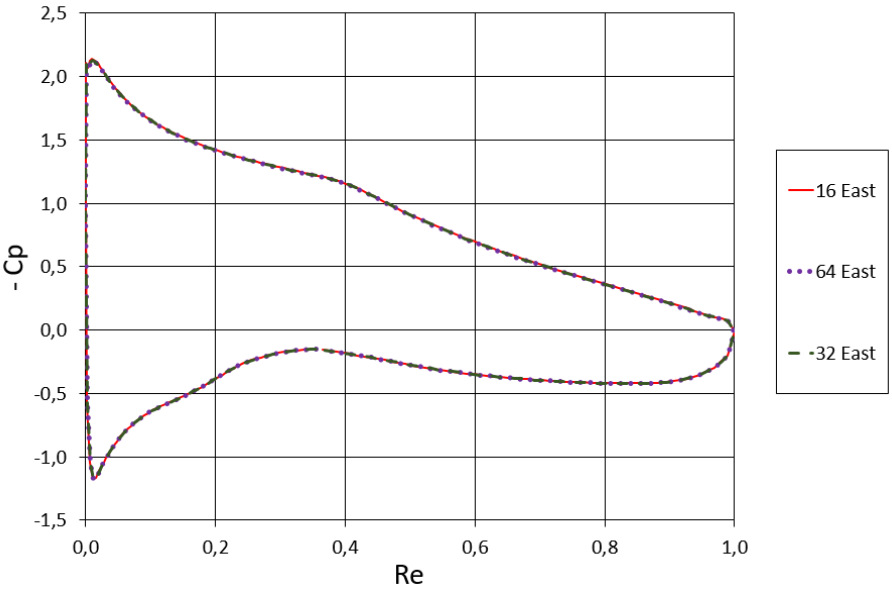

Figure C.4: Different divisions on the East edge

Appendix D

Numerical settings Cp-plots

For all numerical settings simulation below, SA was used with $Re = 10^5$ and $\alpha = 0$. Results are compared with LES results.

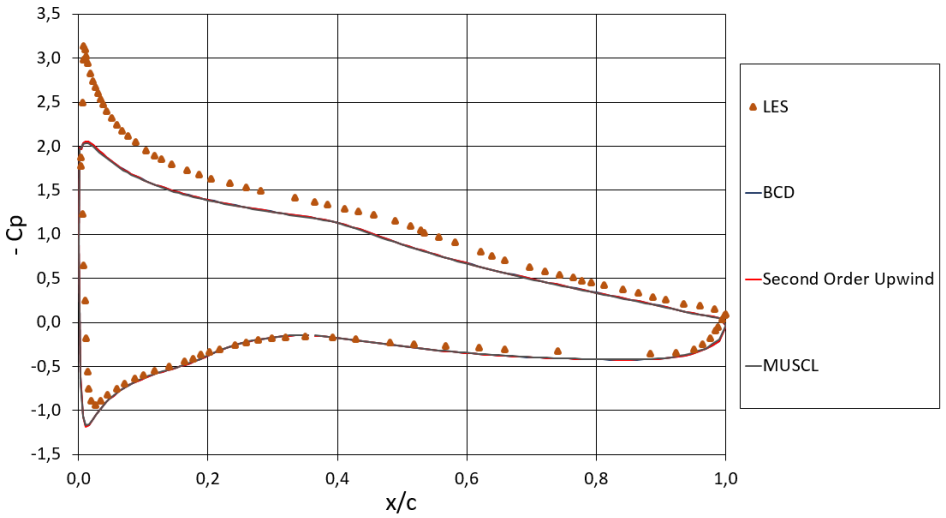

Figure D.1: BCD, MUSCL and Second Order Upwind compared to LES Cp results

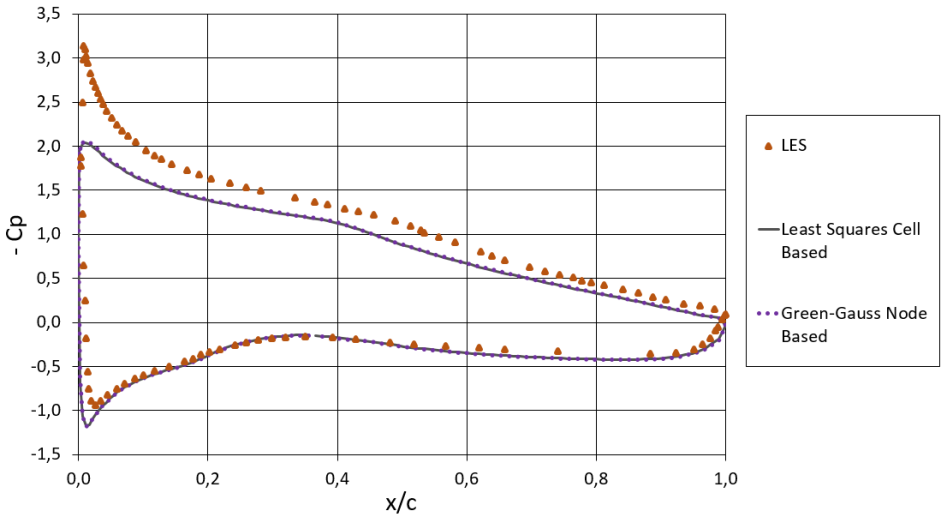

Figure D.2: Least cell squared based and Green-Gauss node based compared to LES Cp results

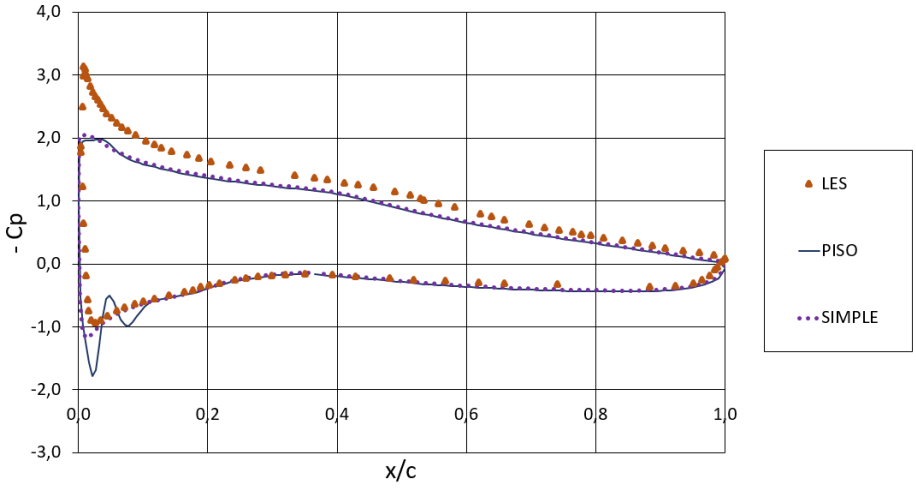

Figure D.3: Piso and SIMPLE compared to LES Cp results

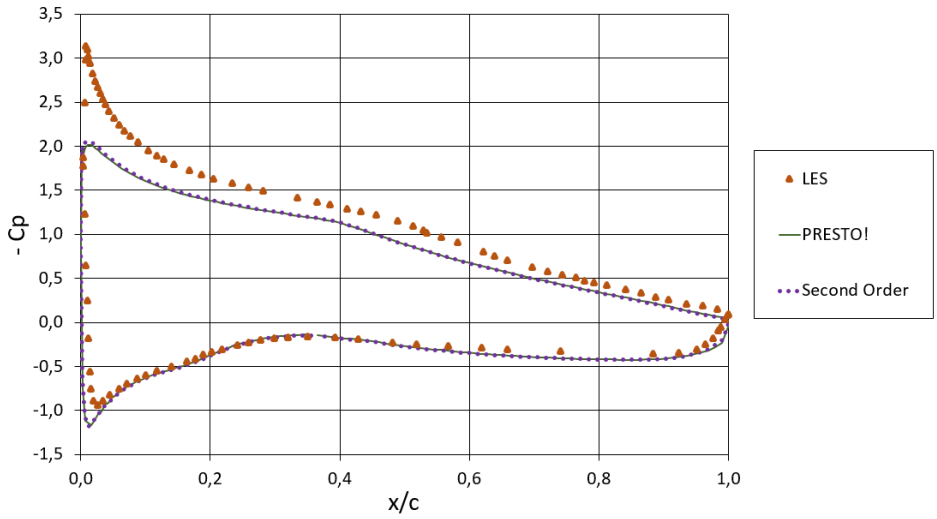

Figure D.4: PRESTO and Second order compared to LES Cp results

Appendix E

Lift and drag against angel of attack for different Reynolds numbers

The Reynolds number for the lift and drag graph from LES (cd and cl) and for the 2D SST $k-\omega$ (cd and cl) is 10^5 in Figure E.1 to E.9

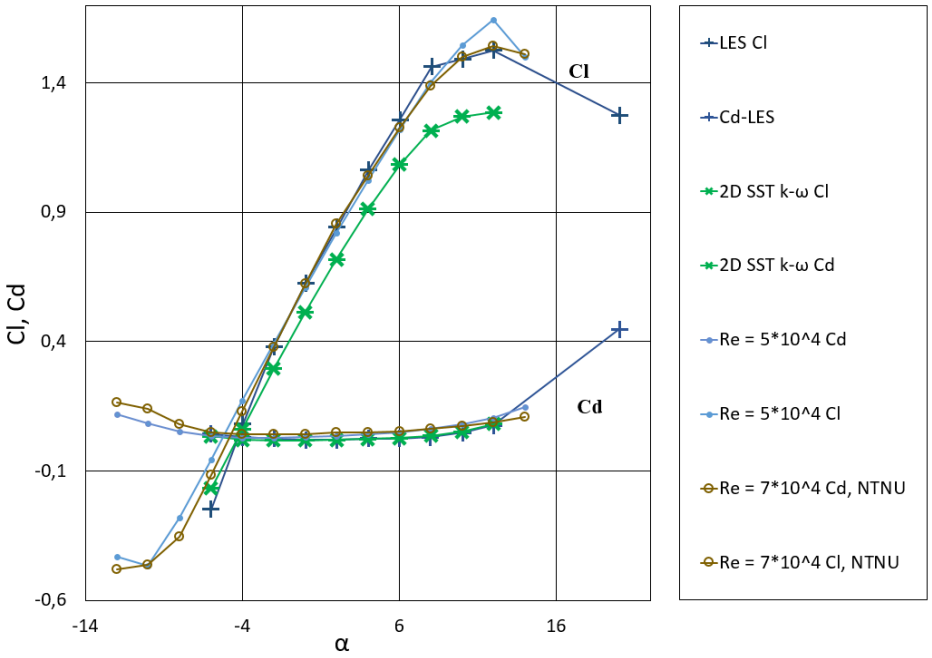

Figure E.1: Lift and drag coefficients for different α and Re= $5 \cdot 10^4$

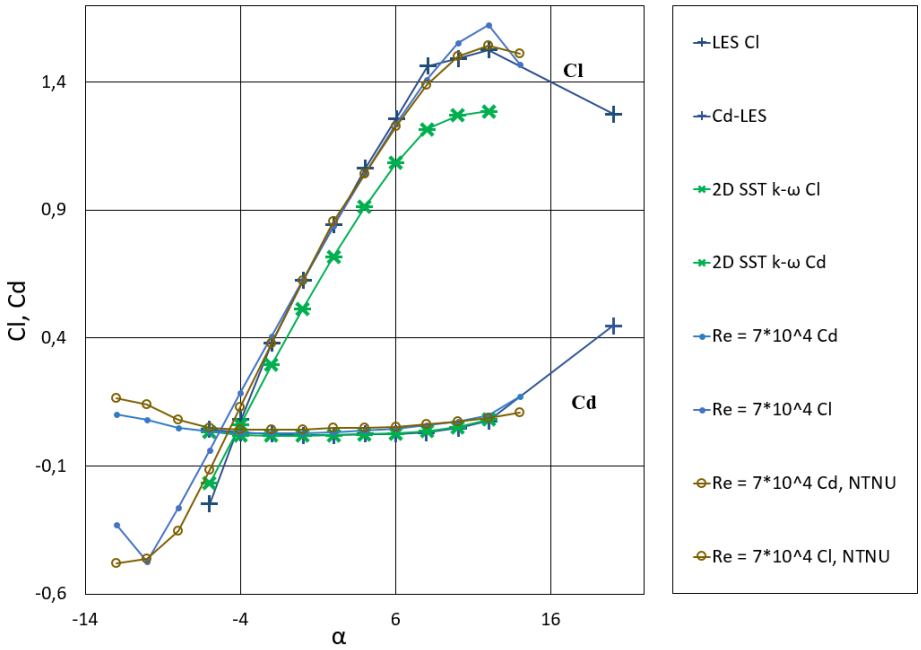

Figure E.2: Lift and drag coefficients for different α and Re= $7 \cdot 10^4$

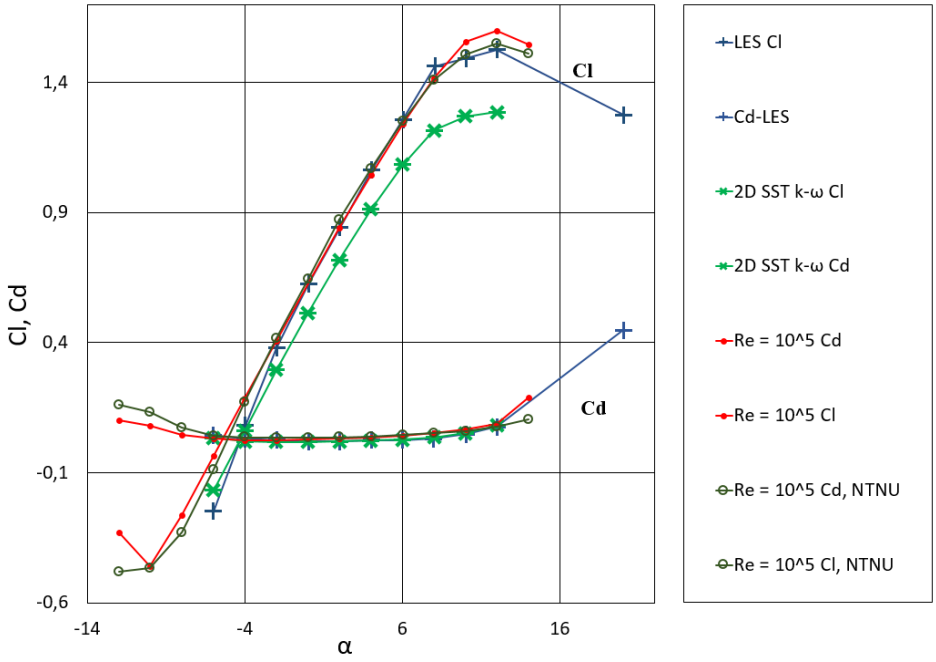

Figure E.3: Lift and drag coefficients for different α and Re= 10^5

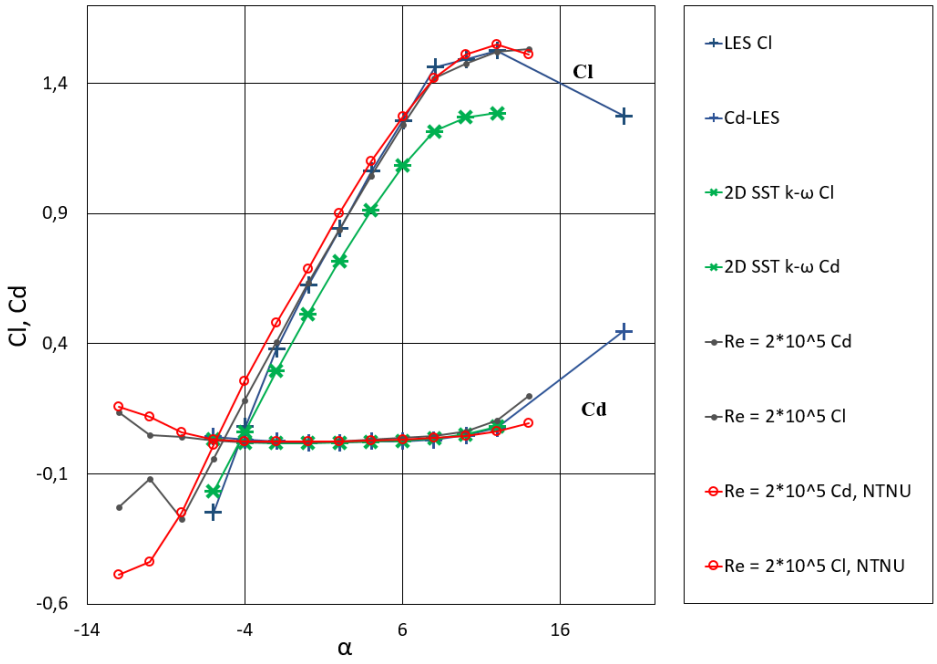

Figure E.4: Lift and drag coefficients for different α and Re= $2 \cdot 10^5$

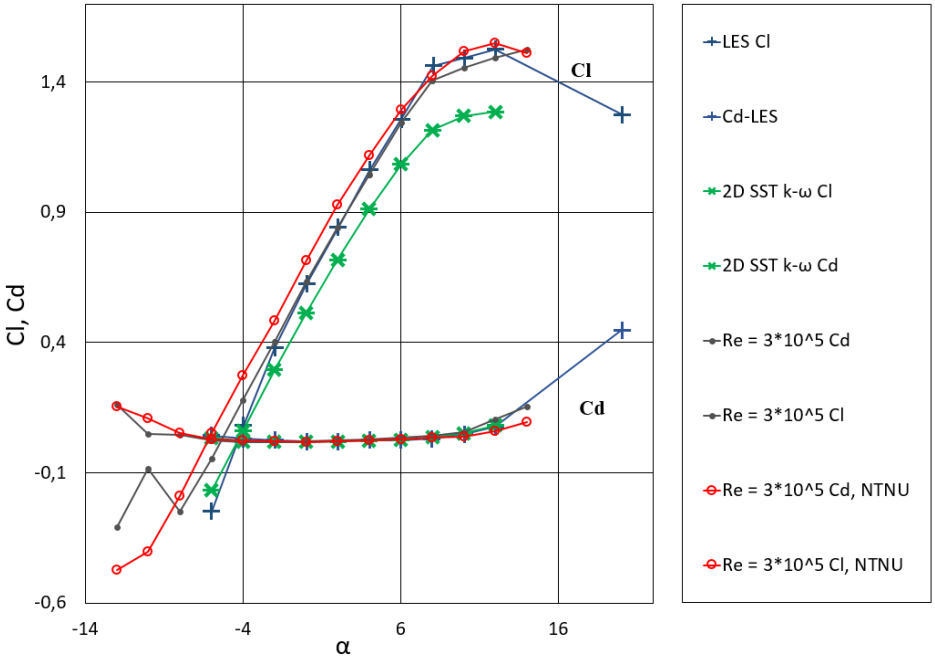

Figure E.5: Lift and drag coefficients for different α and Re= $3 \cdot 10^5$

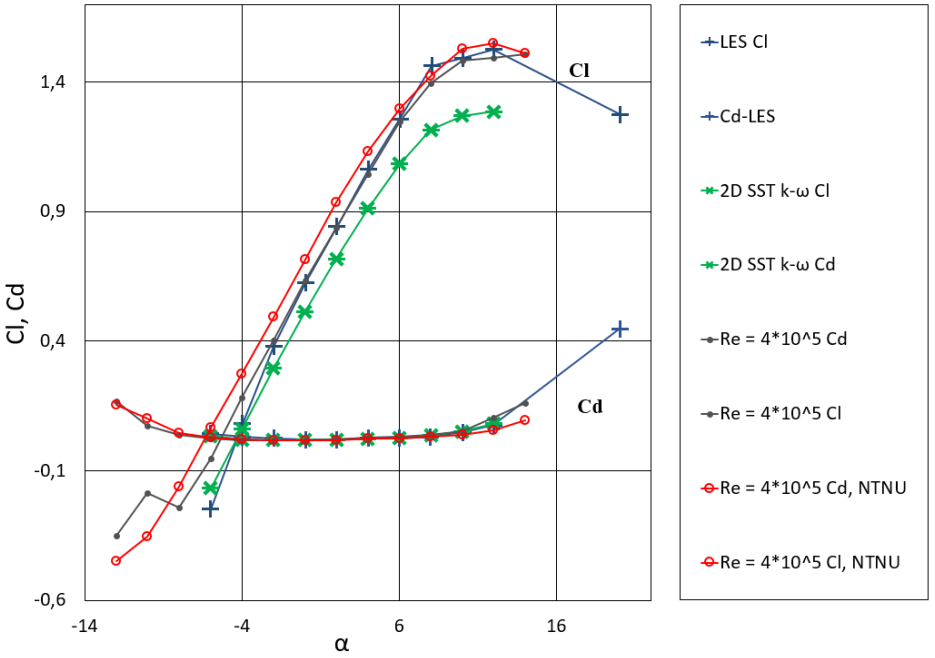

Figure E.6: Lift and drag coefficients for different α and Re= $4 \cdot 10^5$

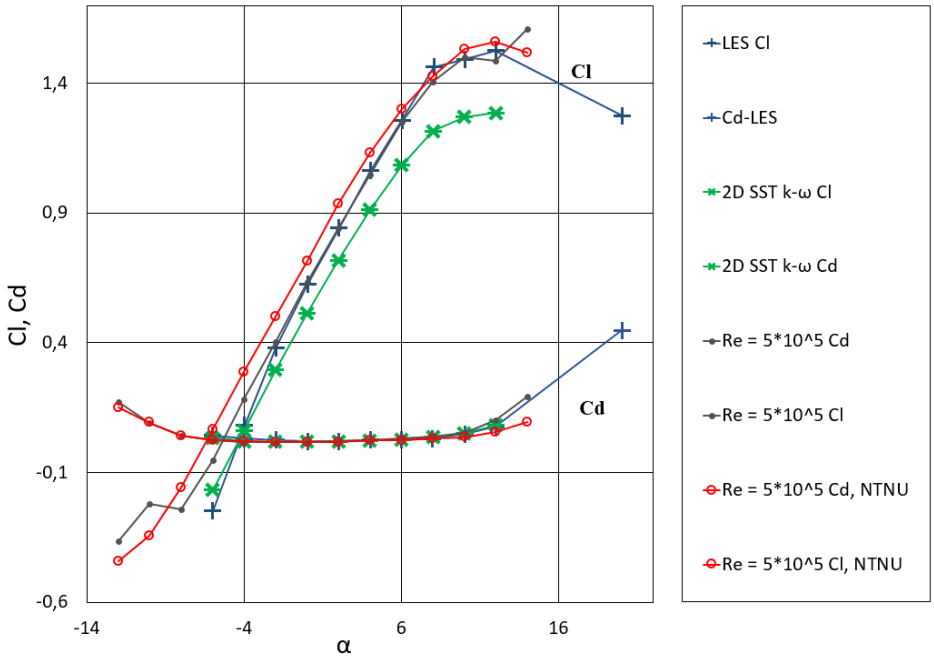

Figure E.7: Lift and drag coefficients for different α and Re= $5 \cdot 10^5$

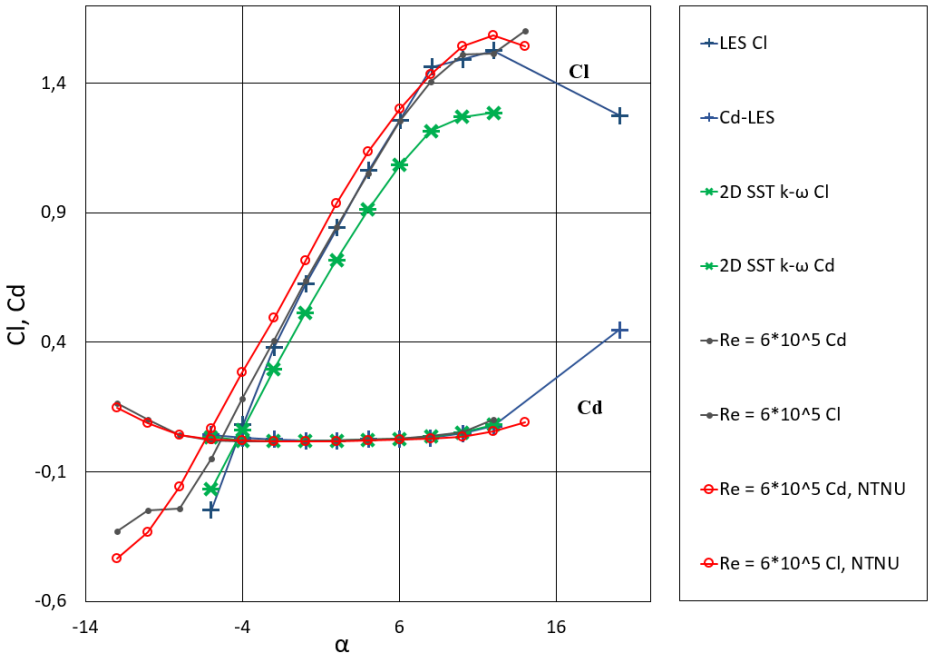

Figure E.8: Lift and drag coefficients for different α and Re= $6 \cdot 10^5$

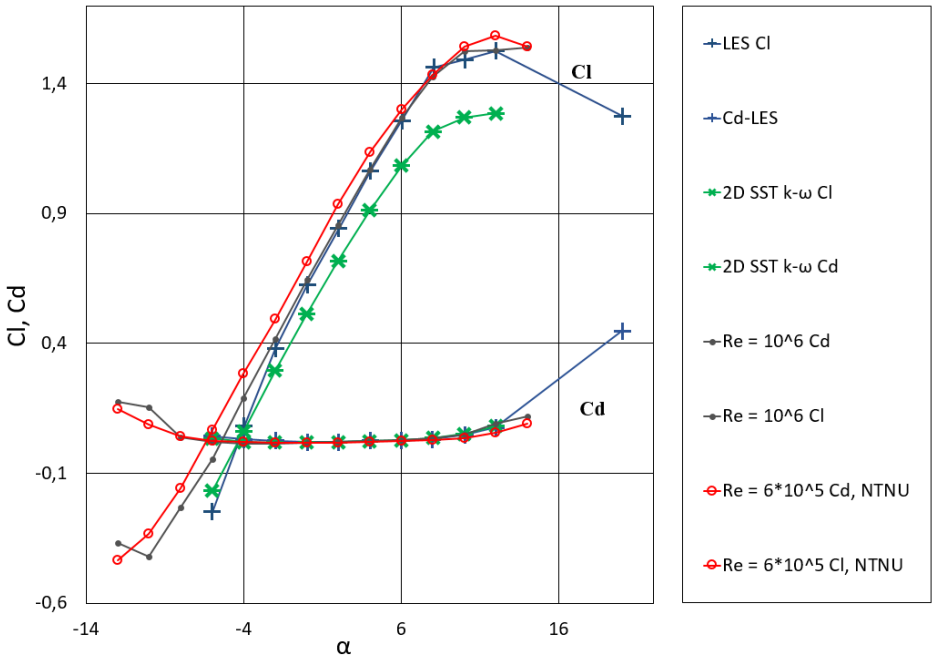

Figure E.9: Lift and drag coefficients for different α and Re= 10^6

Appendix F

Hardware

All of the simulations are run on the Kongull cluster. They are all run on the servers which have:

- 2 x AMD Opteron model 2431 6-core (Istanbul) processors
- 2400 GHz core speed
- 667 MHz (48 GiB nodes) or 800 MHz (24 GiB nodes) bus frequency
- 149GiB 15000 RPM SAS system disc